FOURIER TRANSFORM SPECTROSCOPY OF THE ORION MOLECULAR CLOUD

MARGARET KATHARINE TAHIĆ

B. Sc. Physics, University of Lethbridge, 2002

A Thesis
Submitted to the School of Graduate Studies
of the University of Lethbridge
in Partial Fulfilment of the
Requirements of the Degree

MASTER OF SCIENCE

Department of Physics
LETHBRIDGE, ALBERTA, CANADA

Dedication

Mami Senadi, tati Ramizu i bratu Dejanu,

hvala što ste uvijek vjerovali u mene i što ste žrtvovali sve da bi mi mogli imati bolji život.

I ostaloj porodici, posebno tetki Melki,

nadam se da ćemo se opet vidjeti jednog dana.

Abstract

The Orion Molecular Cloud (OMC) is the nearest, and thus most studied, star forming region to the Earth. To date, most of the studies conducted at submillimetre wavelengths have focused on the spectral line analysis using high resolution heterodyne recievers. However, the role of dust, which is known to be important in the evolution of the interstellar medium, can only be studied through its continuum emission. This thesis presents the first results obtained using a Fourier Transform Spectrometer (FTS) at the James Clerk Maxwell Telescope to study, simultaneously, the continuum and line components of emission on the OMC.

Acknowledgements

I would like to thank David Naylor for taking me on as a graduate student and believing in me from the beginning, even when I did not believe in myself. Thank you for your constant words of encouragement, patience and optimism; I am very grateful for that. Thank you also for allowing me to go to Hawaii and get the first-hand experience of working at the JCMT. I am grateful for the endless hours you spent proof-reading my thesis; I know it was not easy.

I would also like to thank the following people:

Brad Gom - for acting as my surrogate supervisor when David was away and for all your help with IDL. Thank you for proof-reading my thesis; it was extremely helpful.

Ian Chapman - for helping me with IDL and Scientific word and for the words of encouragement.

Alexandra Pope - for being able to use her early programs on rotation diagrams.

Ian Schofield - for writing the software needed to operate the FTS.

Greg Tompkins - for his work on the electronics needed to build the FTS.

Trevor Fulton - for his help with double-checking my work on apodization functions.

Brigette Hesman - for helping me learn how to use the FTS pipeline.

Rachel Friesen - for helping me learn about SEDs.

John Lindner - for his assistance as a proof-reader.

Locke Spencer - for making my days in the office happy ones.

Dr. Paul Hazendonk and Dr. Steve Patitsas - for their assistance as members of my supervisory committee.

Dr. Gary Davis - for giving us the DDT time on the telescope we needed to collect data. Also, thanks for answering my questions regarding the FTS pipeline.

I would also like to thank the staff of the JCMT for all of their assistance in operating the FTS at the JCMT.

I am especially grateful for the financial support of NSERC and the University of Lethbridge.

Contents

List of Figures ix

List of Tables xiii

1 Introduction 1
- 1.1 Overview . . . 1
- 1.2 Star formation . . . 1
- 1.3 Gas and dust in the Interstellar Medium . . . 2
- 1.4 The Orion Molecular Cloud . . . 8
- 1.5 Thesis outline . . . 8

2 Fourier transform spectroscopy: An introduction 11
- 2.1 Overview . . . 11
- 2.2 Fourier integrals . . . 12
- 2.3 Fourier decomposition . . . 14
- 2.4 The Michelson interferometer . . . 23
  - 2.4.1 Monochromatic beam . . . 24
  - 2.4.2 Polychromatic beam . . . 25
  - 2.4.3 Non-ideal Fourier transform spectroscopy . . . 26
- 2.5 Sampling the interferogram . . . 27
- 2.6 Resolution . . . 28
- 2.7 Jacquinot's advantage [1] . . . 31
- 2.8 Fellgett's advantage [2] . . . 33
- 2.9 Phase correction . . . 35
- 2.10 Mach-Zehnder Fourier transform spectrometer . . . 37
- 2.11 Comparison with other spectrometers . . . 40
  - 2.11.1 Grating spectrometer . . . 41
  - 2.11.2 Fabry-Perot interferometer . . . 44
- 2.12 Conclusion . . . 47

3 De-glitching 48
3.1 Overview . . . 48
3.2 Introduction to de-glitching . . . 48
3.3 Approach to de-glitching . . . 51
3.4 Wavelet analysis . . . 52
3.5 IDL® wavelet analysis toolkit . . . 56
3.6 Conclusion . . . 57

4 Apodization 62
4.1 Overview . . . 62
4.2 Introduction to apodization . . . 62
4.3 Natural apodization . . . 68
4.4 The Filler diagram . . . 70
4.4.1 Norton-Beer apodization functions . . . 72
4.4.2 Blackmann-Harris and Hamming apodization functions . . . 76
4.5 Extended apodizing functions . . . 77
4.5.1 Finding the coefficients . . . 79
4.5.2 Amoeba or Downhill simplex method . . . 80
4.5.3 Powell method . . . 81
4.5.4 Results . . . 82
4.6 Conclusion . . . 82

5 Fourier transform spectroscopy of the Orion Molecular Cloud 87
5.1 Introduction . . . 87
5.2 Spectral energy distribution . . . 88
5.3 Methods of determining β . . . 89
5.3.1 SCUBA 850 and 450 μm photometry . . . 91
5.3.2 FTS 850 and 450 μm (dual-band) spectroscopy . . . 94
5.3.3 FTS 850 μm (single-band) spectroscopy . . . 96
5.4 Using FTS spectra to determine the continuum component of emission from Orion-KL . . . 97
5.4.1 Heterodyne spectroscopy versus FTS spectroscopy . . . 97
5.4.2 Orion-KL 850 μm analysis . . . 101
5.4.3 Orion-KL 450 μm analysis . . . 106
5.5 Orion-S analysis . . . 108
5.6 Using FTS spectra to determine spectral line component of emission for Orion-KL . . . 111
5.6.1 Background: Emission and absorption processes for a two-level atom 112
5.6.2 LTE rotation diagram technique . . . 114
5.6.3 Orion-KL at 850 and 450 μm: LTE Rotation Diagrams . . . 116
5.7 Conclusion . . . 120

6 Conclusion and future work 122
6.1 Future work . . . 123

A Unit Conversion 126

B A list of acronyms 128

Bibliography 130

List of Figures

1.1 Orion Nebula image by John Bally (University of Colorado) taken with the Kitt Peak National Observatory (KPNO) 4 meter telescope (National Optical Astronomy Observatory) 9
1.2 Submillimetre Common User Bolometer Array (SCUBA) 850 μm map of Orion. On the right, zoomed-in region of Orion KL and S [3]. 10

2.1 Three cosine waves with different phases. solid line - 0 phase, dash-dot line - $\pi/4$ phase, dot-dot line - $\pi/2$ phase 15
2.2 Fourier transform of the cosine wave of frequency 10 Hz and phase zero, shown in figure 2.1. a) real part b) imaginary part 15
2.3 Fourier transform of the cosine wave of frequency 10 Hz and phase $\pi/4$ shown in figure 2.1 a) real part b) imaginary part 16
2.4 Fourier transform of the cosine wave of frequency 10 Hz and phase $\pi/2$ shown in figure 2.1 a) real part b) imaginary part 16
2.5 The resultant waveform of the superposition of two cosines of frequencies 10 Hz and 11 Hz, equation 2.6. 19
2.6 The real components of the Fourier transform of the waveform shown in figure 2.5 19
2.7 The resultant waveform of the four cosine waves given in equation 2.7. These waves have different amplitudes, frequencies and phases. 21
2.8 Fourier transform of the waveform in the equation 2.7 a) real part b) imaginary part 21
2.9 A more realistic spectrum: a narrow emission line at 2.5 Hz and a narrow absorption line at 6.5 Hz superimposed on a broad emission feature centered at 5 Hz. 22
2.10 23
2.11 a) input spectrum, b) output spectrum, after proper sampling, c) input spectrum that exceeds the Nyquist frequency, d) output spectrum after improper sampling [4] 29
2.12 Top hat function as a function of maximum optical path difference 30
2.13 The Fourier transform of a top hat function, known as a sinc function. . . . 30

2.14 The resultant of two sinc functions of equal amplitudes separated by a frequency of 1/2L. Features are unresolved in the resultant function 32
2.15 The resultant of two sinc functions of equal amplitudes separated by a frequency of 1.21/2L apart. One starts to discern the two component nature of the result. 32
2.16 The resultant of two sinc^2 functions centered 1/L cm^{-1} apart, with each of the sinc^2 functions shown as a black line. 33
2.17 A schematic of the University of Lethbridge Mach-Zehnder FTS. M1, M2 and M5 are plane mirrors, M3 and M4 are powered mirrors, RT are the roof-top mirrors, and BS1 and BS2 are input and output intensity beam dividers [5]. 38
2.18 Top and side views of the U of L Mach-Zehnder FTS in the laboratory [5]. . 39
2.19 A schematic of a reflection grating having a groove spacing of a. Two rays are shown incident at angle θ_i. The optical path difference between the two exiting rays at diffracted at angle θ_m is AB-CD. 41
2.20 Czerny-Turner diffraction grating: the grating provides dispersion and the mirrors provide focusing 44
2.21 Fabry-Perot interferometer 46

3.1 An example of the effect of a cosmic ray on the interferogram 50
3.2 Zoomed-in region of the interferogram shown in figure 3.1. 50
3.3 An interferogram with a cosmic ray: gray lines are an attempt to deglitch. This method picks out the cosmic ray and some of the beat patterns . . . 52
3.4 A time dependent signal consisting of 4 different frequencies: between 0 and 300 ms the frequency is 80 Hz, between 300 and 600 ms, 50 Hz, between 600 and 800 ms, 25 Hz and between 800 and 1000, 10 Hz. 54
3.5 A wavelet transform of the non-stationary signal shown in figure 3.4 55
3.6 Wavelet transform of the interferogram shown in figure 3.1. The cosmic ray at 80 ms shows a wide range of scale in the wavelet transform. By comparion, the heavily modulated zero path difference region of the interferograms shows a low and limited range of scales in the wavelet transform. 58
3.7 Daubechies wavelet 59
3.8 Coiflet wavelet 59
3.9 Haar wavelet 60
3.10 Morlet wavelet 60
3.11 Paul wavelet 61
3.12 Symlet wavelet 61

4.1 Infinite cosine wave of frequency σ_0 64
4.2 Top hat function with a maximum optical path difference of $\pm L$. 64
4.3 A truncated interferogram of a monochromatic source of frequency σ_0 . . . 65
4.4 Fourier transform of the interferogram in figure 4.3 65
4.5 A diagram of light entering the entrance aperture at an angle α. 69
4.6 Filler diagram for $D_\alpha(\delta), E_\alpha(\delta)$ and $P_{\alpha,p}(\delta)$ functions. Red and orange portions of the graph are somewhat linear as proposed by Filler 71
4.7 Norton-Beer weak, medium and strong apodizing functions 73

4.8 Instrumental line shapes for Norton-Beer weak, medium and strong apodizing functions as a function of maximum optical path difference, L 73
4.9 Filler diagram for the instrumental line shapes of apodizing functions discussed in the text. The solid line is the empirical boundary defined by equation 4.17 75
4.10 Four apodizing functions: Blackman-Harris (3-terms), Blackman-Harris (4-terms), Hamming and adjusted Blackman-Harris (4-terms) 78
4.11 Instrumental line shapes of Blackman-Harris, Hamming and Adjusted Blackman-Harris apodizing functions 78
4.12 Ten extended Norton-Beer apodizing functions. The function corresponding to FWHM of 1.1 is in black, the rest of the functions in decreasing order of the tail amplitude correspond to FWHM of 1.2, 1.3 etc. 83
4.13 Instrumental line shapes corresponding to the 10 apodizing functions compared with the sinc function (pink line). Insert shows the magnified region of the third sidelobe. 83
4.14 Extended Norton-Beer apodizing functions (red circles) compared with three original Norton-Beer apodizing functions (blue cirlcles) and the triangle (Bartlett) apodizing function (red triangle) 84

5.1 Model spectral energy distribution for source flux of 100 mJy at 850 μm, dust emissivity $\beta = 1.5$ and 2 and temperatures of 10, 20, 30, 40, 50 K. The passbands of the 850 μm and 450 μm bands are identified by solid black lines. 90
5.2 Model spectral energy distribution for source flux of 100 mJy, dust emissivity $\beta = 1.5$ and 2 and temperatures of 10, 20, 30, 40, 50 K. White noise was introduced into two bands as discribed in the text. 91
5.3 The transmission of the atmosphere: at 1 mm precipitable water vapour (black) and at 0.5 mm precipitable water vapour (gray), corresponding to average and excellent observing conditions, respectively. The spectral range of the 850 μm band is from 330 - 365 GHz and for the 450 μm band is from 630 - 700 GHz. 93
5.4 Uncertainty in derived β as a function of temperature for different observation methods (upper plot). Uncertainty in derived β as a function of temperature excluding the photometric dual-band method (lower plot) 95
5.5 (Upper plot) The raw heterodyne spectrum of Orion-KL showing the variation in baseline between individual scans. Some of the more clearly identified lines are shown. (Lower plot) The raw heterodyne spectrum of Orion-KL with the baseline corrected. 100
5.6 (Upper plot) Spectrum of Orion-KL taken with Fourier Transform Spectrometer, most of the prominent spectral lines are identified. (Lower plot) Spectrum of Orion-KL taken with Caltech Submillimeter Observatory Fourier Transform Spectrometer. In comparison to the upper plot, the spectral lines resemble a histogram [5]. The identification of spectral lines was done by comparing the spectrum to Schilke et al. [6] heterodyne spectrum of the same region. 102

5.7 Comparison of FTS spectra of Orion molecular (gray trace) with the convolved heterodyne spectra (black trace). 103
5.8 Fitting $A\nu^{\gamma}$ to the regions of lowest spectral line content in the Orion-KL spectrum. 105
5.9 Comparison of FTS spectra of Orion-KL (black trace) with fitted continuum plus sinc convolved heterodyne spectra of the same region (gray trace). . . . 105
5.10 A map of the mean spectral index, γ, as a function of 850 μm flux (Jy), along with $\pm 1\sigma$ error estimate of the Orion Molecular Cloud taken with SCUBA photometer [3] 106
5.11 Spectrum of Orion-KL at 450 μm taken with the U of L FTS at a resolution of 150 MHz or 0.005 cm^{-1} (upper plot). Spectrum of Orion-KL at 450 μm taken with the CSO FTS with the 200 MHz resolution (lower plot) [5]. . . . 107
5.12 Heterodyne spectrum of Orion-S. Some of the most prominent spectral lines are identified on the plot. 109
5.13 Heterodyne spectrum of Orion-S (black trace) convolved with the FTS instrumental line shape (gray trace) displaced -10 K for clarity. 110
5.14 Measured FTS spectrum of Orion-S (black curve) compared to convolved heterodyne spectrum (gray curve) displaced -3.5 K for clarity. 111
5.15 The emission and absorption processes for a two level atom. N_2 and N_1 are the populations of the levels 2 and 1, respectively, g_2 and g_1 are the degeneracies of the two levels, and E_2 and E_1 are the energies of the levels. 112
5.16 Rotation diagrams for SO_2 (upper plot) and SO (lower plot) reproduced from Serabyn's data. 118
5.17 Rotation diagrams for SO_2 (upper plot) and SO (lower plot) for U of L FTS data. 119

List of Tables

4.1 FWHM, height (upper) and position (lower) in units of 1/L of the first 5 secondary minima of a sinc function (figure 4.4) normalized to the principal maximum. 67

4.2 FWHM, height (upper) and position (lower) in units of 1/L of the first 5 secondary maxima of a sinc function (figure 4.4) normalized to the principal maximum. 67

4.3 Coefficients of the Norton-Beer apodizing functions. 74

4.4 Coefficients of the extended Norton-Beer apodizing functions. 82

4.5 FWHM and height (upper row) and position (lower row) of the first five minima of 10 best apodizing functions in units of 1/L. 85

4.6 FWHM and height (upper row) and position (lower row) of the first five maxima of 10 best apodizing functions in units of 1/L. 86

4.7 FWHM and height of the largest secondary maximum of 10 best Norton-Beer apodizing functions. 86

5.1 Comparison of errors in retrieved β 97

5.2 Comparison of Rotation Temperatures and Column Densities for two different molecules: SO and SO_2 120

A.1 Unit conversion between wavelength, λ, wavenumber, σ and frequency, ν for 450 μm waveband. 127

A.2 Unit conversion between wavelength, λ, wavenumber, σ and frequency, ν for 850 μm waveband. 127

Chapter 1

Introduction

1.1 Overview

This chapter gives a brief introduction to star formation, followed by a discussion of the composition and the structure of molecular clouds. The Orion Molecular Cloud (OMC), the brightest such source at submillimetre wavelengths, is the focus of this thesis.

1.2 Star formation

Stars form in the interstellar medium (ISM) from collapsing clouds of gas and dust [7, 8, 9, 10]. The temperature of these clouds lies in the range of 10 - 50 K. The temperature and density are highest at the center of the cloud, where a new star will eventually form. Under such conditions, the gravitational forces exceed the internal pressure of the cloud and the part of the cloud collapses. The object that is formed at the center of the collapsing cloud, and which will become a star, is called a protostar. Since the protostar is embedded

in the cloud of gas and dust, it is difficult to detect at visible wavelengths, since these wavelengths are heavily scattered. Since the temperature of the cloud gives rise to the peak intensity of emission in the far infrared and submillimetre region of the electromagnetic spectrum, according to Wien's law, protostars can only be studied at these long wavelengths. Upon maturation, the star will carve out a cocoon in the surrounding material at which point it will become visible [8]. Long wavelength studies thus provide key information on the star formation process and a window on how the Solar System itself was formed.

1.3 Gas and dust in the Interstellar Medium

In 1968, Spitzer [11] suggested that the ISM can be viewed in terms of dense, cool clouds in pressure equilibrium, and a warm, thin intercloud medium. A year later, in 1969, Field, Goldsmith and Habing [12] developed a two-phase model of the ISM, based on heating by the low energy cosmic rays, which includes a warm intercloud medium at temperature of $\sim$ 10000 K which is approximately 10 % ionized. The second phase of the model consists of cold clouds with temperatures less than 300 K. In 1977, the model was refined further by McKee and Ostriker [13] to include the effects of super nova explosions. In this model, there are three components. Most of the interstellar medium is composed of hot (with temperature of $\sim 500,000$ K), low density of $\sim 0.03 \mathrm{cm}^{-3}$ medium (HIM), which is moderately inhomogeneous [13]. Embedded in this medium are the cold ($\sim$ 100 K) and dense ($\sim$ 40 cm^{-3}), neutral clouds (CNM). Surrounding these clouds is the warm ($\sim$8000 K) photoionized cloud corona, which occupies a larger volume then the cold gas but has less mass [13]. The authors separated this phase into two regions: warm neutral medium

(WNM), which is an inner region having a fractional ionization of ~ 0.1, and an ionized medium (WIM), which is an outer region with fractional ionization of ~ 0.7.

The ISM consists of both gas and dust. The gas appears primarily in two forms: Cold clouds of atomic or molecular hydrogen, and near hot young stars ionized hydrogen. The clouds of cold molecular and atomic hydrogen are the material from which stars can be formed if they become gravitationally unstable and collapse [10].

Interstellar dust grains play a major role in the composition and evolution of the interstellar medium because the dust acts as a catalyst for molecule formation, such as molecular hydrogen, H_2O, CH_4, and NH_3. Dust particles range in size from about 1 nm to 1 μm [7]. Radiation from cold dust is the primary source of continuum emission in the ISM. The continuum emission varies with temperature and type of dust, and can be expressed as [14]:

$$S_\nu = (N_g M_g)\,\kappa_0 \left(\frac{\nu}{\nu_0}\right)^\beta B_\nu(T_d)\Omega. \tag{1.1}$$

Here, S_ν is measured in Janskys (Jy) where 1 Jy = $10^{-26}\mathrm{Wm^{-2}Hz^{-1}}$, κ_0 ($\mathrm{m^2/kg}$) is the dust emissivity at some reference frequency ν_0 (Hz), β is the dust emissivity index, and $B_\nu(T_d)$ ($\mathrm{Wm^{-2}str^{-1}Hz^{-1}}$) is the Planck blackbody function at frequency ν (Hz) for dust at temperature T_d, Ω is the solid angle, N_g is the dust column density ($\mathrm{m^{-2}}$) and M_g is the mass of the dust grains (kg).

There are several pieces of evidence for the presence of dust grains in the ISM, the most important of these are as follows:

Depletion of elements

Relative abundances of chemical elements in the Sun have been assumed to be typical of the Galaxy as a whole. It has been found, however, that the abundances of some elements are greatly reduced in the cold clouds of the ISM. It has also been found that the elements which are able to form refractory solids are highly depleted, which suggests that elements that can form such solids are being removed from the gas [7]. There is a strong correlation between the condensation temperature of the element being depleted and the amount of depletion: the higher the condensation temperature of an element, the more it will be removed from the gas phase [7]. For example, titanium is depleted by a factor of more than a 1000, relative to the Sun, while oxygen is underabundant by a factor of 3 [7, 15].

Extinction

Extinction (the reduction of the intensity of light as it travels through the ISM) means that there is an agent that is scattering or absorbing the star light [7, 10]. The intensity of the star light after it has gone through a medium is defined by [7]

$$I = I_0 \exp\left(-\int_0^l \alpha \mathrm{d}l\right). \tag{1.2}$$

Here, I_0 is the initial intensity of the light, l is the distance the light has passed through the medium and α is the extinction coefficient. α (m^{-1}) is not constant of the medium but depends on the physical conditions of the ISM. Dust grains are believed to be a principle source of extinction in the ISM [7]. Extinction is measured by comparing the spectra of stars having the same spectral type, for example O or B stars, one chosen to have little

material between the star and the observer, and the other extinguished by dust along the line of sight [7]. The amount of extinction can be measured by the differences in measured light intensities [7]. Some of this difference can be attributed to the stars being at different distances, but there will also be a difference in measured intensities due to extinction. The two star intensities, I_1 and I_2, can be related to the difference in magnitudes, Δm, by the following equation [7, 15]:

$$\Delta m = -2.5 \log_{10} \frac{I_1}{I_2}. \tag{1.3}$$

The typical extinction at visible wavelengths for a region in our galaxy is about 1 magnitude for a path length of 1 kpc [7].

Polarization

Starlight is, in general, linearly polarized by a few percent, with the amount of polarization being proportional to the amount of the extinction [7]. In order to polarize light, the interstellar grains cannot be spherical but must be elongated, and there must be some degree of alignment of the elongated grains. If these two conditions are satisfied, then radiation with electric vectors parallel to the longer axis of the grains will be more extinguished than vectors parallel to the shorter ones, resulting in net polarization of the radiation [7].

Scattered light

Our galaxy is filled with diffuse light that cannot be traced to a particular source. The simplest explanation for this is that the light is being scattered by some agent. Since scattering by atoms and molecules would be insufficient to account for the diffuse light seen,

this provides support for the existence of interstellar grains [7].

Solid state spectral lines

There are several absorption lines in the infrared that are attributed to absorption of radiation from background stars by foreground solid particles. If dust grains are hot, they will emit, or absorb, radiation not only in continuum but also in spectral bands. At a wavelength of about 3 μm, a strong absorption of background stars light is detected. Since H_2O ice would evaporate before it could radiate at a wavelength of 3 μm, it is thought that silicates, which can withstand high temperatures, are the cause of this absorption [7].

It is clear from the indications listed above that dust plays a key role in the evolution of the ISM. Since dust particles are small, and generally found at low temperatures in the ISM, dust can only be studied closely at the submillimetre wavelengths. Submillimetre astronomy is one of the last windows of the universe to be open to investigation. This is due largely to the fact that photons at these wavelengths have such small energy and the complexity of the instrumentation required to study them.

Dust plays a key role in the evolution of the ISM. At submillimetre wavelengths, the optical depth is much less than one so the dust emission is optically thin, which allows for all the dust emission to be observed along the line of sight [14]. This fact is useful in determining the mass of the cloud and other physical parameters such as column densities[14, 16, 17]; however, the intensity of the dust emission depends on the temperature of the dust and its emissivity, β, which depends on the composition and grain size of the dust. One goal of this thesis is to determine the dust emissivity index, β, of Orion-KL, one of the brightest regions in the OMC, but the effects of temperature need to be taken

into account (equation 1.1). Currently the only means of estimating β from submillimetre measurements uses dual band photometry, which requires a knowledge of the dust temperature. As will be seen in chapter 5, this method is largely dependent on the assumed dust temperature for which the variation in β can be very large. In this thesis, I present the first estimates of the results of the dust emissivity, β, based on submillimetre spectroscopic measurements alone. The gas in the ISM can be studied through high resolution spectroscopy of spectral line emission or absorption, while the dust can be studied through low resolution measurements of continuum emission or absorption.

As mentioned earlier in this chapter, there is much evidence for the existence of dust. Dust is known to be an important catalyst for the formation of a wide range of molecules. The emissivity of the dust is expected to change during the evolution of the ISM. For example, cold dust can accrete a mantle of ice, which decreases the emissivity. It has been shown that the emissivity can have a wide variation, which is believed to track the evolutionary stages of the Universe. Dust emissivity is an important diagnostic tool for probing the evolution of ISM, protostars in particular.

This thesis presents a feasibility study for using a Fourier transform spectrometer (FTS), with its variable resolution, to measurements of the continuum and line emission from the interstellar clouds. The target chosen for this analysis is the OMC, the brightest galactic source at the submillimetre wavelengths.

1.4 The Orion Molecular Cloud

The Orion emission nebula, shown in figure 1.1, is the nearest star formation region to the Earth (about 450 pc away). The nebula is visible with the naked eye as the middle star in Orion's "sword". Because of its close proximity to Earth and its brightness, it has become a Rosetta stone for astronomers studying star formation. For example, the first protostars were discovered in the OMC as were most of the 125 molecules discovered in the ISM to date (Aug 2004) [18, 19]. The optical emission from the Orion nebula, also known as M42, arises from the ultaviolet flux from the Trapezium cluster. The four brightest stars of this cluster seen in the centre of figure 1.1 photo-ionize the surrounding nebula.

1.5 Thesis outline

This thesis addresses the applicability of Fourier transform spectroscopy at submillimetre wavelengths to the study of the ISM. Chapter 2 introduces the mathematical principles of FTS spectroscopy. Chapter 3 discusses the removal of noise spikes in the interferograms caused by cosmic rays. Chapter 4 introduces several new apodizing functions for FTS spectroscopy. Chapter 5 presents spectroscopic measurements obtained with an FTS, of Orion-KL and Orion-S, the two brightest regions of the OMC, in the submillimetre region shown in figure 1.2, . The chapter shows that it is possible to extract both the continuum and line components of emission from the interstellar medium with an FTS. And finally, chapter 6 outlines the future prospects for FTS spectroscopy at submillimetre wavelengths.

Figure 1.1: Orion Nebula image by John Bally (University of Colorado) taken with the Kitt Peak National Observatory (KPNO) 4 meter telescope (National Optical Astronomy Observatory)

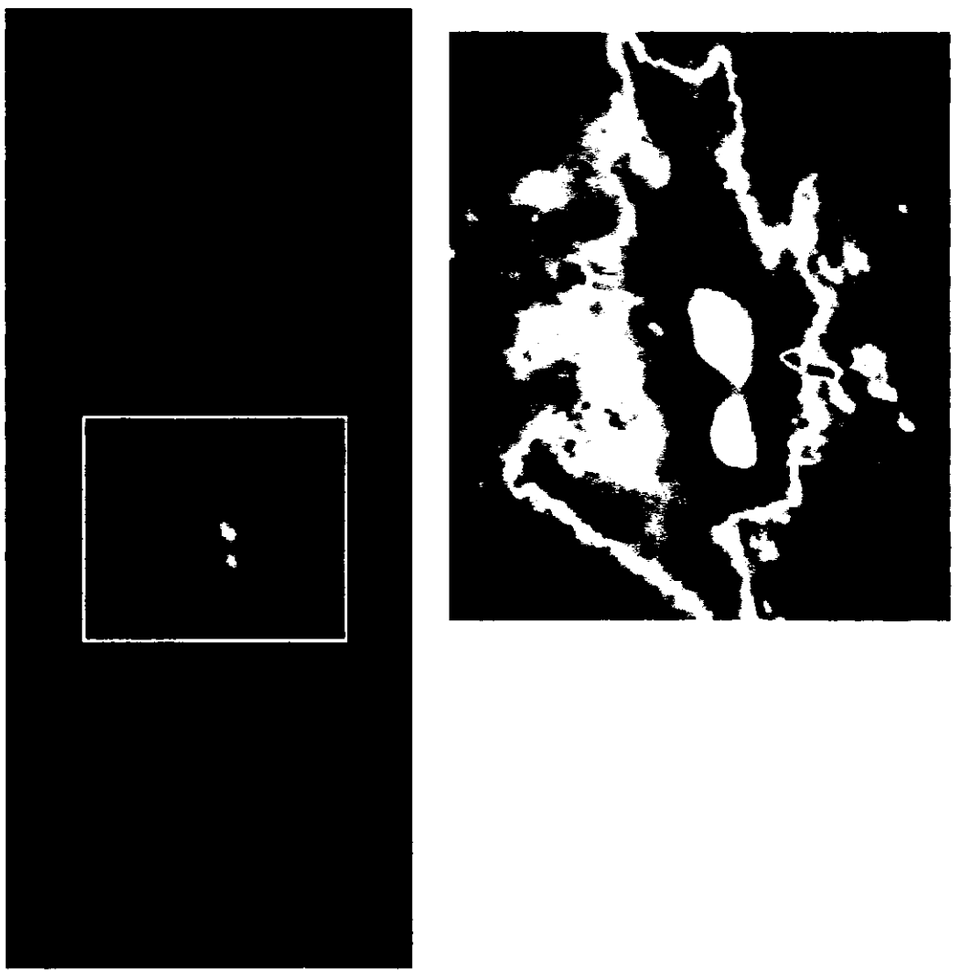

Figure 1.2: Submillimetre Common User Bolometer Array (SCUBA) 850 μm map of Orion. On the right, zoomed-in region of Orion KL and S [3].

Chapter 2

Fourier transform spectroscopy: An introduction

2.1 Overview

This chapter gives a brief overview of Fourier transform spectroscopy and the underlying mathematical principles. The chapter includes a description of the Mach-Zehnder FTS built by the Astronomical Instrumentation Group (AIG) at the University of Lethbridge (U of L), headed by Dr. David Naylor, for use at the James Clerk Maxwell Telescope (JCMT). The JCMT is the world's largest submillimetre telescope which is located atop Mauna Kea, Hawaii, widely regarded as the world's premier astronomical observing site.

2.2 Fourier integrals

One of the techniques for analyzing periodic functions was developed by Jean Baptiste Joseph, Baron de Fourier [20, 21] (1768-1830) which is now known as *Fourier's Theorem* [22]. This theorem states that a periodic function $f(t)$ of period T, can be expressed as a series of harmonic functions given by [22]:

$$f(t) = \frac{A_0}{2} + \sum_{m=1}^{\infty} A_m \cos m2\pi\nu_0 t + \sum_{m=1}^{\infty} B_m \sin m2\pi\nu_0 t, \tag{2.1}$$

where the coefficients, A_m and B_m, are given by

$$\begin{aligned} A_m &= \frac{2}{T}\int_0^T f(t)\cos m2\pi\nu_0 t\ dt \qquad m = 1, 2, 3, ..., \\ B_m &= \frac{2}{T}\int_0^T f(t)\sin m2\pi\nu_0 t\ dt \qquad m = 1, 2, 3, ... \end{aligned} \tag{2.2}$$

Introducing negative values of m into equation 2.1 and expressing it in exponential form, the expression becomes [23]:

$$f(t) = \frac{A_0}{2} + \frac{1}{2}\sum_{m=-\infty}^{\infty} (A_m - iB_m)e^{i2\pi m\nu_0 t} \tag{2.3}$$

$$= \frac{A_0}{2} + \sum_{m=-\infty}^{\infty} C_m e^{i2\pi m\nu_0 t} \tag{2.4}$$

where $C_m = (A_m - iB_m)/2$ which means that the amplitudes of the spectral components are split between positive frequencies represented by positive values of m, and negative frequencies represented by negative values of m.

The descrete representation given by equation 2.1 is replaced by the Fourier integral:

$$f(t) = \left[\int_{-\infty}^{\infty} (A(\nu)\cos 2\pi\nu t + B(\nu)\sin 2\pi\nu t)\ d\nu\right], \tag{2.5}$$

where the coefficients, $A(\nu)$ and $B(\nu)$, are computed using

$$\begin{aligned} A(\nu) &= \int_0^T f(t)\cos 2\pi\nu t \; dt, \\ B(\nu) &= \int_0^T f(t)\sin 2\pi\nu t \; dt. \end{aligned} \tag{2.6}$$

Inspection of equation 2.6 shows that under certain symmetry conditions these coefficients are trivial. For example when the function $f(t)$ is even, $B(\nu) = 0$ for all ν, and its Fourier series will contain only cosine terms, which are themselves even functions. In the same way, when the function $f(t)$ is odd, $A(\nu) = 0$ for all ν, and its Fourier series will contain only sine functions, which are themselves odd functions.

The fourier transform of $f(t)$ is defined, in an exponential form, as follows [24, 23]:

$$F(\nu) = \mathcal{F}\{f(t)\} = \int_{-\infty}^{\infty} f(t)e^{-i2\pi\nu t}dt, \tag{2.7}$$

where $F(\nu)$ is called a Fourier transform of $f(t)$. It is possible to recover $f(t)$ by performing the inverse Fourier transform of $F(\nu)$ in the following way:

$$f(t) = \mathcal{F}^{-1}\{F(\nu)\} = \int_{-\infty}^{\infty} F(\nu)e^{i2\pi\nu t}d\nu. \tag{2.8}$$

Equations 2.7 and 2.8 are called Fourier transform pairs [23]. In this case, time, t, and frequency, ν, were used as Fourier transform variables. Another common Fourier transform pair of variables are position (x) measured in cm, and wavenumber (σ), measured in cm^{-1}.

In practice, the continuous Fourier transform pair given by equations 2.7 and 2.8 is replaced by the discrete Fourier transform pair [23]:

$$F\left(\frac{n}{NT}\right) = \sum_{k=0}^{N-1} f(kT)e^{-i2\pi nk/N} \qquad n = 0, 1, ..., N-1, \tag{2.9}$$

where n and k are the integers, N is the total number of samples of time and T is the sampling interval. The discrete inverse Fourier transform is defined as [23]

$$f(kT) = \frac{1}{N} \sum_{n=0}^{N-1} F\left(\frac{n}{NT}\right) e^{i2\pi nk/N} \qquad k = 0, 1, ..., N-1. \tag{2.10}$$

The next section shows how Fourier analysis can be applied to electromagnetic radiation.

2.3 Fourier decomposition

Electromagnetic radiation can be represented as a transverse wave of orthogonal electric and magnetic fields whose amplitude varies with time. This wave carries information about the source generating it. If the frequencies and amplitudes that make up the wave are known, then the source spectrum can accurately be modelled. The process that separates a time-varying wave into its constituent frequencies is called Fourier decomposition [4]. Some examples are given below.

Figure 2.1 shows three cosine waves of unit amplitude, and frequency 10 Hz but having different phases. The solid trace shows the cosine wave having zero phase, the dash-dot trace shows the cosine wave having a phase shift of $\pi/4$, and the dot-dot trace shows the cosine wave having a phase shift of $\pi/2$, which is of course a sine wave. The next three figures show the complex Fourier transforms (FTs) of these three functions.

Figure 2.2 shows the Fourier transform of the cosine wave having zero phase and it shows that only the real part of the FT is non-zero (because the cosine function is an even function). While the original cosine wave has an amplitude of unity, its Fourier transform yields an amplitude of 0.5. This is because the Fourier transform includes

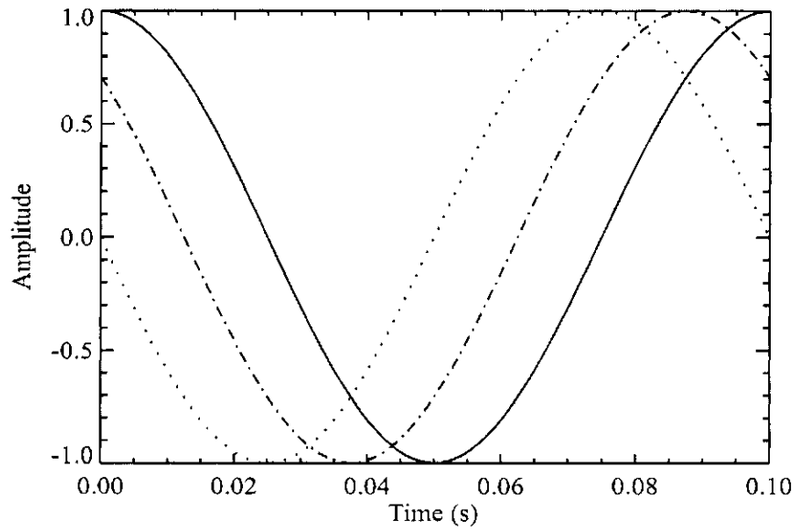

Figure 2.1: Three cosine waves with different phases. solid line - 0 phase, dash-dot line - $\pi/4$ phase, dot-dot line - $\pi/2$ phase

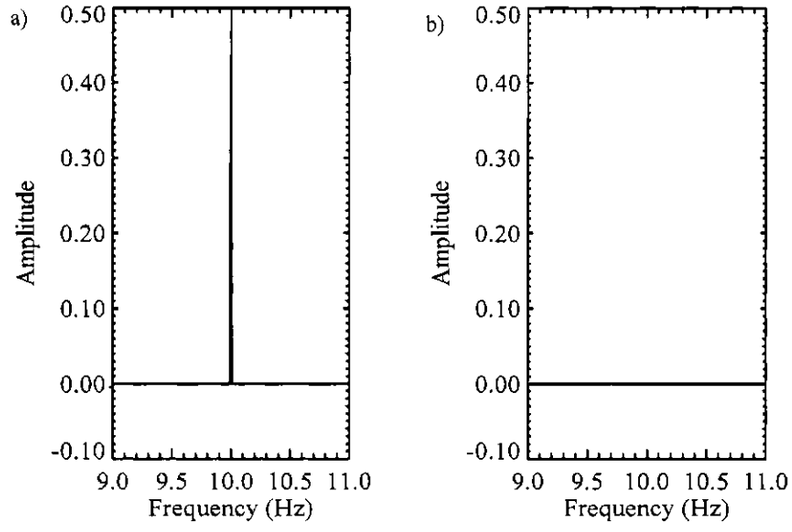

Figure 2.2: Fourier transform of the cosine wave of frequency 10 Hz and phase zero, shown in figure 2.1. a) real part b) imaginary part

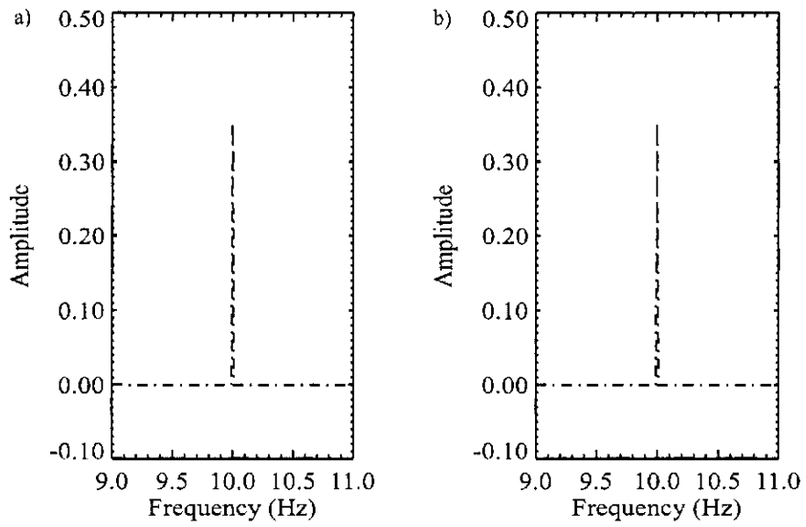

Figure 2.3: Fourier transform of the cosine wave of frequency 10 Hz and phase $\pi/4$ shown in figure 2.1 a) real part b) imaginary part

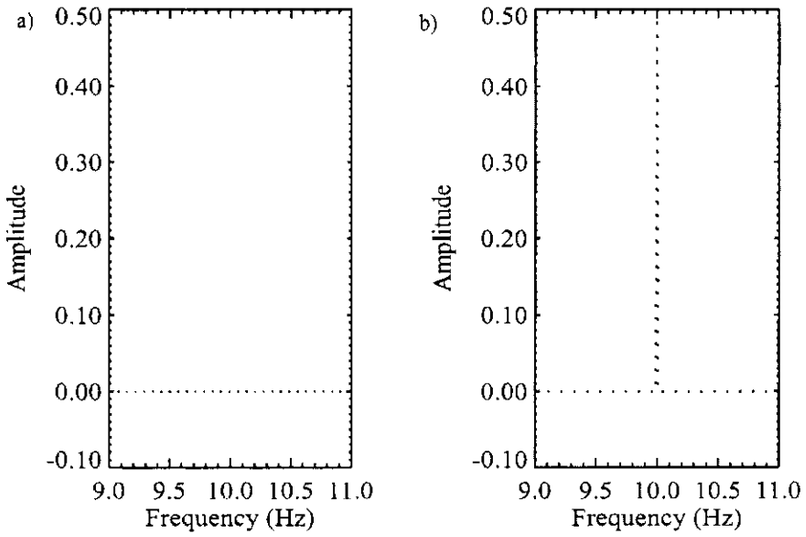

Figure 2.4: Fourier transform of the cosine wave of frequency 10 Hz and phase $\pi/2$ shown in figure 2.1 a) real part b) imaginary part

negative frequencies terms also (equation 2.8), and this part is not included in the graphs. There is another feature at -10 Hz with the same amplitude so the resultant amplitude of the two features is simply the addition of the two, which is equal to unity. To explain this mathematically, $f(t) = A\cos 2\pi\nu_0 t$ is the equation of the cosine form in figure 2.2, where A is the amplitude of the wave and ν_0 is the frequency in Hz. The amplitude of the spectral components of this function is represented by the coefficients A_m and B_m in the Fourier series given by equation 2.2.

$$\begin{aligned} A_m &= \frac{2}{T}\int_0^T f(t)\cos m2\pi\nu_0 t dt \\ &= \frac{2}{T}\int_0^T A\cos 2\pi\nu_0 t\cos m2\pi\nu_0 t dt \\ &= \frac{2A}{T}\frac{T}{2}\delta_{m1} = A\delta_{m1}, \end{aligned}$$

since $\int_0^T A\cos 2\pi\nu_0 t\cos m2\pi\nu_0 t dt = \frac{T}{2}\delta_{m1}$ [22]. Here, δ_{m1} is the Kronecker delta function whose value is 0 everywhere except at $m = 1$, where its value is unity. Coefficients B_m can be caluculated in a similar way:

$$\begin{aligned} B_m &= \frac{2}{T}\int_0^T f(t)\sin m2\pi\nu_0 t dt \\ &= \frac{2}{T}\int_0^T A\cos 2\pi\nu_0 t\sin m2\pi\nu_0 t dt \\ &= 0, \end{aligned}$$

since $\int_0^T A\cos 2\pi\nu_0 t\sin m2\pi\nu_0 t dt = 0$ [22]. Including negative frequencies in equation 2.3, it is easy to see that $C_m = A_m/2$, since B_m is zero. This corresponds to the amplitude, A, being split between positive frequencies, $m = 1$ and negative frequencies, $m = -1$. Therefore, the amplitude at $\nu = 10$ Hz is 0.5 and at $\nu = -10$ Hz is 0.5.

Now if we consider the second function which has a phase shift of $\pi/4$, it is no

longer symmetric about $t = 0$. In this case the Fourier transform, figure 2.3, shows that the real and imaginary components are equal, having amplitudes of 0.35355 units. The total amplitude is then given by the vector sum: $\sqrt{0.35355^2 + 0.35355^2} = 0.5$. Again, when account is taken of the negative frequencies the total amplitude is unity. Finally, by shifting the cosine wave by $\pi/2$ radians we effectively create a sine wave, which, being an odd function, has a non-zero imaginary component of amplitude 0.5.

All of the waves in the previous examples had the same frequency. Now consider what happens when we add two cosine waves *with amplitude* $A = 1$ *unit* but different frequencies of $\nu_1 = 10$ Hz and $\nu_2 = 11$ Hz.

$$\begin{aligned} x_1 &= A\cos(2\pi\nu_1 t) \\ x_2 &= A\cos(2\pi\nu_2 t). \end{aligned} \tag{2.11}$$

Since the two waves are close in frequency the combined wave exhibits the phenomenon of *beats*. The superposition of x_1 and x_2 gives

$$x_1 + x_2 = 2A\cos\left(2\pi\left(\frac{\nu_1 - \nu_2}{2}\right)t\right)\cos\left(2\pi\left(\frac{\nu_1 + \nu_2}{2}\right)t\right). \tag{2.12}$$

The combined wave is seen to be a disturbance having a frequency that is the average of the two frequencies $\frac{\nu_1+\nu_2}{2}$, but with an amplitude that varies with time, as a cosine of the difference between the two waves $\frac{\nu_1-\nu_2}{2}$. This is shown in figure 2.5. The FT of this function is shown in figure 2.6. It shows two features at the frequencies of the original waves.

Finally, consider four waves having different frequencies, amplitudes and phases,

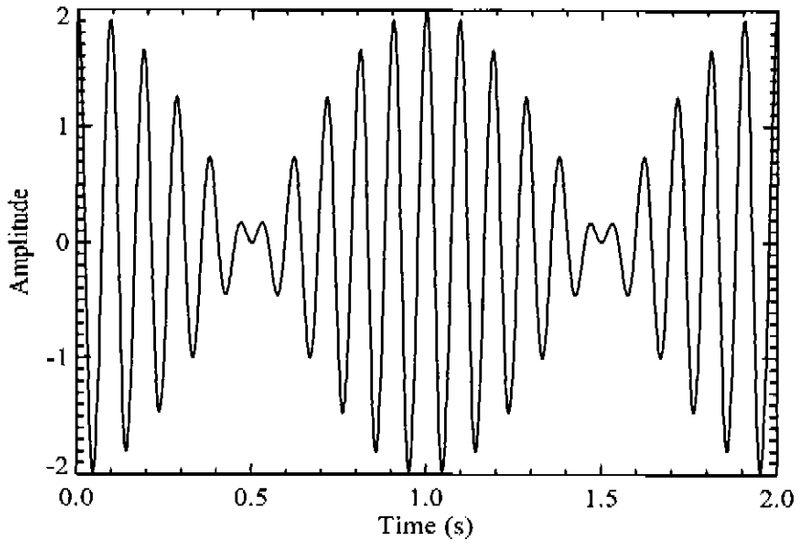

Figure 2.5: The resultant waveform of the superposition of two cosines of frequencies 10 Hz and 11 Hz, equation 2.6.

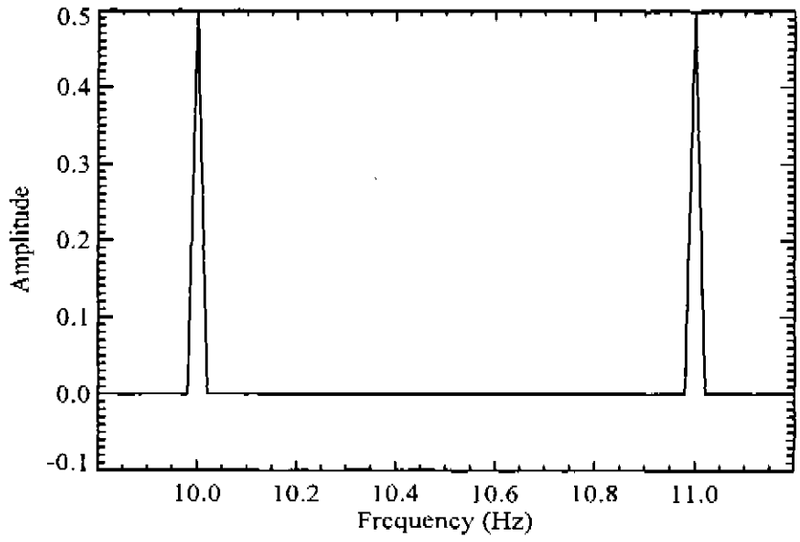

Figure 2.6: The real components of the Fourier transform of the waveform shown in figure 2.5

given by

$$\begin{aligned} x_1 &= \cos(2\pi\nu_1 t) \\ x_2 &= 0.8\cos(2\pi\nu_2 t - \frac{\pi}{4}) \\ x_3 &= 0.5\cos(2\pi\nu_3 t - \frac{\pi}{2}) \\ x_4 &= 0.2\cos(2\pi\nu_4 t - \frac{\pi}{16}), \end{aligned} \tag{2.13}$$

where $\nu_1 = 5$ Hz, $\nu_2 = 12$ Hz, $\nu_3 = 14$ Hz and $\nu_4 = 20$ Hz.

Combining these four waves leads to the function shown in figure 2.7. It is not obvious from inspecting this figure how many components are involved. However, the FT shown in figure 2.8 clearly shows the individual spectral components at frequencies of 5, 12 and 20 Hz in the real domain and the spectral components in the imaginary domain at frequencies of 12, 14 and 20 Hz. This shows that the original function is the superposition of four sinusoids. Since the 5 Hz component only shows up in the real domain the original component was thus a cosine function. Similarly the 14 Hz component, being purely imaginary, represents a sine function. The other two components are complex and represent sinusoids of different phases. The phases of these components can be determined from the arctangent of the imaginary divided by the real component. The amplitudes of the four functions can be determined as described above.

As discussed in chapter 1, spectra can consist of continuum or line, emission or absorption. A more realistic spectrum is shown in figure 2.9. The line at 2.5 Hz is a narrow emission line which occurs when atoms or molecules emit electromagnetic radiation during changes from excited states to states of lower energy. On the right is an absorption line at 6.5 Hz which occurs when radiant energy is absorbed by the medium through which

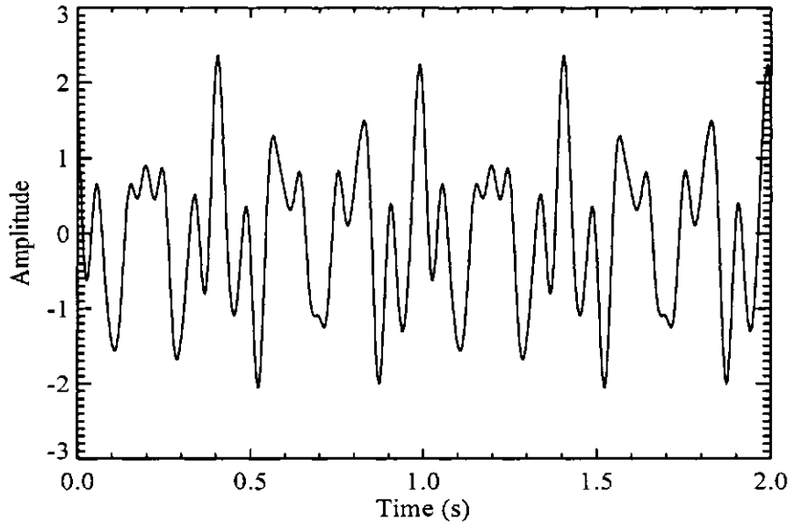

Figure 2.7: The resultant waveform of the four cosine waves given in equation 2.7. These waves have different amplitudes, frequencies and phases.

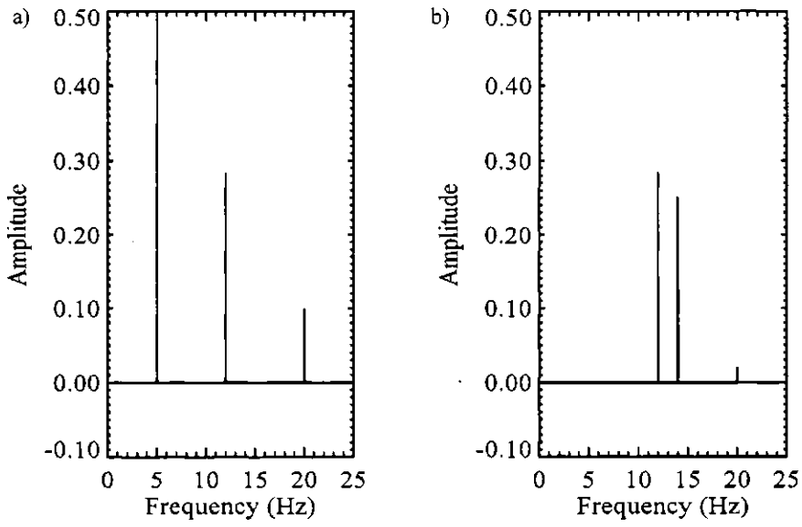

Figure 2.8: Fourier transform of the waveform in the equation 2.7 a) real part b) imaginary part

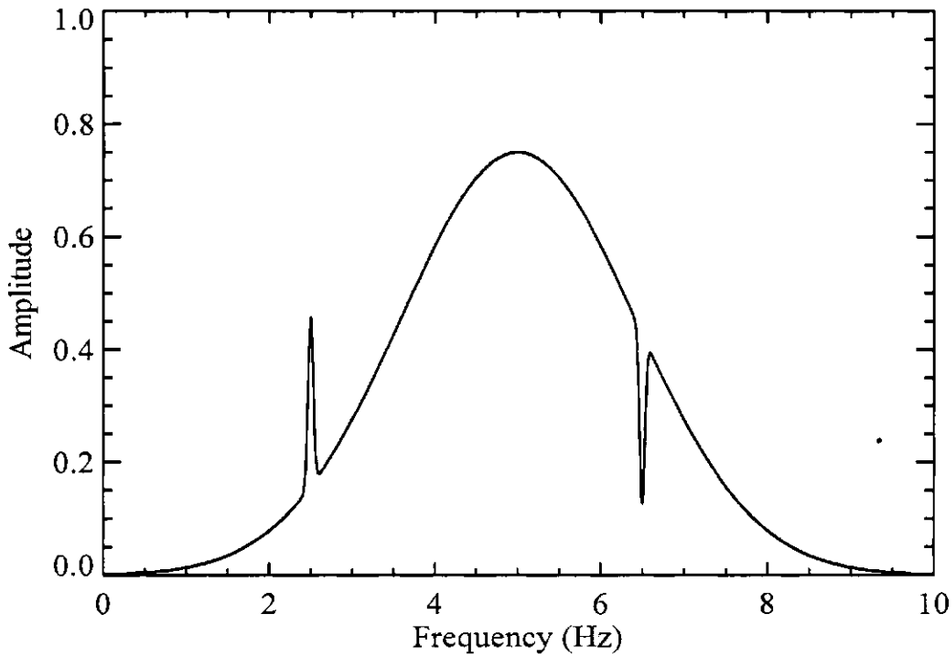

Figure 2.9: A more realistic spectrum: a narrow emission line at 2.5 Hz and a narrow absorption line at 6.5 Hz superimposed on a broad emission feature centered at 5 Hz.

it is passing. Both lines are superimposed on a broader emission feature centered at 5 Hz. The Fourier components of such a spectrum are manifold.

FTS spectroscopy is a method of obtaining intermediate to high resolution spectroscopic measurements on the incident radiation field [4, 5, 25]. A Fourier spectrometer is a multiplex instrument, which means that the detector simultaneously records the intensity of the source at all wavelengths at all times. The FTS is a two beam interferometer which operates on the principle of the light interference. The intensity of the interference fringes depends on the optical path difference between the two beams of the interferometer. The variation in the intensity of these fringes as a function of optical path difference is known

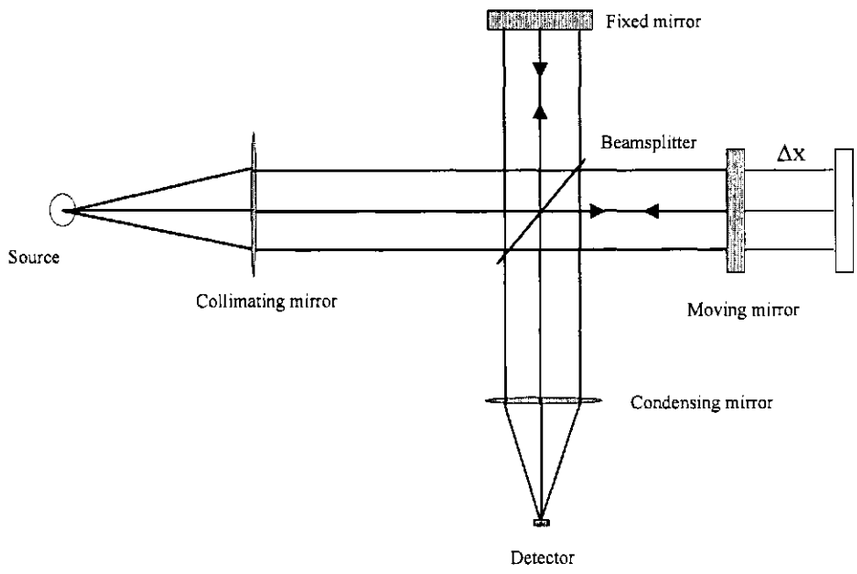

Figure 2.10:

as the *interferogram*. Finally, the spectrum is computed from the Fourier transformation of the interferogram.

2.4 The Michelson interferometer

The simplest form of a FTS is a Michelson interferometer [4, 22, 26] shown in figure 2.10.

The Michelson interferometer works on the principle of amplitude division. Light from a source enters the interferometer and it is collimated by a lens or mirror. The resulting plane wave is then split into two equal amplitude waves by the beamsplitter. These waves

are reflected back on themselves by two mirrors, one fixed and one movable. These reflected two beams are recombined at the beamsplitter where they form two resultant beams, one travelling back to the source and the other one to the detector. These recombined beams interfere with each other at the detector to produce intensity variations that depend on the optical path difference between the recombined beams; the optical path difference being varied by the motion of the moving mirror. Different frequency components in the beam will experience different phase shifts and therefore different levels of interference. When the optical path difference is zero, however, all frequency components exhibit zero phase difference and constructive interference occurs simultaneously for all wavelengths; this position is called the zero path difference (ZPD) position.

2.4.1 Monochromatic beam

Let us consider a monochromatic beam entering the interferometer. The beam is divided into two beams by the beamsplitter. The electric fields describing these two beams can be written as

$$\begin{aligned} E_1 &= E_0 e^{i\omega t} r_m r_b t' e^{-2\pi i \sigma x_1} \\ E_2 &= E_0 e^{i\omega t} r_m r_b t' e^{-2\pi i \sigma x_2}. \end{aligned} \tag{2.14}$$

In this equation, E_0 is the amplitude of the incident electromagnetic wave of angular frequency $\omega = 2\pi\nu$; r_m is the amplitude reflection coefficient of the mirrors, r_b is the amplitude reflection coefficient of the beamsplitter, t' is the amplitude transmission coefficient of the beamsplitter, and x_1 and x_2 are the optical path length travelled by the two beams respectively. The total electric field at the detector is given by adding the two individual electric

fields in the above equation

$$E_T = E_1 + E_2 = E_0 e^{i\omega t} r_m r_b t' (e^{-2\pi i \sigma x_1} + e^{-2\pi i \sigma x_2}). \tag{2.15}$$

The total intensity measured at the detector, known as the interferogram, is defined as the square of the magnitude of the total electric field [4]

$$I(x_1 - x_2) = |E_T|^2 = 2E_0^2 R_m R_b T(1 + \cos(2\pi\sigma(x_1 - x_2))), \tag{2.16}$$

where $R_m = r_m^2$ is the reflectance of the mirrors, $R_b = r_b^2$ is the reflectance of the beamsplitter, $T = t'^2$ is the transmittance of the beamsplitter and $x_1 - x_2$ is the optical path difference which can be expressed as δ. In the case of an ideal interferometer, the beamsplitter reflects and transmits 50 % of the incident light and the interferogram can be written as

$$I_0(\delta) \propto B(\sigma)\left[1 + \cos(2\pi\sigma\delta)\right], \tag{2.17}$$

where $E_0^2 = B(\sigma)$ is the spectrum, and σ is the wavenumber (cm^{-1}) The interferogram is seen to be composed of a constant (DC) term and a modulation term, which is given by the cosine function.

2.4.2 Polychromatic beam

When the source contains more than one frequency, the resultant interferogram is the superposition of the interferograms for each frequency, ie.

$$I_0(\delta) \propto \int_{-\infty}^{\infty} B(\sigma)\left[1 + \cos(2\pi\sigma\delta)\right] d\sigma. \tag{2.18}$$

It is customary to neglect the constant (DC) component and express the interferogram as

$$I(\delta) \propto \int_{-\infty}^{\infty} B(\sigma)\cos(2\pi\sigma\delta) d\sigma. \tag{2.19}$$

This is the cosine Fourier transform of the source spectrum $B(\sigma)$. The spectrum can be recovered by the inverse cosine Fourier transform

$$B(\sigma) \propto \int_{-\infty}^{\infty} I(\delta)\cos(2\pi\sigma\delta)d\delta. \tag{2.20}$$

As discussed earlier, when the inverse cosine Fourier transform of an interferogram is taken, in addition to the positive frequency spectrum $B(\sigma)$, the negative frequency spectrum $B(-\sigma)$ is produced. The negative frequencies have no physical interpretation but they play an important role when we want to transform back and forth between the interferogram and spectral domains.

2.4.3 Non-ideal Fourier transform spectroscopy

All of the previous equations were derived assuming ideal conditions. In the real world however, we have to consider non-ideal interferometers of finite length. The finite length of an interferometer limits the maximum optical path difference, which in turn limits the resolution. Furthermore, phase shifts are introduced that make the interferograms asymmetric (phase shifts will be discussed later in this chapter). Interferograms are no longer even functions but rather a mixture of even and odd functions and are analyzed using the complex Fourier transform defined as [4]

$$B(\sigma) = \int_{-L}^{L} I(\delta)e^{-2\pi i\sigma\delta}d\delta, \tag{2.21}$$

where L is the maximum optical path difference and the resulting $B(\sigma)$ will now be complex.

2.5 Sampling the interferogram

In order to compute the spectrum from 0 to ∞ wavenumbers, the interferogram would have to be sampled at infinitesimally small increments of optical path difference. In practice, the interferogram is sampled at finite intervals of optical path difference. The Nyquist sampling theorem states that in order to unambiguously reconstruct the spectrum the interferogram must be sampled at twice the Nyquist frequency which is shown in the following equation:

$$\Delta x = \frac{1}{2\sigma_N}. \tag{2.22}$$

Here, Δx is the optical path difference increment in cm and σ_N is the Nyquist frequency in cm^{-1}. If an interferogram is sampled at regular discrete path differences, the continuous interferogram is multiplied by a repetitive impulse function which is an infinite series of Dirac delta functions spaced at intervals $1/x$, where x is the optical path difference in cm [4]. The equation of this impulse function is given by equation 2.23.

$$III_{1/x}(\delta) = \frac{1}{x} \sum_{n=-\infty}^{\infty} \Delta\left(\delta - \frac{n}{x}\right). \tag{2.23}$$

Here Δ is the Dirac delta function and $III_{1/x}(\delta)$ is the Dirac delta comb function, also known as Shah function, expressed as a function of optical path difference. The Fourier transform of a Dirac delta comb is another Dirac delta comb function [4] of period x instead of $1/x$ shown in equation 2.24

$$III_x(\sigma) = x \sum_{n=-\infty}^{\infty} \Delta\left(\delta - nx\right). \tag{2.24}$$

One of the most important properties of Fourier transforms is that multiplication in one domain is equivalent to convolution in the inverse domain and vice versa (section 4.2).

Therefore, when the Fourier transform of the discretely sampled interferogram is taken, this is equivalent to convolving the spectrum with the Fourier transform of the sampled comb. The effect of this convolution is that the spectrum is repeated indefinitely. If the bandwidth of the spectrum is 0 to $\sigma_{\max}$, then the period of the transformed comb must be at least twice this maximum frequency, known as the Nyquist frequency, in order to avoid aliasing.

If the sampling frequency was decreased so that signal was sampled at $1/\sigma_N$ instead of $1/2\sigma_N$, for example, the transformed spectra would overlap and some spectral features would occur at incorrect frequencies. This phenomenon is called *aliasing* or *folding* and it is shown in figure 2.11.

For example, if there is a spectral feature at $\sigma_{\max} + \sigma$, then another feature will appear at $\sigma_{\max} - \sigma$. This situation must be avoided since in general it is no longer possible to recover spectral information.

2.6 Resolution

In practice, interferograms can only be measured to finite maximum optical path difference, L, determined by the length of the translation stage. This is equivalent to multiplying the infinitely long interferogram by the top hat truncation function given in figure 2.12.

This in turn is equivalent to convolving the entire spectrum with the Fourier transform of the boxcar function, which is the sinc function shown in equation 4.5, more generally known as *instrumental line shape* (ILS) function. When the spectrum consists of

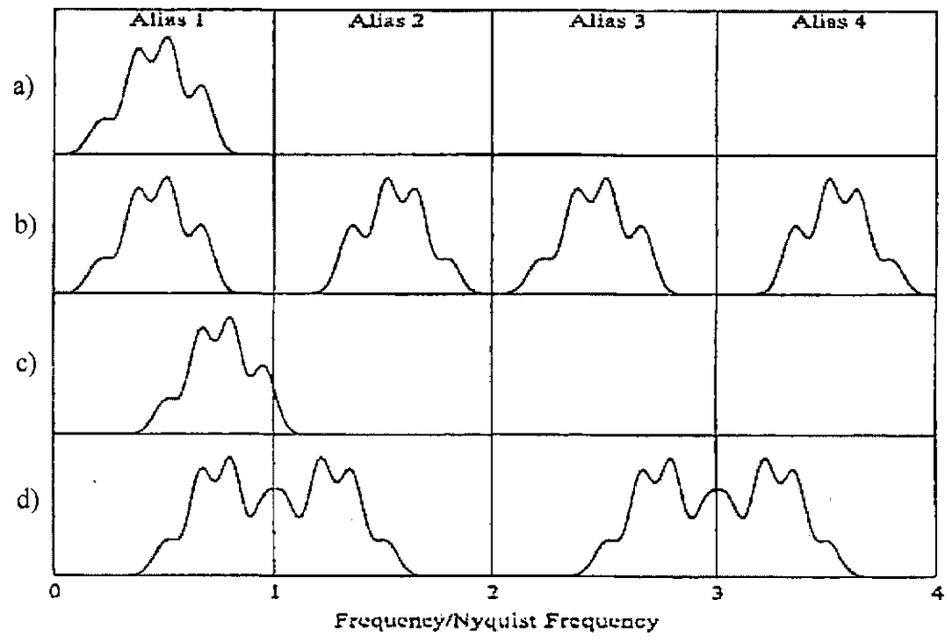

Figure 2.11: a) input spectrum, b) output spectrum, after proper sampling, c) input spectrum that exceeds the Nyquist frequency, d) output spectrum after improper sampling [4]

two closely spaced lines it can often be difficult to resolve them. There are many definitions of resolution. Two common ones are based on the full width at half-max (FWHM) of the ILS and the Rayleigh criterion [25, 27].

The FWHM criterion states that two individual lines are resolved when the spacing between the lines is equal to or greater than the FWHM of the ILS. As will be shown in section 4.2 the FWHM of a sinc function is $1.21/2L$ where L is the maximum optical path difference. For example, figure 2.14 shows two sinc functions which are separated by a frequency of $1/2L$; it is obvious from the graph that these two lines are not resolved. By comparison, figure 2.15 shows that when the two lines are separated by a frequency

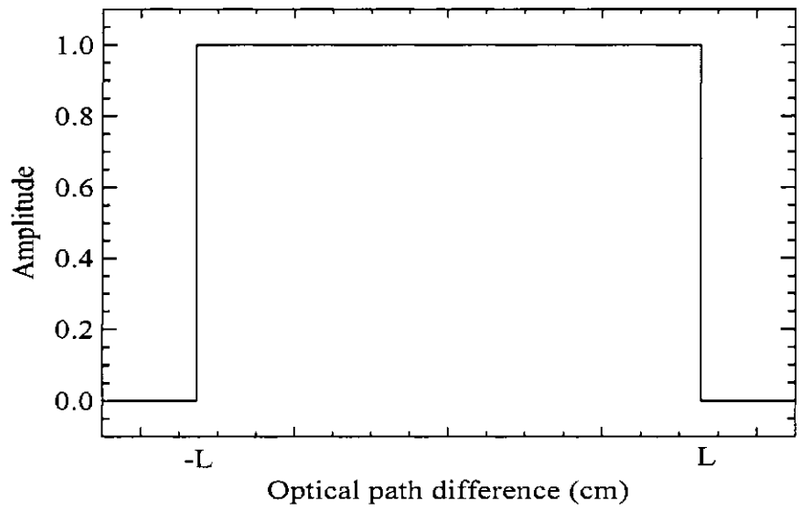

Figure 2.12: Top hat function as a function of maximum optical path difference

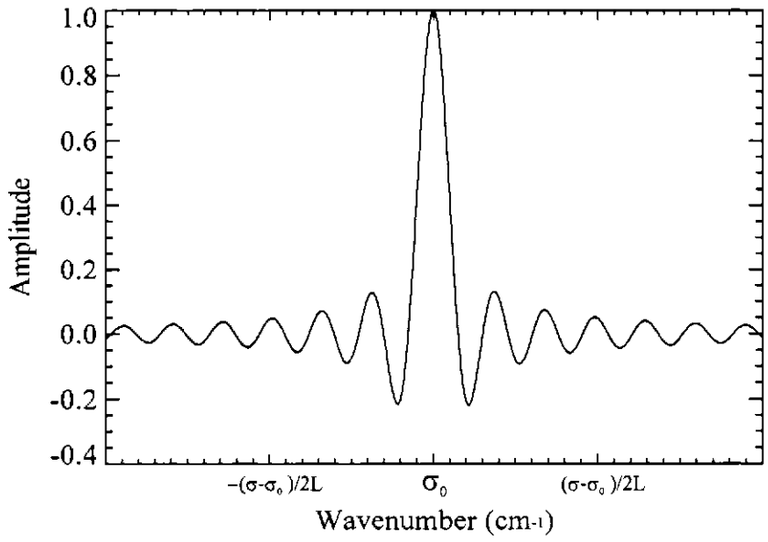

Figure 2.13: The Fourier transform of a top hat function, known as a sinc function.

of $1.21/2L$ we are just able to discern that there are at least two features present. The Rayleigh criterion [28] considers that two lines are resolved when the resultant curve has a ~20 % dip of the peak amplitude of the line, or in another words the resultant line amplitude at the midpoint between the lines is $\frac{8}{\pi^2}$ times the peak amplitude . The Rayleigh criterion is shown in figure 2.16 for the case of the two $\text{sinc}^2 x$ ILSs. It can be seen that this is also equivalent to the case in which the maximum of the one line falls on the first minimum of the other [28].

The resolving power of a spectrometer is defined as [4]

$$R \equiv \frac{\sigma}{\delta\sigma}. \tag{2.25}$$

Since $\delta\sigma$ is proportional to $1/2L$ as discussed above, it can be seen that the resolving power is determined by the maximum optical path difference, L.

2.7 Jacquinot's advantage [1]

The throughput of an FTS is defined as the product of the area of the input light beam A (m^2) and the solid angle Ω (str) contained within the beam; sometimes this quantity is called the étendue or light grasp. The controlling factor for the throughput is usually the most expensive component of the spectrometer; in the case of an FTS this is the beamsplitter. All interferometers possessing circular symmetry (eg. FTS or Fabry Perot interferometer) have significantly higher throughput or optical efficiency, compared with dispersive spectrometers, like a grating spectrometer, where the areal component of the throughput is determined by the narrow entrance and exit slits (see section 2.11.1). The high throughput of the FTS is known as the Jacquinot advantage. As will be seen in

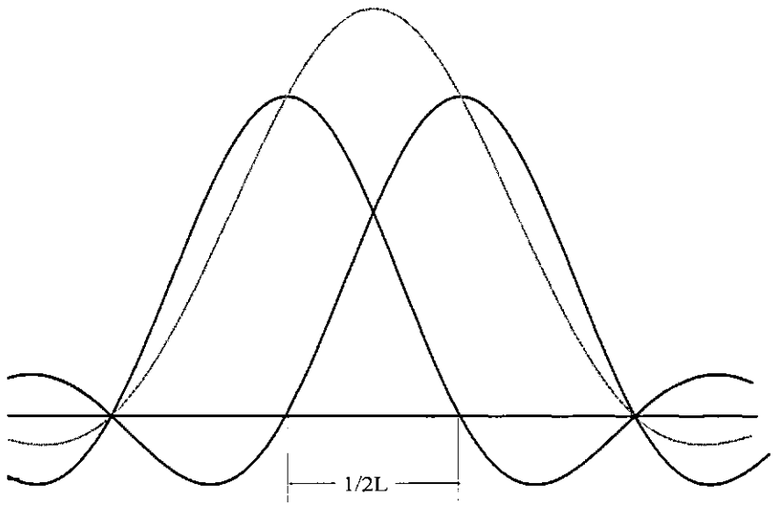

Figure 2.14: The resultant of two sinc functions of equal amplitudes separated by a frequency of 1/2L. Features are unresolved in the resultant function

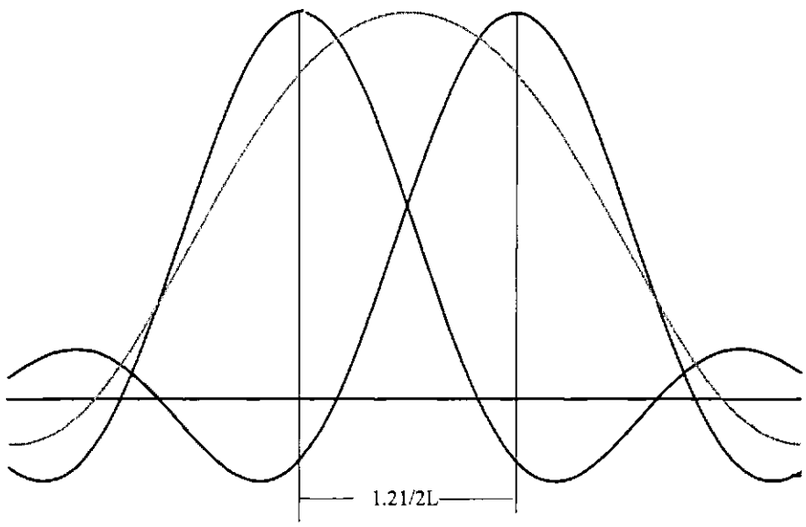

Figure 2.15: The resultant of two sinc functions of equal amplitudes separated by a frequency of 1.21/2L apart. One starts to discern the two component nature of the result.

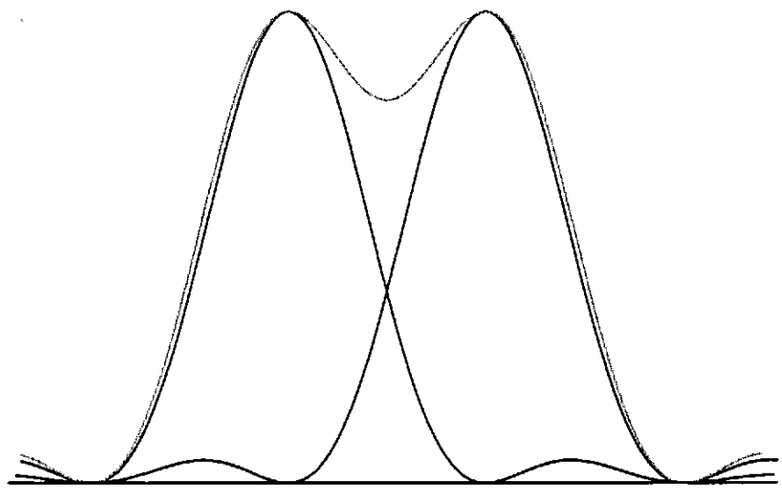

Figure 2.16: The resultant of two sinc^2 functions centered 1/L cm^{-1} apart, with each of the sinc^2 functions shown as a black line.

section 4.3, while in principle one can increase the throughput by increasing the divergence angle within the FTS this results in a natural apodization of the interferogram, which limits the maximum attainable resolution.

2.8 Fellgett's advantage [2]

In a dispersive spectrometer only a narrow range of wavelengths are measured at a given instant. By comparison, in an FTS all source wavelengths are measured at all times. This leads to a multiplex advantage also known as Fellgett's advantage. The multiplex advantage can be explained in the following way: Suppose we are interested in measuring the spectrum between σ_1 and σ_2 with a resolution $\delta\sigma$ (cm^{-1}). The number of spectral

elements, M, in the band is given by

$$M = (\sigma_2 - \sigma_1)/\delta\sigma. \tag{2.26}$$

If a grating spectrometer is used then each small band of width $\delta\sigma$ can be observed for a time T/M where T is the total time required to scan the full spectrum from σ_1 to σ_2. This means that the integrated signal received in a small band $\delta\sigma$ is proportional to T/M. If the noise is random and does not depend on the signal, then the signal noise should be proportional to $(T/M)^{1/2}$. Therefore, the signal-to-noise ratio for a grating spectrometer is [27]

$$(S/N)_G \propto (T/M)^{1/2}. \tag{2.27}$$

On the other hand, an FTS measures all wavelengths at all times. So the integrated signal in a small band $\delta\sigma$ is proportional to T and the signal noise is proportional to $T^{1/2}$. Thus, for an interferometer, the signal-to-noise ratio would be [27]

$$(S/N)_I \propto T^{1/2}. \tag{2.28}$$

If the grating and an FTS have an identical throughput then the ratio of the S/N for the two instruments can be written:

$$\frac{(S/N)_I}{(S/N)_G} = M^{1/2}. \tag{2.29}$$

Since M is the number of spectral elements of width $\delta\sigma$, equation 2.29 indicates that the interferometer has a much higher signal-to-noise ratio than a grating spectrometer. Moreover, it should be noted that the throughput of an FTS is typically two orders of magnitude larger than the grating, which leads to an even greater increase in signal-to-noise

ratio. Advances in detector array technology allow grating spectrometers to observe entire spectral ranges simultaneously; however, the FTS can use the same detector to observe many spatial parts of the source so the gain is retained [27].

2.9 Phase correction

In earlier sections ideal interferometers were considered, which produce interferograms that are real and symmetric, and thus whose spectrum is a cosine Fourier transform of a symmetric interferogram. In this case, the sine transform is zero and the phase is also zero. Practically, however, asymmetries are often unavoidably introduced into the interferogram, which result in the phase errors in the spectrum [29, 30, 31, 32]. If left uncorrected these phase errors yield to errors in the positions, intensities and shapes of spectral features because phase errors take the energy out of the real part of the spectrum and put it in the imaginary part [4]. The spectral information from the imaginary part needs to be brought back into real part of the spectrum. In order to recover the true spectrum, we must first determine the phase error.

An ideal Fourier transform spectrometer produces a sampled interferogram described by [4]

$$I(\delta_n) = \sum_{j=1}^{N} B(\sigma_j) \cos 2\pi\sigma_j\delta_n. \tag{2.30}$$

Here, $I(\delta_n)$ is one of the samples of the interferogram taken at the optical path difference of δ_n. In a non-ideal case, an interferogram must be written in a more general form to

incorporate the asymmetries [4]

$$I(\delta_n) = \sum_{j=-N}^{N} B(\sigma_j) e^{-i(2\pi\sigma_j\delta_n + \phi_{tot}(\sigma_j))}, \tag{2.31}$$

where $\phi_{tot}(\sigma_j)$ is the total phase shift. The presence of phase shifts means that the exponent in equation 2.31 does not go to zero at zero optical path difference (ZPD) plus it has a wavenumber dependence. The phase of a spectrum can be expressed as a polynomial of wavenumber σ:

$$\phi_{tot}(\sigma) = a + b\sigma + c\sigma^2 + d\sigma^3 + e\sigma^4 + ... \tag{2.32}$$

This phase function can be represented as a linear combination of three physical components: a component due to missampling the position of ZPD, a contribution due to the spectrometer beamsplitter, and a contribution from other sources (e.g. detector or electronics). The overall measured phase can therefore be expressed as:

$$\phi_{tot}(\sigma) = \phi_{ZPD} + \phi_{BS} + \phi_{OTHER}, \tag{2.33}$$

where $\phi_{ZPD} = 2\pi\sigma\Delta x$ is the phase term that arises from missampling the ZPD position by an amount Δx, ϕ_{BS} is the contribution due to the beamsplitter, generally non-linear, and ϕ_{OTHER} is the contribution due to all other sources (detector, pre-amplifier etc.).

These phase errors lead to asymmetries in the interferogram. The phase correction method of Forman et al. [33] has been adopted. The key steps are described below:

Step 1: Extract the double-sided portion of the interferogram (i.e., equal distance on both sides of ZPD),

Step 2: Perform a complex FT on the double-sided interferogram. It will return both real and imaginary components,

Step 3: Compute the spectral phase from:

$$\phi(\sigma) = \arctan\left(\frac{\mathrm{Im}(FT)}{\mathrm{Re}(FT)}\right). \tag{2.34}$$

Step 4: Fit a low order polynomial to the phase data, weighted by the amplitude of the spectrum,

Step 5: Take the inverse FT of $\exp(-i\phi(\sigma))$ to get the phase correction function (PCF) ie., $PCF = \int_{-\infty}^{+\infty} e^{-i\phi(\sigma)} e^{2\pi i\sigma\delta} d\sigma$.

Step 6: Convolve the PCF with the original interferogram to generate a symmetric phase-corrected interferogram, which can be subsequently analyzed to produce the final spectrum.

Phase correction is implemented as part of the processing pipeline that has been developed for use with the U of L FTS. Details of this are given in chapter 3.

2.10 Mach-Zehnder Fourier transform spectrometer

The FTS used to collect these data was built by Dr. Naylor's group at the U of L [34]. This FTS uses two broadband intensity beamsplitters in a Mach-Zehnder configuration, which provides access to all four interferometer ports while maintaining a high and uniform efficiency over a broad spectral range. The layout of this spectrometer is shown in figure 2.17 and the laboratory view is shown in figure 2.18.

The interferometer is constructed on a damped optical breadboard. All mirrors are made from uncoated diamond-turned aluminum [5]. Two flat mirrors (M1 and M2) focus the beam at the first beamsplitter (BS1) for each of the two input ports. The reflected and transmitted beams from the beamsplitter are collimated by spherical concave mirrors

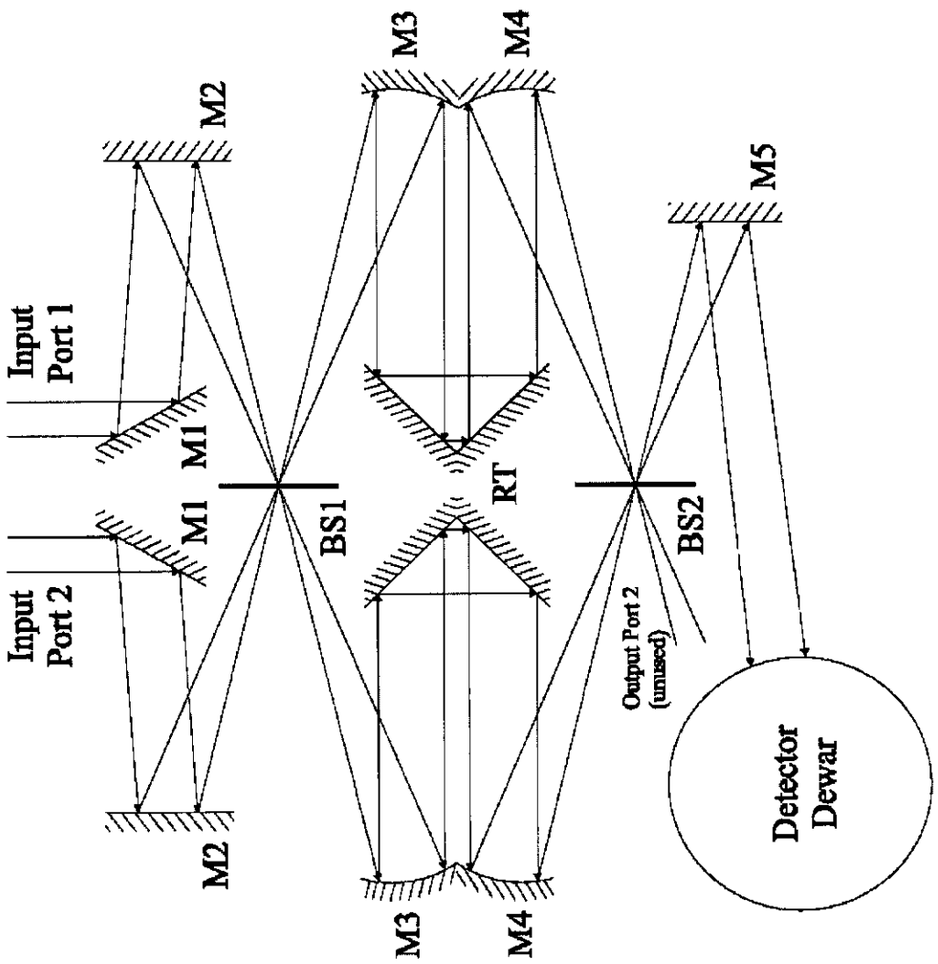

Figure 2.17: A schematic of the University of Lethbridge Mach-Zehnder FTS. M1, M2 and M5 are plane mirrors, M3 and M4 are powered mirrors, RT are the roof-top mirrors, and BS1 and BS2 are input and output intensity beam dividers [5].

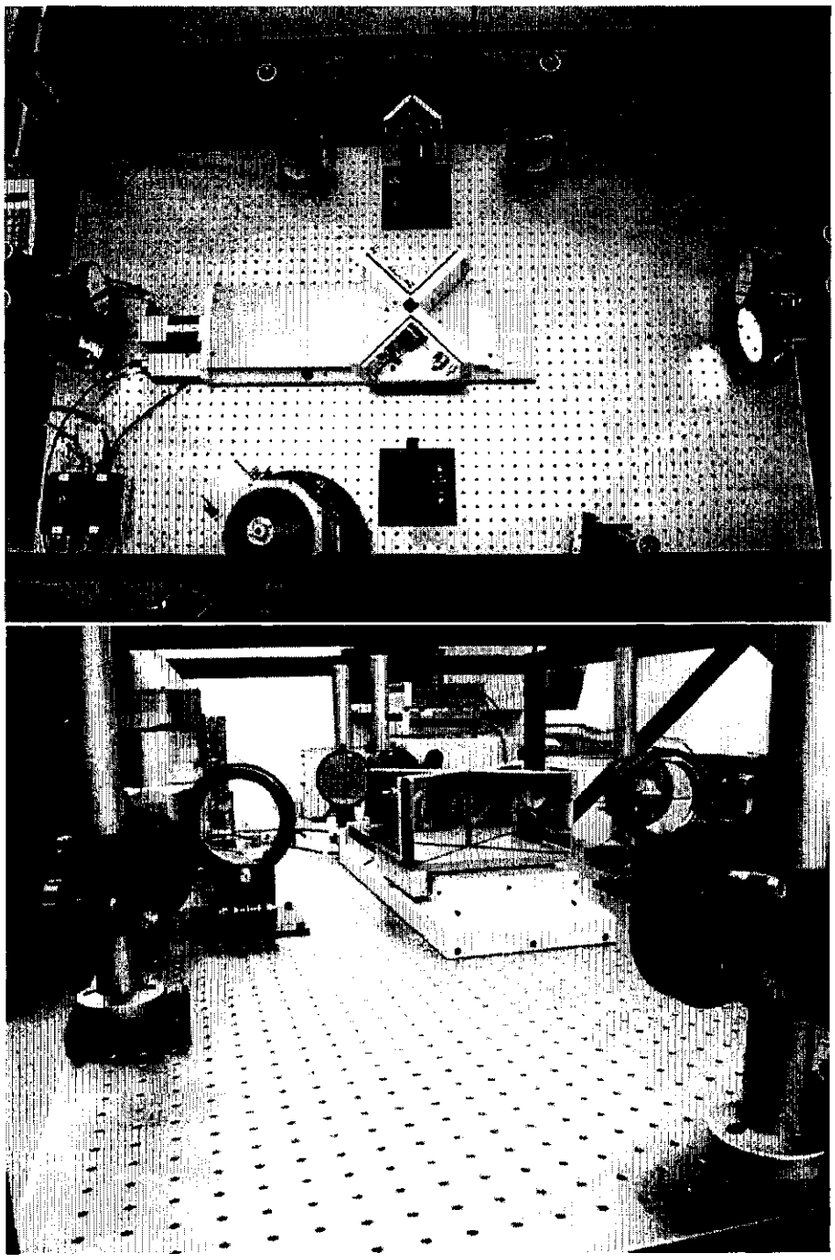

Figure 2.18: Top and side views of the U of L Mach-Zehnder FTS in the laboratory [5].

M3. These beams travel to roof-top mirrors (RT) which are placed back-to-back on the translation stage, which provides a travel of 300 mm. This in turn provides a maximum optical path difference between the interfering beams of 1.2 m. The optical path difference multiplication factor of 4 provides a spectral resolution of 0.005 cm^{-1}. The beam divergence within the interferometer is designed to satisfy the Jacquinot criteria ($R\Omega = 2\pi$) so that the beam divergence, Ω, does not compromise the maximum attainable resolving power, R, of $\tilde{}10^4$. Mirrors M4 focus the beam on the second beamsplitter (BS2), which then directs the beam to a flat mirror M5 before it enters the detector dewar.

By using powered mirrors within the arms of the interferometer, the size of the optical beam at the beamsplitter is minimized. Since the size of the beamsplitter is a limiting factor of any FTS, this design is well suited for imaging Fourier transform spectroscopy as evidenced by its adoption for the FTS under development for the SCUBA-2 camera [35] and the SPIRE instrument on Herschel [36].

2.11 Comparison with other spectrometers

For completeness this section will compare and contrast FTSs with two different spectrometers found in common use: a grating spectrometer and a Fabry-Perot spectrometer. Comparing the FTS with these two spectrometers will give us some insight as to why FTSs find use in astronomical applications.

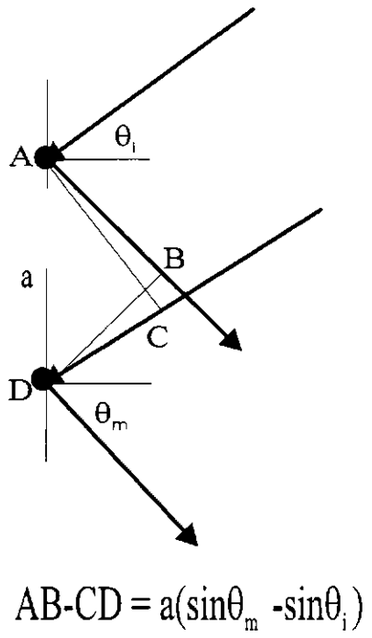

Figure 2.19: A schematic of a reflection grating having a groove spacing of a. Two rays are shown incident at angle θ_i. The optical path difference between the two exiting rays at diffracted at angle θ_m is AB-CD.

2.11.1 Grating spectrometer

A diffraction grating [22, 26, 37, 38] is made out of a large number of close and equally spaced lines that are ruled on plane or concave surfaces. The diffraction gratings can be ruled on a surface, be formed by replicating the ruled surface, or generated by etching a suitably prepared coating as in a holographic grating. When monochromatic light is incident on a grating surface, it is diffracted into discrete directions.

The entrance slit controls the field of the source and the throughput. The incident light passes through the entrance slit and the collimating mirror collimates the beam so that

the light rays are parallel when they reach the grating. The focusing mirror displays the spectrum in the focal plane, and a portion of that spectrum passes through the exit slit and reaches the detector. Figure 2.19 shows the geometry of a diffraction grating.

This figure shows a light ray of wavelength λ incident at an angle θ_i and diffracted by a grating along angles θ_m. a is the groove spacing. The angles are measured from the normal of the grating. The path difference between contributions from adjacent grooves to a wave diffracted at angle θ_m is [22]

$$l = a(\sin\theta_i + \sin\theta_m). \tag{2.35}$$

The path difference is denoted by AB - CD. The principle of interference says that when this path difference equals an integer multiple of the wavelength of light, reflections from adjacent grooves will be in phase and this will lead to constructive interference given by the equation $m\lambda = l$, where m is an integer that represents the order of interference. Combining these leads to the grating equation [22]

$$m\lambda = a(\sin\theta_i + \sin\theta_m). \tag{2.36}$$

From the grating equation we can see that different diffracting orders overlap. For example, if we have a line of 600 nm in the first order, it will be diffracted at the same angle as a line of 300 nm in the second order or the line of 200 nm in the third order. If we have two lines of wavelengths λ and $\lambda + \Delta\lambda$, and they coincide in successive orders, then we have the following relationship

$$(m+1)\lambda = m(\lambda + \Delta\lambda). \tag{2.37}$$

This wavelength difference, at which wavelength measured in one order coincides with a slightly different wavelength $\lambda + \Delta\lambda$ observed in the next lowest order is known as *free*

spectral range

$$(\Delta\lambda)_{fsr} = \frac{\lambda}{m}. \tag{2.38}$$

The free spectral range is the range of wavelengths that can be studied uniquely without contamination from overlapping orders.

The resolving power of a diffraction grating can also be expressed as [4]

$$R = mN, \tag{2.39}$$

where N is the number of grooves illuminated on the surface of the grating. The ability of a grating to resolve two closely spaced lines in a spectrum depends on the dispersion of the grating and the angular interval in the focal plane over which a single wavelength is spread. The smallest angle that can be subtended by a single wavelength is given by the diffraction limit [22]

$$\Delta\theta_i \sim \frac{\lambda}{D}. \tag{2.40}$$

In this formula, D is the diameter of the beam incident on the grating. In order for a grating spectrometer to attain its best resolution, it must be used near the diffraction limit. This requires that the range of incident angles at the grating be small, which in turn limits the width of the entrance slit, and thus the throughput and consequently the overall efficiency. A common grating spectrometer configuration is shown in figure 2.20. In astronomical spectroscopy at submillimetre wavelengths (350 – 1100 μm) diffraction gratings are seldom used. For example, let us use equation 2.39 to determine the size of the grating that will achieve the resolving power of 10^4, the resolving power of the FTS used in this thesis. If we choose to work in the first order we require N = 10^4 lines on the grating, and since the separation between these lines, a, is of the order of one wavelength, the length of the grating

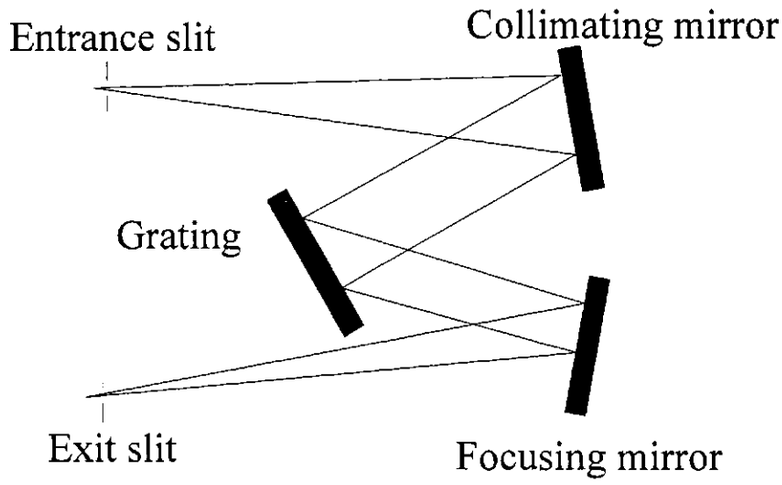

Figure 2.20: Czerny-Turner diffraction grating: the grating provides dispersion and the mirrors provide focusing

is $Na = 11$ m. Moreover, in order to minimize self-emission this grating would require cryogenic cooling, a situation that is clearly impractical. When operating in the first order, the grating spectrometer has a large free spectral range, however its low throughput and single wavelength operation are particularly disadvantageous when trying to measure the spectrum of a weak astronomical source.

2.11.2 Fabry-Perot interferometer

In contrast to an FTS, which operates on the principle of two beam interference, a Fabry-Perot interferometer [22, 26] is a high-resolution spectrometer which operates on the principle of multiple beam interference. Figure 2.21 shows a schematic of a Fabry-Perot interferometer, which consists of two plane, parallel, highly reflective surfaces separated

by a distance d. The enclosed air gap typically ranges from several millimetres to several centimetres. If the gap can be varied by moving one of the mirrors, then it is referred to as an interferometer. When the mirrors are held fixed then it is referred to as an 'etalon'. All rays incident on the Fabry-Perot at a given angle, θ, will result in a single circular fringe when projected onto the screen by the focusing lens. The interference bands will be narrow concentric rings, corresponding to the multiple-beam transmission pattern [22]. The equation that describes the transmitted intensity, $\frac{I_t}{I_i}$, that is projected onto the screen is given by [22];

$$\frac{I_t}{I_i} = \left(\frac{T}{1-R}\right)^2 \frac{1}{1+[4R/(1-R)^2]\sin^2(\delta/2)}, \tag{2.41}$$

where R is the reflectance, T is the transmittance and δ, the phase difference, is given by

$$\delta = \frac{2\pi}{\lambda}\Lambda + 2\phi = \frac{4\pi n_f}{\lambda} d\cos\theta + 2\phi, \tag{2.42}$$

where Λ is the optical path difference and ϕ is an additional phase.

A Fabry-Perot interferometer is a multiple beam interferometer, capable of extremely high resolution in the near infrared. It operates on the principle of amplitude division interferometry, which means that the interfering beams are produced by splitting the incoming beam at a partially reflecting surface. In a Fabry-Perot interferometer, a series of such beams is produced by multiple reflections between two parallel plates with partially reflecting coatings.

In common with the FTS the Fabry-Perot interferometer has cylindrical symmetry, and thus much higher throughput than the grating spectrometer. While the use of multiply reflected beams leads to a compact design for the Fabry-Perot interferometer, it does place high tolerance demands on the optomechanical design. The resolving power of a Fabry-

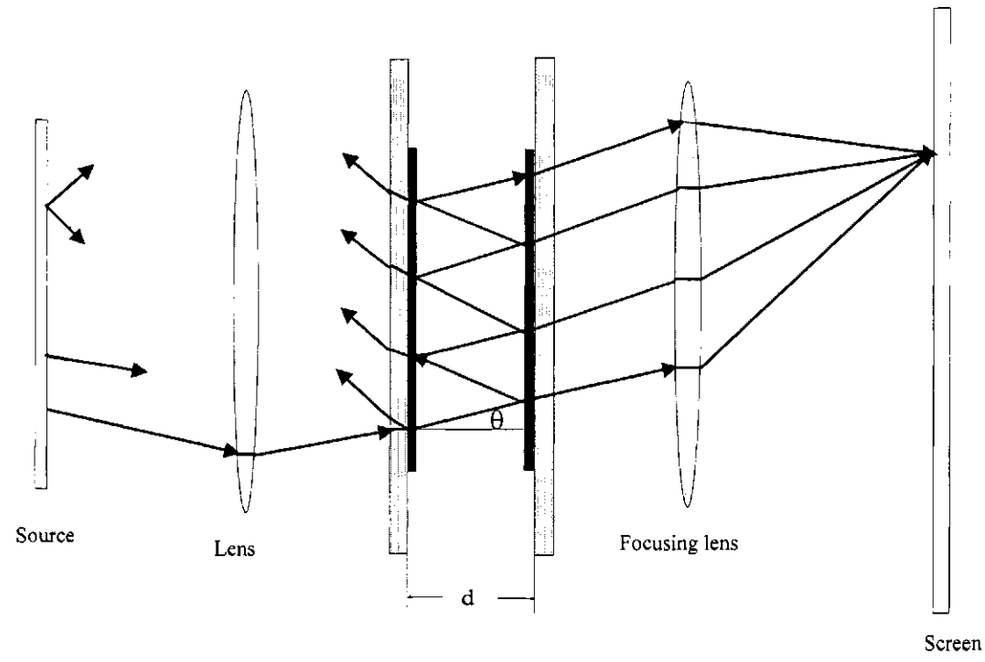

Figure 2.21: Fabry-Perot interferometer

Perot interferometer is given by equation [22]

$$\Re = \mathcal{F}m, \tag{2.43}$$

where $\mathcal{F}$ is known as the finesse defined as $\mathcal{F} = \frac{\pi\sqrt{F}}{2}$ and $F = 4R/(1-R)^2$. The challenge becomes to find highly reflective surfaces at submillimetre wavelengths, which will result in a high finess and thus high resolving power. Like a diffraction grating, the free spectral range of the Fabry-Perot interferometer is λ/m. While the grating spectrometer is usually operated in low order and has a relatively large free spectral range, it is common practice to operate a Fabry Perot interferometer in higher order ($m = 100 - 1000$), with a correspondingly lower free spectral range. While a Fabry-Perot interferometer has a higher throughput

than a grating spectrometer, its limited free spectral range and single wavelength operation make it unsuitable for measuring astronomical spectra at submillimetre wavelengths.

2.12 Conclusion

This chapter has introduced the mathematics behind the operation of a FTS. The advantages and disadvantages of the FTS, when compared with two other types of spectrometer that find common usage, have been explored. It has been shown that the FTS, with its simple optomechanical design, broad spectral coverage, high throughput and variable resolution make it a choice spectrometer for measurements of weak astronomical signals at submillimetre wavelengths. Moreover, as it will be seen in chapter 4, the FTS has the instrumental line shape of any spectrometer, and one which can be modified *post facto*. The principal disadvantage is the complexity of mathematics required to extract the spectrum.

Chapter 3

De-glitching

3.1 Overview

This chapter discusses the detection and removal of cosmic ray effects on the interferogram. After discussing some simple methods, a sophisticated new approach to the detection of cosmic rays, wavelet analysis, will be introduced.

3.2 Introduction to de-glitching

Cosmic rays are the nuclei of ordinary atoms stripped of their electrons. Their energies are extremely high and are distributed over a broad spectrum (from 10^9 eV to 10^{19} eV) [39]. The primary source of cosmic rays is the sun which provides the steady stream of protons and electrons [39, 40]. Under conditions of increased solar activity the solar cosmic ray flux can increase significantly as evidenced by increased auroral activity [41]. In addition, some high energy cosmic rays travel vast distances from deep space

although the exact nature of their origin is not well understood. Occasionally, a cosmic ray strikes the detector and imparts a large amount of energy which results in a characteristic spike in the interferogram. Approximately 1 in every 10 interferograms exhibit cosmic ray spikes [5]. As an example, figure 3.1 shows an interferogram of Uranus taken during the September 2002 observing run at the JCMT; figure 3.2 shows a zoomed in region of a cosmic ray event. The principle characteristic of a cosmic ray event is a sharp discontinuity in the interferogram followed by an exponential decay back to the mean level of the interferogram.

It is now common practice to use delta-sigma ($\Delta\Sigma$) analog-to-digital converters in scientific instrumentation. These devices offer up to 24-bit precision and include sophisticated digital filtering [42]. In the case of an interferogram, the $\Delta\Sigma$ effectively filters much of the exponential decay so the cosmic ray spike has only one or two points. Nonetheless, it is important to remove the cosmic ray from the interferogram before analysis, otherwise the sharp feature in the interferogram domain transforms to a sinusoidal noise component in the spectral domain. Even though the detector [43] is shielded by the aluminum casing of the dewar and large copper cold plates, the cosmic rays still get through these shield. Short of wrapping the detector into large amounts of lead, nothing can be done to stop the cosmic rays from occasionally reaching the detector.

Cosmic rays are often easy to detect visually because most of the time they stand out in the interferogram (figure 3.1). However, sometimes cosmic rays strike the detector near the position of zero path difference. When this happens, they are difficult to detect visually because here the interferogram has its greatest modulation. In principle, cosmic rays are easy to correct. The simplest method is to take the point immediately before the

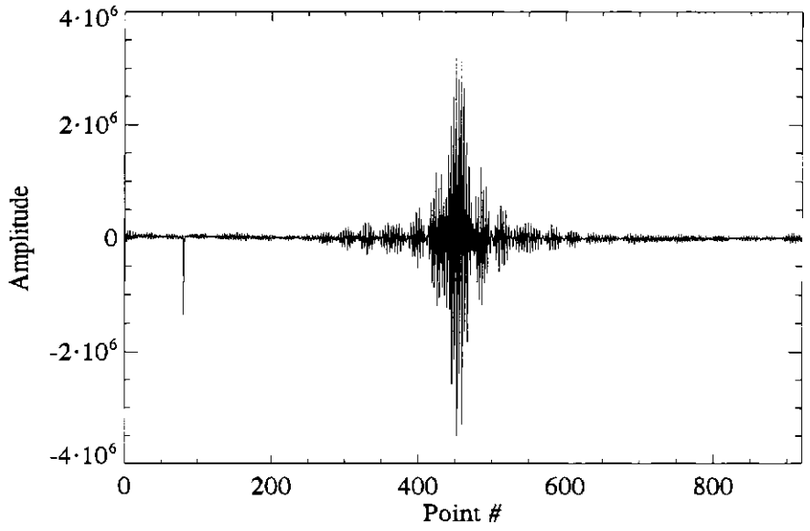

Figure 3.1: An example of the effect of a cosmic ray on the interferogram

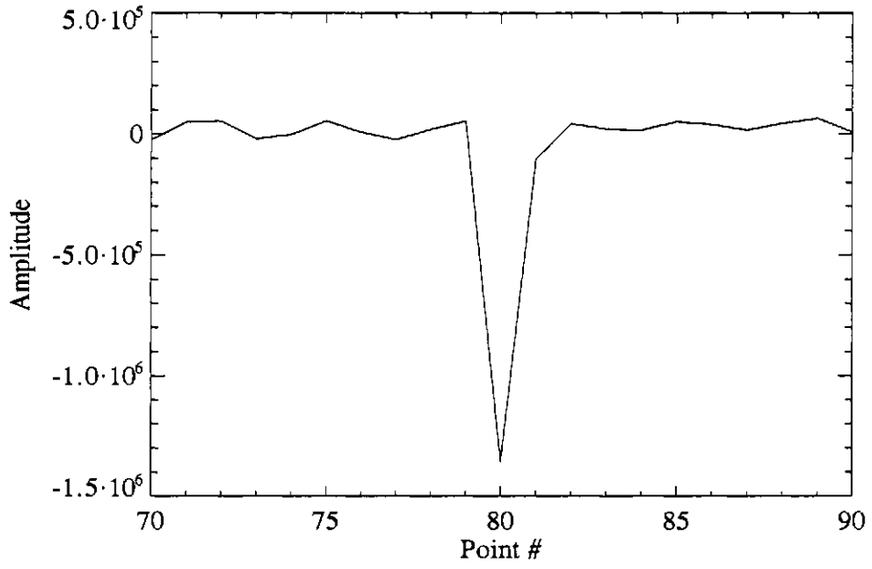

Figure 3.2: Zoomed-in region of the interferogram shown in figure 3.1.

cosmic ray event and one time later, when the interferogram has returned to its equilibrium position, and either substitute the mean value of the interferogram or linearly interpolate between the points.

3.3 Approach to de-glitching

As mentioned earlier, a data processing pipeline, written in Interactive Data Language (IDL®), has been developed for the analysis of data from the FTS [5]. In this pipeline, there is a step for removing cosmic rays. However, this step is not automated, so that de-glitching requires inspecting each interferogram by hand and removing the cosmic rays when necessary. This procedure can be time consuming, particularly when there are thousands of interferograms to inspect. Clearly, it would be more efficient to develop an automatic de-glitching process.

The initial approach taken was to look for deviations of the interferogram from its local mean value. Using a running window average of 10 points, the next point in the interferogram was compared with the window mean and variance, and if it differed by more than 3 standard deviations it was flagged as being a potential cosmic ray candidate. This would correctly pick out some cosmic ray events, but it also produced false positive detections, as shown in figure 3.3. This was particularly evident near the ZPD region where there naturally exist a high degree of modulation.

A second approach taken was to differentiate the interferogram and discriminate the cosmic rays on the steepness of the slope. However, for the reasons described above, this method also fails in the region of ZPD of the interferogram. While both these methods

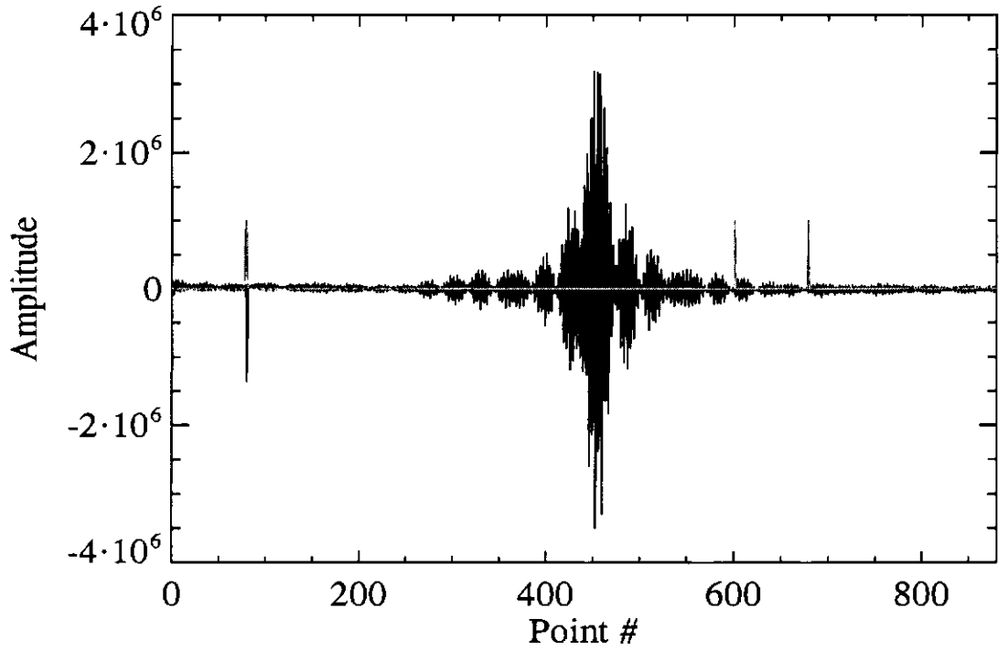

Figure 3.3: An interferogram with a cosmic ray: gray lines are an attempt to deglitch. This method picks out the cosmic ray and some of the beat patterns

work well far from the ZPD region and yet are incapable of detecting, all but the strongest, cosmic rays near the region of ZPD, another approach was required.

3.4 Wavelet analysis

It is possible to analyze a signal using an approach called multi-resolution analysis (MRA) [44]. MRA analyzes the signal at different frequencies with different spectral resolutions (ie., every spectral component is not resolved equally). MRA is designed to give good time resolution and poor frequency resolution at high frequencies and correspondingly, good frequency resolution and poor time resolution at low frequencies. This is equivalent

to observing a signal with low frequency components for long durations and a signal with high frequency components for short durations. Wavelet analysis is one powerful method of MRA [44]. In wavelet analysis, the signal is multiplied by a wavelet function, ψ. The width of the wavelet window is changed as the transform is computed for every single spectral component. The resulting continuous wavelet transform is defined as [44]:

$$CWT_x^{\psi}(\tau, s) = \Psi_x^{\psi}(\tau, s) = \frac{1}{\sqrt{|s|}} \int x(t)\psi^* \left(\frac{t-\tau}{s} \right) dt, \tag{3.1}$$

where the transformed signal is a function of two parameters, τ and s. τ is the translation parameter and s is the scale parameter. $\psi(t)$ is the transforming function and it is called the mother wavelet. The term translation corresponds to the location of the window and the scale corresponds to the inverse of the frequency.

The computation of CWT

The interferogram, $x(t)$, is the signal to be transformed. The mother wavelet is chosen to serve as a prototype for all window functions in the process. All the windows that are used are scaled (ie., dilated (or compressed)) and shifted versions of the mother wavelet. There are a wide variety of mother wavelets in common use (Daubechies, Mallet, Morlet etc.) [45, 46]. Once the wavelet function is chosen, the computation starts with a scaling of unity, $s = 1$. The wavelet transform is computed for all values of s, smaller and larger than 1. As one increases the scaling factor, the wavelet becomes compressed as one effectively studies lower spatial frequencies. For a given scale value, the wavelet is then convolved with the interferogram signal. The factor $\frac{1}{\sqrt{|s|}}$ is required to normalize the integral in equation 3.1. The convolution is repeated for increasing values of s to produce

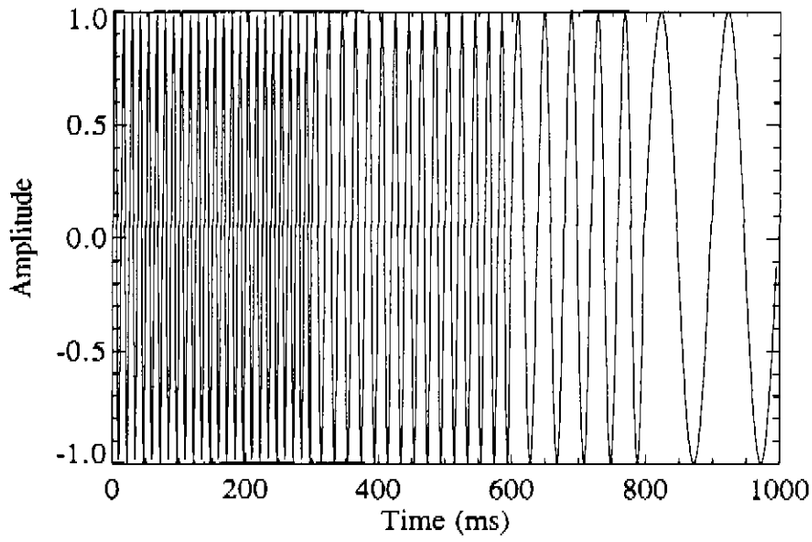

Figure 3.4: A time dependent signal consisting of 4 different frequencies: between 0 and 300 ms the frequency is 80 Hz, between 300 and 600 ms, 50 Hz, between 600 and 800 ms, 25 Hz and between 800 and 1000, 10 Hz.

the continuous wavelet transform (CWT).

By way of illustration, figure 3.4 shows a non-stationary signal consisting of four different frequencies at four different times: between 0 to 300 ms the frequency of the signal is 80 Hz, between 300 and 600 ms the frequency is 50 Hz, between 600 and 800 ms the frequency is 25 Hz and between 800 and 1000 ms the frequency is 10 Hz.

The wavelet transform of this signal is shown in figure 3.5 where the axes are time, scale and intensity. By comparison with figure 3.4 it can be seen that smaller scales correspond to higher frequencies. As mentioned earlier, the wavelet transform has a good time resolution and poor frequency resolution at high frequencies, while it has poor time resolution and good frequency resolution at low frequencies. This can be seen in the figure 3.5. At small scales (in the range from 16 to 64 - corresponding to the 80 Hz feature in

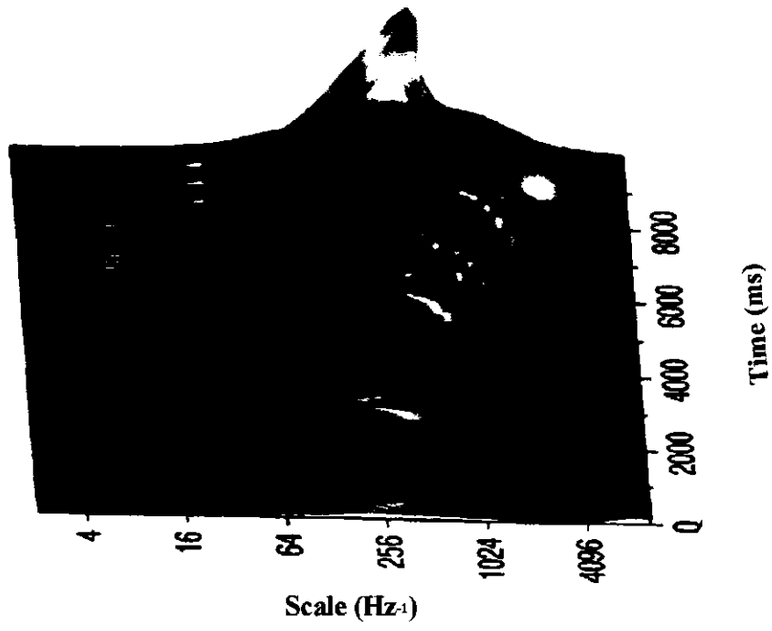

Figure 3.5: A wavelet transform of the non-stationary signal shown in figure 3.4

figure 3.4), the scale resolution is good; however, since the scale is inversely proportional to frequency, this is equivalent to poor frequency resolution. The corresponding time resolution of this 80 Hz signal, as evidenced by the sharpness of this feature projected on to the time axis, is good. By comparison, at large scales (in the range from 100 to 600 - corresponding to the 10 Hz feature in figure 3.4), the scale resolution is poor, and correspondingly, the frequency resolution is good. However, as expected, the time resolution is poor as evidenced by the ill-defined projection of this feature on to the time axis.

3.5 IDL® wavelet analysis toolkit

The IDL® wavelet analysis toolkit package comes with seven wavelet functions: Daubechies, Haar, Coiflet, Symlet, Morlet, Paul and Gaussian [47]. All wavelet functions were applied to the interferogram shown in figure 3.6 to determine their efficiency in detecting cosmic rays. This study has shown that the Gaussian wavelet function appears to give the best results. Figure 3.6 shows the result of applying a Gaussian wavelet function to the interferogram of figure 3.1, repeated here for convenience.

In this figure, the x-axis corresponds to the interferogram position and the y-axis corresponds to the scale. It can be clearly seen that the cosmic ray feature is immediately evident having a significant intensity over a wide range of scales. More importantly, the scale range of the interferogram, even in the heavily modulated ZPD region is very low, which suggests that wavelet analysis will be a powerful tool for detecting cosmic rays in this region, also. As chance would have it, application of this technique to the search and detection of the cosmic rays in the ZPD region of the interferograms that form the basis of my thesis did not reveal any likely candidates.

For completeness, figures 3.7 to 3.12 show wavelet transforms of the same interferogram performed with six different mother wavelets, which are distributed with the IDL® toolkit. The toolkit for the wavelet application is in read-only format, so for more information on the details of the wavelets, the reader is referred to the toolkit manual [47]. It can be seen that the plotting ranges of the figures are different from one another. This is a result of the automatic scaling of the read-only software that was distributed with the toolkit. The cosmic ray is identified by all wavelets, but most importantly, there is a

variation in the scale range in the ZPD region from one wavelet to another. The cosmic ray is more evident with the application of a Gaussian wavelet. Moreover, the scale range near ZPD is narrow with the application of the Gaussian wavelet. This is not surprising, because the spectral passband of the detector, which is defined by a narrow band filter, has an approximately Gaussian profile. Features in the interferogram that correspond to non-physical interferometric signals will have spectral components that fall outside of this bandpass and therefore require different scales of the Gaussian wavelet. By contrast, features that are due to interferometric signals will be well represented by a Gaussian wavelet of fixed scale. In this brief analysis of the applicability of wavelets to the detection of cosmic rays, it has been shown that the technique holds potential for detecting cosmic rays and that in the present case, the Gaussian wavelet proves the best results.

3.6 Conclusion

It is important to remove the effects of the cosmic rays from the interferogram. While simple methods based on differences or statistics of the interferogram can be employed, they fail near the ZPD region where the interferogram experiences its greatest modulation. A new sophisticated method, based on wavelet analysis, holds much promise for the detection of cosmic ray events even near the heavily modulated ZPD region.

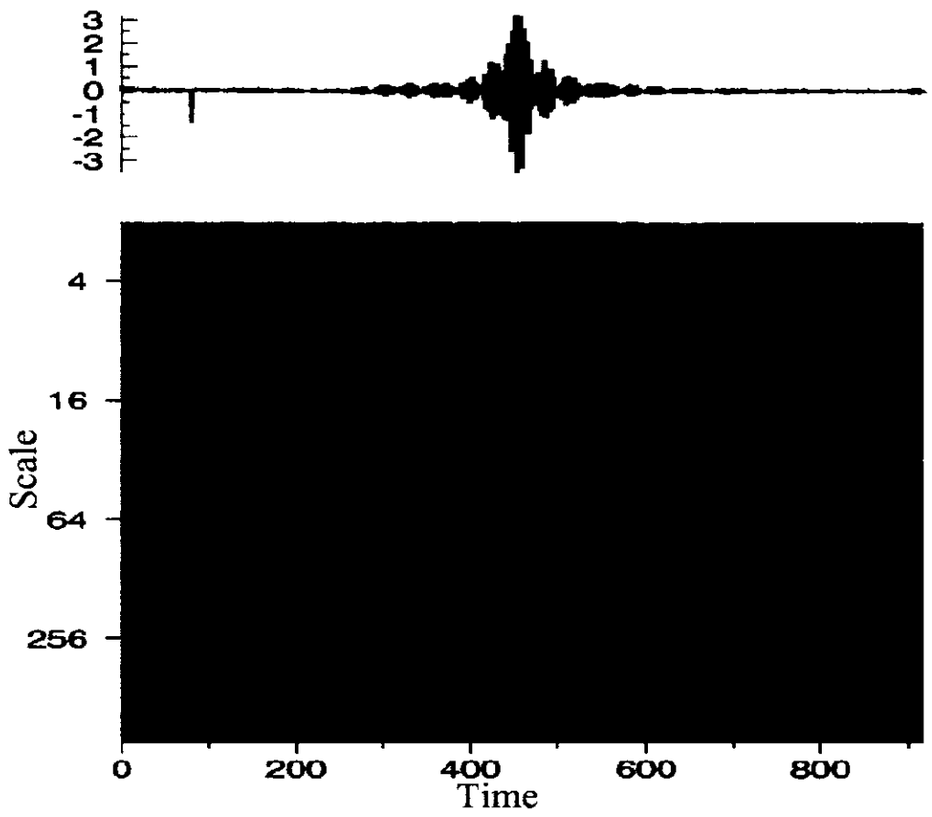

Figure 3.6: Wavelet transform of the interferogram shown in figure 3.1. The cosmic ray at 80 ms shows a wide range of scale in the wavelet transform. By comparion, the heavily modulated zero path difference region of the interferograms shows a low and limited range of scales in the wavelet transform.

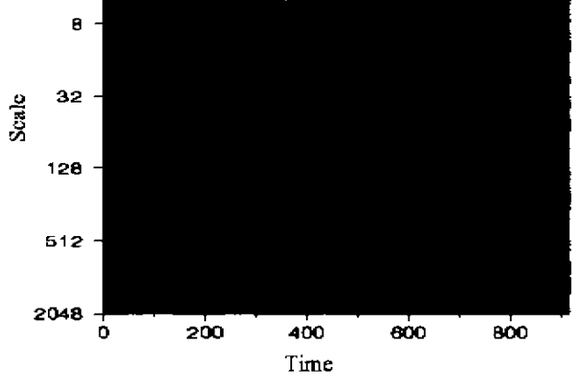

Figure 3.7: Daubechies wavelet

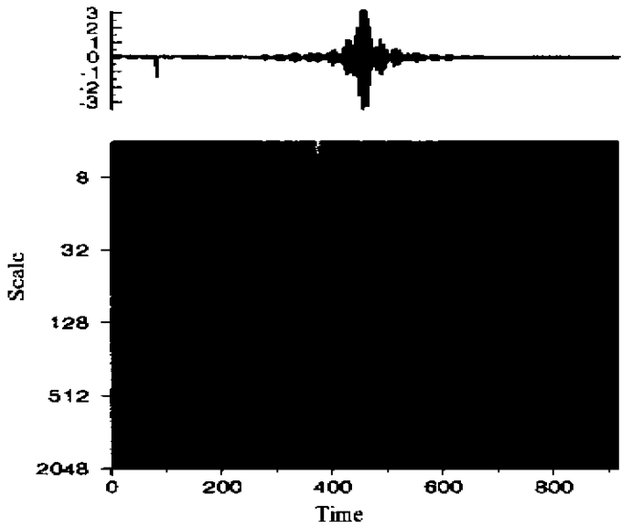

Figure 3.8: Coiflet wavelet

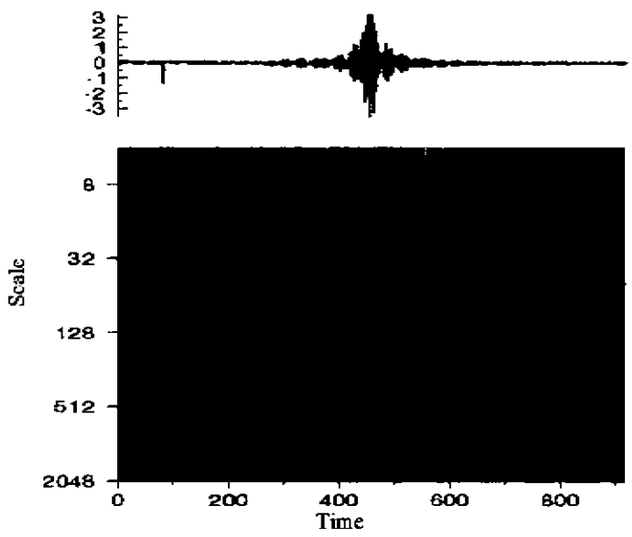

Figure 3.9: Haar wavelet

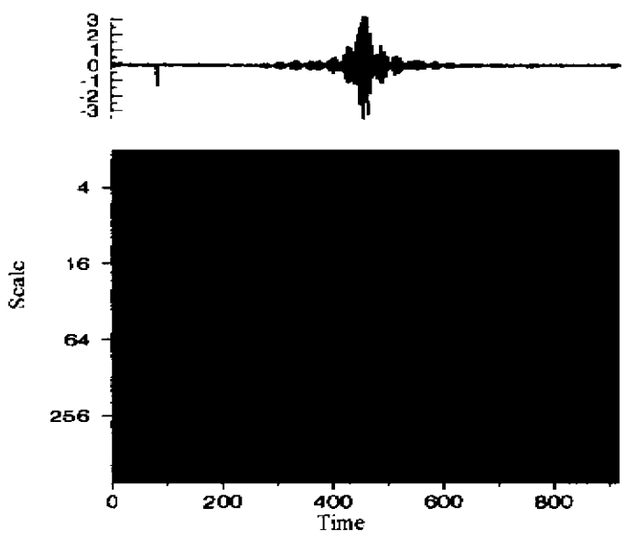

Figure 3.10: Morlet wavelet

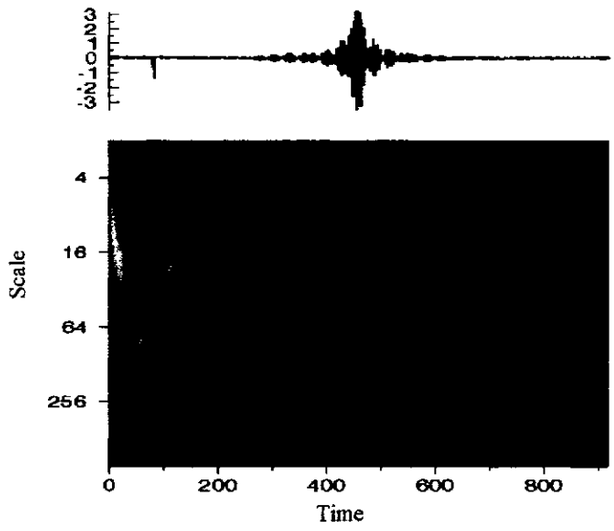

Figure 3.11: Paul wavelet

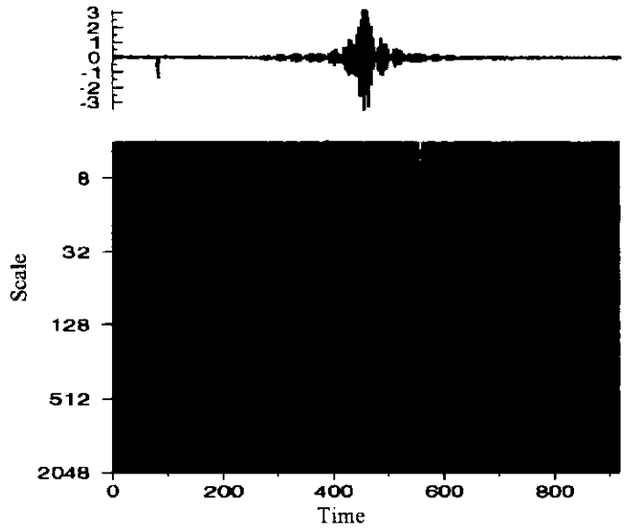

Figure 3.12: Symlet wavelet

Chapter 4

Apodization

4.1 Overview

This chapter discusses apodization, an important topic in the field of FTS spectroscopy. Following a brief overview of apodization and in particular the role of natural apodization that occurs in any interferometer, the rest of the chapter will focus on the derivation of optimum apodization functions for FTS spectroscopy.

4.2 Introduction to apodization

Apodization [4, 25, 48, 49, 50, 51, 52] is a mathematical procedure that is used in FTS spectroscopy to minimize the "ringing" present in the Instrumental Line Shapes (ILS). The word apodization refers to the suppression of the ringing, or the side lobes of the ILS; the word is derived from the Greek, 'α $\pi\grave{o}\delta os$, which means 'without feet' [25]. The ringing is the result of the interferogram being truncated at finite optical path differences.

The Fourier transform of an interferogram produced by a monochromatic source from an ideal interferometer, measured out to infinite optical path difference, would yield a delta function. Mathematically, the interferogram measured out to an infinite distance can be expressed by the following equation which was derived in chapter 2 [25]:

$$I(\delta) = \int_{-\infty}^{+\infty} B(\sigma) \cos 2\pi\sigma\delta \cdot d\sigma. \tag{4.1}$$

Here, $I(\delta)$ represents the interferogram, $B(\sigma)$ is the intensity of the source at wavenumber σ (cm^{-1}) and δ is the optical path difference variable (cm). The spectrum is calculated by taking the cosine Fourier transform of $I(\delta)$

$$B(\sigma) = \int_{-\infty}^{+\infty} I(\delta) \cos 2\pi\sigma\delta \cdot d\delta. \tag{4.2}$$

Since in practice, interferograms have finite length this is equivalent to an infinitely long interferogram shown in figure 4.1 multiplied by a top hat function shown in figure 4.2 and represented by the equation

$$\begin{aligned} \Pi(\delta) &= 1 \quad |\delta| \leq L \\ \Pi(\delta) &= 0 \quad |\delta| > L. \end{aligned} \tag{4.3}$$

The resultant wave is a cosine wave with a sharp cut off at the optical path difference ±L shown in figure 4.3. The Fourier transform of equation 4.3 is

$$\mathcal{F}\{\Pi(\delta)\} = \int_{-L}^{L} e^{-i2\pi\sigma\delta} d\delta = 2L\mathrm{sinc}(2\pi\sigma L), \tag{4.4}$$

which is shown in figure 4.4 where the sinc function is defined as

$$\mathrm{sinc}(2\pi\sigma\delta) = \frac{\sin(2\pi\sigma\delta)}{2\pi\sigma\delta}. \tag{4.5}$$

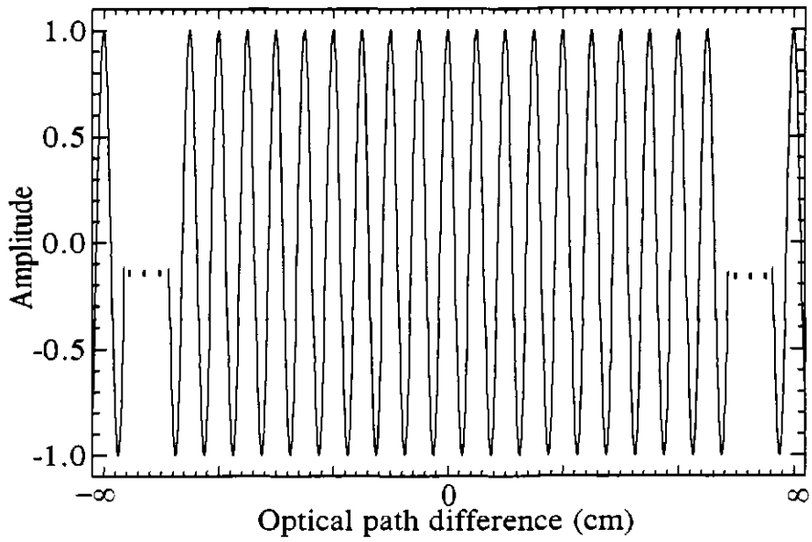

Figure 4.1: Infinite cosine wave of frequency σ_0

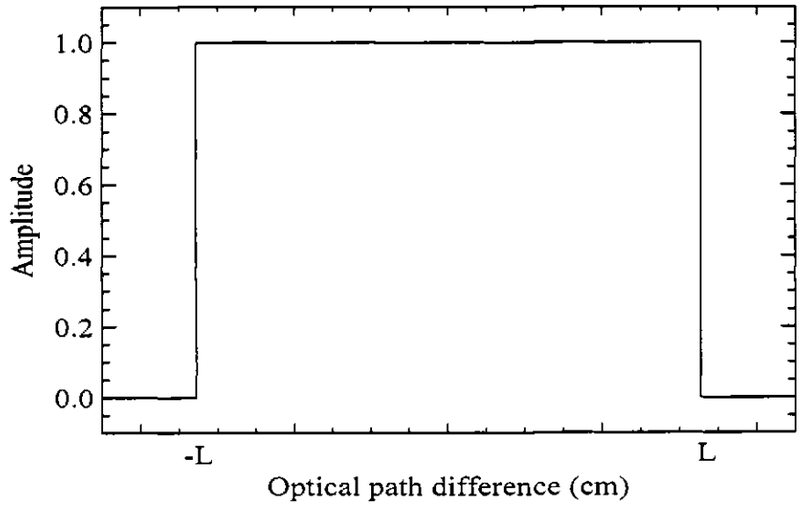

Figure 4.2: Top hat function with a maximum optical path difference of $\pm L$.

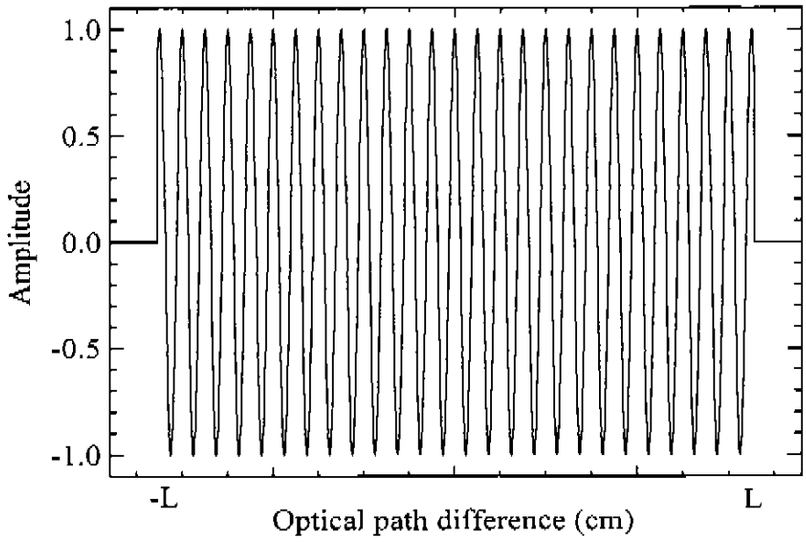

Figure 4.3: A truncated interferogram of a monochromatic source of frequency σ_0

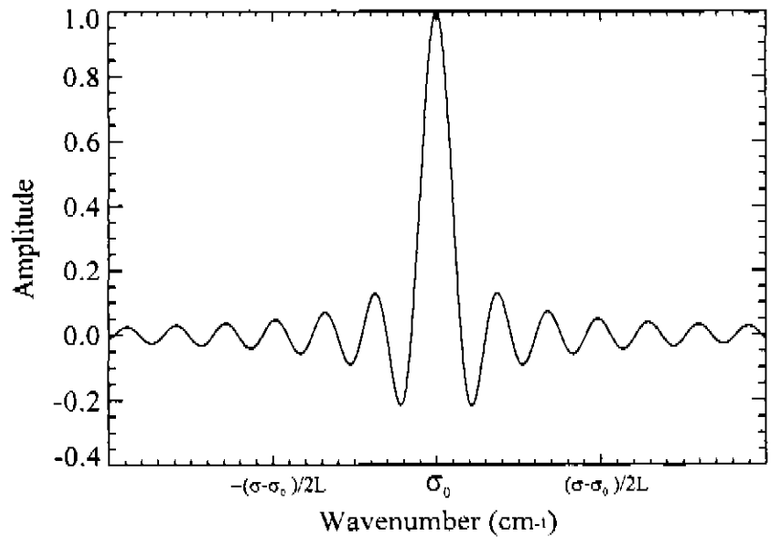

Figure 4.4: Fourier transform of the interferogram in figure 4.3

Since the interferograms can only be measured to finite optical path differences, the Fourier transform of an interferogram is equivalent to the convolution of the spectrum with equation 4.4 meaning that all spectral lines will have a sinc profile. In the case where one is primarily interested in the continuum component of emission, it is useful to reduce the size of the sidelobes of the sinc function by use of an apodizing function.

The convolution of two functions $g(t)$ and $h(t)$ is defined in the following equation [38]:

$$g(t) * h(t) = \int_{-\infty}^{+\infty} g(u)h(t-u)du. \tag{4.6}$$

Convolution of two functions can be thought of as the area of the product of $g(u)$ and $h(t-u)$, varying with t [38]. In another words, a convolution is an integral that expresses the amount of overlap of one function h as it is shifted over another function g. If $H(f) = \mathcal{F}^{-1}\{h(t)\}$ and $G(f) = \mathcal{F}^{-1}\{g(t)\}$ then the convolution theorem can be described through the following equations [38]:

$$\begin{aligned} \mathcal{F}\{H(f)G(f)\} &= \mathcal{F}\{H(f)\} * \mathcal{F}\{G(f)\} = h(t) * g(t) \\ \mathcal{F}^{-1}\{h(t) * g(t)\} &= \mathcal{F}^{-1}\{h(t)\}\mathcal{F}^{-1}\{g(t)\} = H(f)G(f), \end{aligned} \tag{4.7}$$

and

$$\begin{aligned} \mathcal{F}^{-1}\{h(t)g(t)\} &= H(f) * G(f) \\ \mathcal{F}\{H(f) * G(f)\} &= h(t)g(t). \end{aligned} \tag{4.8}$$

This illustrates that multiplication in the time domain is equivalent to the convolution in the frequency domain, and vice versa [4]

Function	FWHM	h_1	h_2	h_3	h_4	h_5
Sinc	$\frac{1.207}{2L}$	-0.21723	-0.09132	-0.05797	-0.04248	-0.03352
		0.71552	1.73632	2.74215	3.74511	4.74704

Table 4.1: FWHM, height (upper) and position (lower) in units of 1/L of the first 5 secondary minima of a sinc function (figure 4.4) normalized to the principal maximum.

Function	FWHM	h_1	h_2	h_3	h_4	h_5
Sinc	$\frac{1.207}{2L}$	0.12837	0.07091	0.04903	0.03747	0.03033
		1.23015	2.23983	3.24382	4.24616	5.24780

Table 4.2: FWHM, height (upper) and position (lower) in units of 1/L of the first 5 secondary maxima of a sinc function (figure 4.4) normalized to the principal maximum.

Three parameters are important when discussing apodization: the height of the principal maximum, the FWHM, and the height of the largest secondary maximum of the ILS. Tables 4.1 and 4.2 show the FWHM and the height of the of the secondary maxima and minima of a sinc function; secondary heights being normalized with respect to the principal maximum.

From table 4.1, we can see that the first minimum is about -21.7 % which is a significant fraction of the total height of the sinc function. It is also noticeable that the heights of successive secondary maxima fall off, but not very rapidly. The ILS of a perfect interferogram obtained with an interferometer sampled out to optical path difference $\pm L$ is the sinc function, given by equation 4.5, which is responsible for the ringing seen in the spectral lines.

The sole purpose of apodization is to decrease the amplitude of the secondary lobes of the sinc function in the frequency domain at the cost of increasing the FWHM, or equivalently, lowering the spectral resolution. Apodization is accomplished by multiplying the interferogram with a function which generally reduces the amplitude of the interferogram

at increased optical path differences and results in the broadening of the ILS (recall that the ILS is simply the Fourier transform of the apodizing function). Many apodization functions find common use, but only a few of them are recommended [51]. A good apodizing function will decrease the amplitude of the sidelobes while minimizing the increase in the FWHM. The shape of the ILS is determined by the shape of the Fourier transform of the apodizing function. As an example, let us look at the following function

$$\begin{aligned} A(\delta) &= 1 - \left|\frac{\delta}{L}\right| \qquad -L \leq \delta \leq L \\ A(\delta) &= 0 \qquad\qquad\quad \delta > |-L|. \end{aligned} \tag{4.9}$$

This is the so called triangular, or Bartlett, apodization function; it is the most commonly used apodization function in infrared FTS spectroscopy [25] yet, as it will be shown later, and far from optimum. In general, any function that has a value of unity at $\delta = 0$ and decreases with increasing retardation can be used as an apodizing function.

4.3 Natural apodization

In reality, all interferograms suffer from some degree of apodization due to the divergence of radiation within the interferometer. In the case of a point source located at a focus of a lens which feeds an interferometer, the resulting collimated beam has no divergence and thus the overlap of the recombined beams from the interferometer is independent of path difference. In a real interferometer the entrance aperture has finite size which means that a beam entering the interferometer is divergent and the overlap between the recombined beam now depends upon the path difference between them; this leads to the phenomenon known as natural apodization. For example, consider the light entering

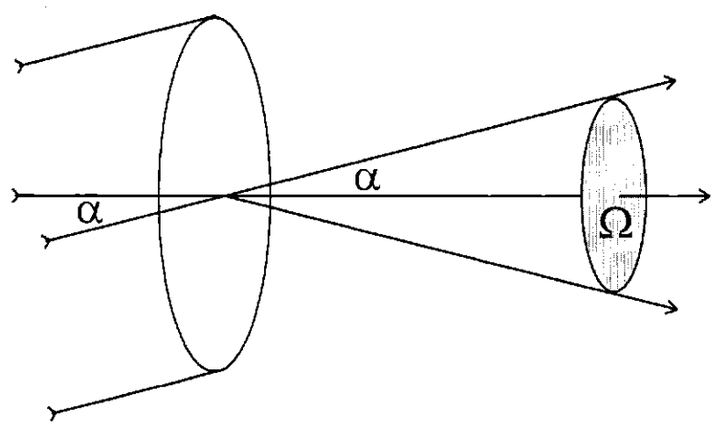

Figure 4.5: A diagram of light entering the entrance aperture at an angle α.

an entrance aperture at an angle α shown in figure 4.5. Then the off-axis path difference is $\delta\cos(\alpha)$. The resulting intensity is evaluated by integrating over the solid angle Ω using

$$dI(\delta) = \cos(2\pi\sigma\delta\cos(\alpha))d\Omega. \tag{4.10}$$

In the small angle approximation $\cos(\alpha) \approx 1 - \frac{\alpha^2}{2}$, equation 4.10 becomes

$$dI(\delta) = \cos\left(2\pi\sigma\delta\left(1 - \frac{\alpha^2}{2}\right)\right)d\Omega. \tag{4.11}$$

For a circular entrance aperture $\Omega = \pi\alpha^2$. Substituting this into equation 4.11 and integrating from $\Omega = 0$ to $\Omega = \Omega_m$, where Ω_m is the divergence limit within the interferometer, we obtain the following equation for the interferogram

$$I(\delta) = \Omega_m \text{sinc}\left(\frac{\sigma\delta\Omega_m}{2\pi}\right)\cos\left(2\pi\sigma\delta\left(1 - \frac{\Omega_m}{4\pi}\right)\right) \tag{4.12}$$

The sinc term in equation 4.12 is what gives rise to the natural apodization discussed above, while the $\frac{\Omega_m}{4\pi}$ term inside the cosine function is due to the off-axis optical path difference variation which causes the oblique rays to be observed at shorter wavenumbers. Natural apodization is a direct result of the finite entrance aperture.

4.4 The Filler diagram

Many studies have been conducted on apodization functions. In 1964, A.S. Filler [52] conducted a study of several apodization functions and introduced two families of functions denoted by $D_\alpha(\delta)$ and $E_\alpha(\delta)$ defined as

$$D_\alpha(\delta) = \cos\left(\frac{\pi\delta}{2L}\right) + \alpha\cos\left(\frac{3\pi\delta}{2L}\right) \qquad \text{where} \quad 0 \leq \alpha \leq 1 \tag{4.13}$$

$$E_\alpha(\delta) = 1 + (1+\alpha)\cos\left(\frac{\pi\delta}{L}\right) + \alpha\cos\left(\frac{2\pi\delta}{L}\right) \qquad \text{where} \quad 0 \leq \alpha \leq 1. \tag{4.14}$$

Filler devised a way of comparing different functions by plotting the normalized height of the largest secondary maximum as a function of FWHM. The FWHM of the central peak of the apodization function is a measure of resolution, and the absolute magnitude of the first sidelobe is a measure of apodization [52]. It is important to note that in some cases the first lobe is not the largest one. Therefore, Filler generalized the measure of apodization to be the magnitude of the lobe with the largest absolute value. He discovered that the logarithm of the absolute value of the first lobe varies almost linearly with the FWHM of the central peak for the two cases of $D_\alpha(\delta)$ and $E_\alpha(\delta)$ functions, where α lies between 0 and 0.25.

In 1975, Robert H. Norton and Reinhard Beer [51] introduced another set of functions, denoted $P_{\alpha,p}(\delta)$, which are variants of the $E_\alpha(\delta)$ family. They added a constant

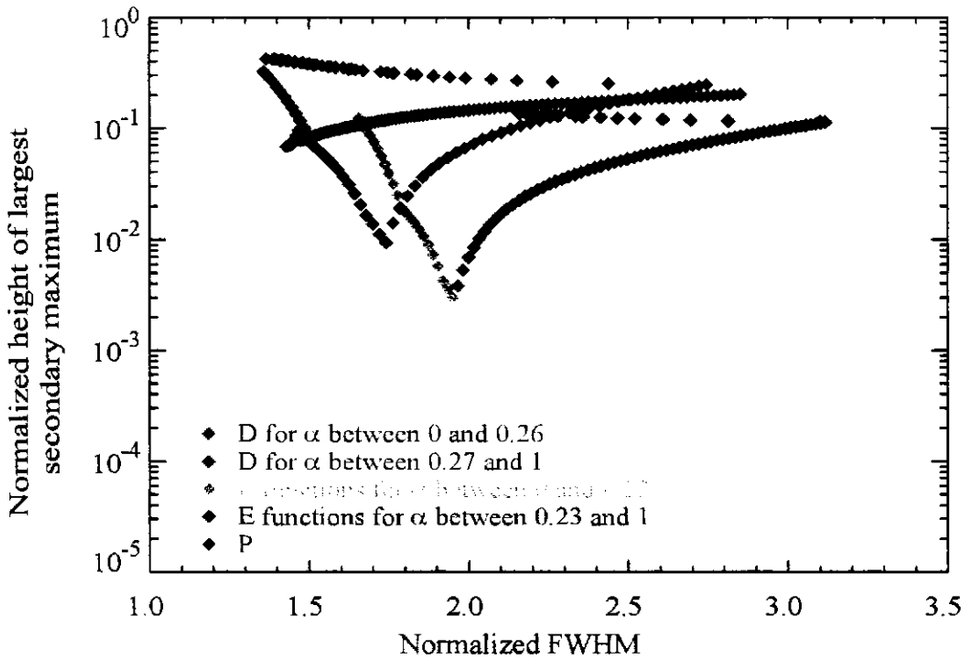

Figure 4.6: Filler diagram for $D_\alpha(\delta), E_\alpha(\delta)$ and $P_{\alpha,p}(\delta)$ functions. Red and orange portions of the graph are somewhat linear as proposed by Filler

term p and allowed α to vary from -1 to 1. $P_{\alpha,p}(\delta)$ are described by the following equation:

$$P_{\alpha,p}(\delta) = 1 + p + (1+\alpha)\cos\left(\frac{\pi\delta}{L}\right) + \alpha\cos\left(\frac{2\pi\delta}{L}\right) \quad \text{where} \quad -1 \leq \alpha \leq 1 \quad 0 \leq p \leq 1. \tag{4.15}$$

Figure 4.6 shows the three families of functions $D_\alpha(\delta), E_\alpha(\delta)$ and $P_{\alpha,p}(\delta)$ graphed on what is known as the Filler diagram. Different points on the graph are functions with different values of α. The portions that are in red are the values of α from 0 to 0.26 for functions $D_\alpha(\delta)$. The portions in orange are the values of α from 0 to 0.22 for functions $E_\alpha(\delta)$. For these values of α the graph looks linear for both sets of functions.

4.4.1 Norton-Beer apodization functions

Robert H. Norton and Reinhard Beer [51, 50] conducted a study of about three thousand algebraic and trigonometric-algebraic functions. These authors computed the FWHM and height of the largest secondary lobe of these functions, and plotted them on the Filler diagram.

The authors found that the best set of apodizing functions is simply algebraic of the form

$$A(\delta) = \sum_{i=0}^{n} C_i \left[1 - \left(\frac{\delta}{L}\right)^2\right]^i \text{ where } \sum_{i=0}^{n} C_i \equiv 1. \tag{4.16}$$

In these functions, n does not exceed four since the authors did not find any improvement beyond this value. As a result of this analysis the authors identified three functions, out of the three thousand, that are optimum and now find common usage in Fourier spectroscopy. These are known as Norton-Beer 'weak', 'medium' and 'strong' apodization functions. These apodization functions and their corresponding ILSs are shown in figures 4.7 and 4.8, respectively. Table 4.3 shows the coefficients, C_i , of these functions [51]. It also shows the resulting FWHM and the height of the largest secondary lobe of the corresponding ILSs normalized to the case of the sinc function. It can be seen from figure 4.7 that these functions fall off sharply with increased path difference, but they do flatten out and some even increase slightly. The ILSs of these three functions are shown in figure 4.8 As expected, it can be seen that weak Norton-Beer apodization has larger sidelobes compared with the medium and strong apodization. The price of reducing the amplitude of ringing results in the lowering of the spectral resolution. The Norton-Beer functions have the advantage in that the zero crossings of each function essentially coincide with the

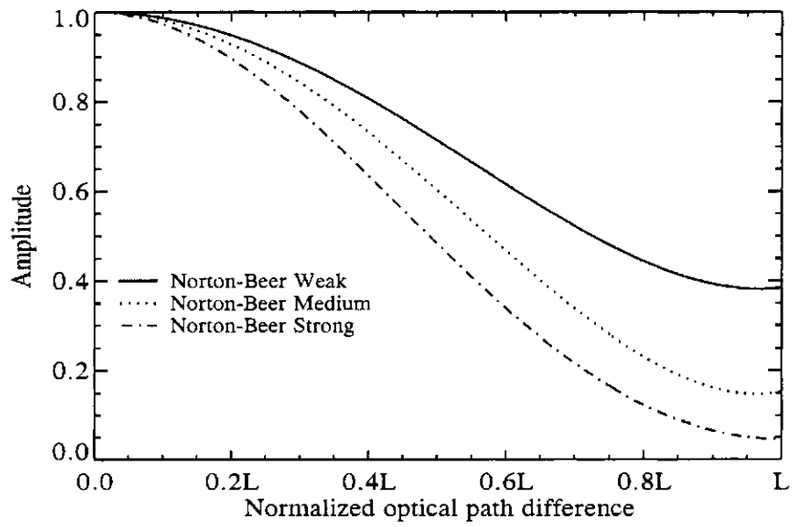

Figure 4.7: Norton-Beer weak, medium and strong apodizing functions

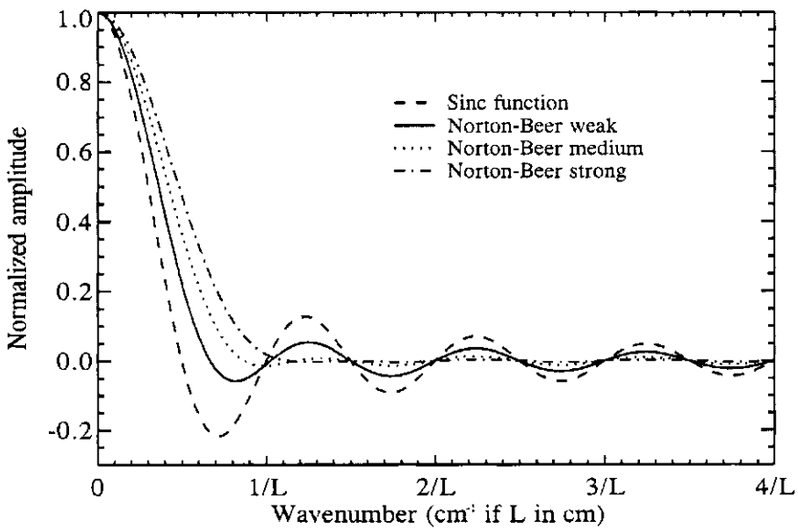

Figure 4.8: Instrumental line shapes for Norton-Beer weak, medium and strong apodizing functions as a function of maximum optical path difference, L

Apodizing function number	C_0	C_1	C_2	C_4	Normalized FWHM	Height of largest secondary lobe
0 (Boxcar)	1	0	0	0	1.000	-21.723 %
1 (Weak)	0.384093	-0.087577	0.703484	0	1.200	-5.816 %
2 (Medium)	0.152442	-0.136176	0.983734	0	1.400	-1.426 %
3 (Strong)	0.045335	0	0.554883	0.39978	1.600	-0.373 %

Table 4.3: Coefficients of the Norton-Beer apodizing functions.

zero crossings of the sinc function. The more closely the crossings are to those of the sinc function, the less damage is done to the independence of the data [51].

It is interesting to note that on the Filler diagram there appears to be a boundary below which no function penetrates. Norton-Beer determined the empirical equation of this boundary to be [51]

$$\log_{10}|h/h_0| \approx 1.939 - 1.401\,(W/W_0) - 0.597\,(W/W_0)^2\,. \tag{4.17}$$

In this equation h/h_0 is the size of the largest secondary lobe (not necessarily the first one) relative to the sinc function and W/W_0 is the FWHM relative to the sinc function. For the purpose of graphing the functions on the Filler diagram, the FWHM and the height of the secondary lobe of each function is divided by the corresponding value of the sinc function. The locus of some apodizing functions are shown in figure 4.9 and some of the functions in this figure are given in equation 4.18 [49]: It is evident that almost all of the functions lie to the right of the empirically determined boundary. The three Norton-Beer functions, with coefficients given in table 4.3, were chosen so that the ILSs would fall very close to the boundary, as it can be seen from figure 4.9. From the Filler diagram, we can see that there is one function for each family of functions $D_\alpha(\delta)$, $E_\alpha(\delta)$ and $P_{\alpha,p}(\delta)$ that falls very

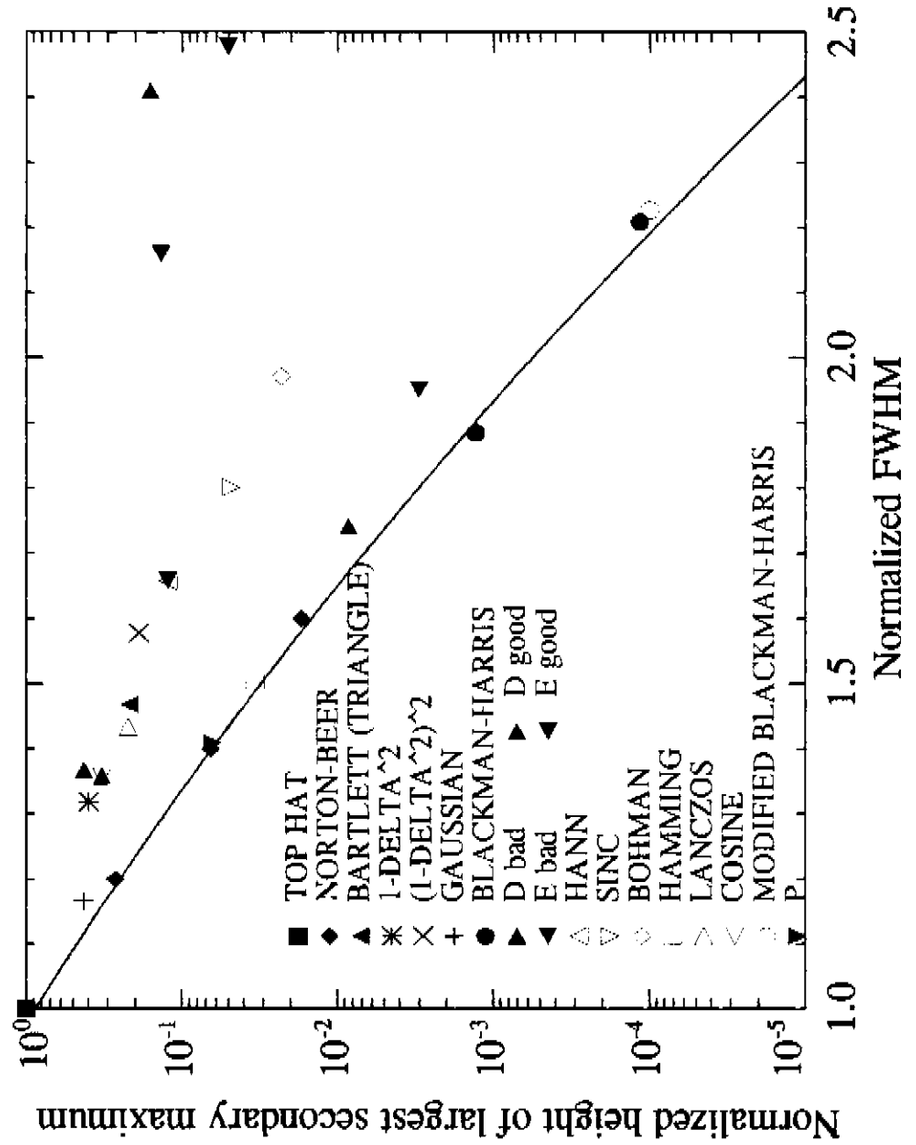

Figure 4.9: Filler diagram for the instrumental line shapes of apodizing functions discussed in the text. The solid line is the empirical boundary defined by equation 4.17

close to the line. The values of α for these functions are: $\alpha = 0.26$ for D_α , $\alpha = 0.22$ for E_α, $p = 0.3$ and $\alpha = -0.0325$ for $P_{\alpha,p}$.

$$\begin{aligned} Bartlett &= 1 - \frac{\delta}{L} \\ Gaussian &= \exp\left(-\left(\frac{\delta}{L}\right)^2\right) \\ Hann &= 0.5(1 + \cos\left(\pi\frac{\delta}{L}\right) \\ Bohman &= \left(1 - \frac{\delta}{L}\right)\cos\left(\pi\frac{\delta}{L}\right) + \frac{1}{\pi}\sin\left(\pi\frac{\delta}{L}\right) \\ Lanczos &= \sin\left(\frac{\pi\delta}{L}\right) / \left(\frac{\pi\delta}{L}\right). \end{aligned} \tag{4.18}$$

4.4.2 Blackmann-Harris and Hamming apodization functions

From the Filler diagram we can see that other functions lie close to the boundary: Hamming and Blackman-Harris (B-H). The Hamming function is given by [49]

$$A(\delta) = 0.54 + 0.46\cos\left(\frac{\pi\delta}{L}\right). \tag{4.19}$$

There are two common versions of Blackman-Harris functions [49]; the three term Blackmann-Harris function is given by

$$A(\delta) = 0.42323 + 0.49755\cos\left(\frac{\pi\delta}{L}\right) + 0.07922\cos\left(\frac{2\pi\delta}{L}\right), \tag{4.20}$$

and the four terms Blackman-Harris function is given by

$$A(\delta) = 0.35875 + 0.48829\cos\left(\frac{\pi\delta}{L}\right) + 0.14128\cos\left(\frac{2\pi\delta}{L}\right) + 0.01168\cos\left(\frac{3\pi\delta}{L}\right). \tag{4.21}$$

Recently, Learner et al. [31] introduced a modified four term Blackmann-Harris function which takes the form

$$A(\delta) = 0.355766 + 0.487395\cos\left(\frac{\pi\delta}{L}\right) + 0.144234\cos\left(\frac{2\pi\delta}{L}\right) + 0.012605\cos\left(\frac{3\pi\delta}{L}\right), \quad (4.22)$$

in which the coefficients are modified to remove the pedestal at the end of the apodizing function. All four of these functions are shown in figure 4.10 and the ILSs are shown in figure 4.11.

As can be seen from figure 4.9 the locus of these functions on the Filler diagram falls close to the boundary which is defined by the empirical line given by equation 4.17. The goal is to find functions that lie close to this boundary; functions that are far from this boundary are less than optimum and should be avoided. It can be seen that one of the worst functions in this respect is the triangle function. The FWHM of triangle function is 1.48 with respect to the sinc function and height of the secondary lobe is 4.7 % of the central maximum. The Hamming function has a similar FWHM but its height of the secondary lobe is 0.735 % of the central maximum, which is considerably smaller. Surprisingly the triangle function is still widely used in Fourier transform spectroscopy.

4.5 Extended apodizing functions

We have extended the work of Norton and Beer to generate 10 apodizing functions of the family described by equation 4.16, which correspond to FWHMs of the ILS from 1.1 to 2.0 in steps of 0.1. Seven of these functions are new; three functions that correspond to FWHMs of 1.2, 1.4 and 1.6 represent minor changes to those given earlier. These functions were generated by finding the best set of coefficients C_i in equation 4.16 for each FWHM.

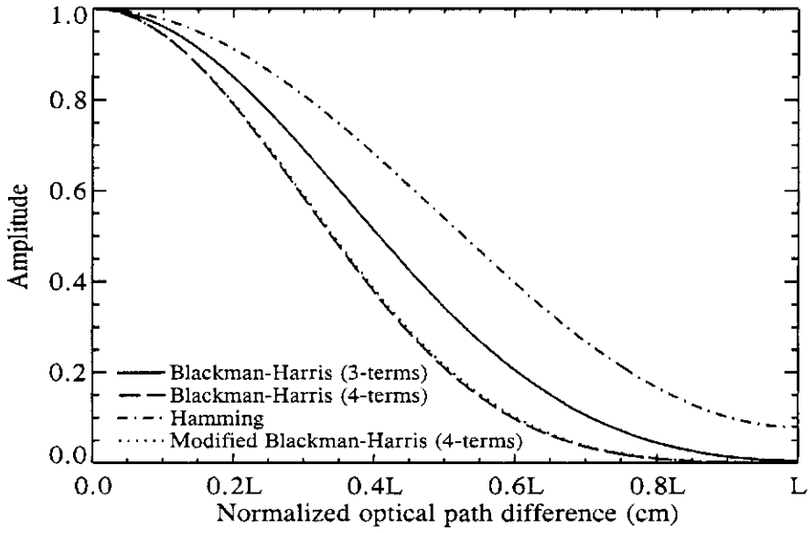

Figure 4.10: Four apodizing functions: Blackman-Harris (3-terms), Blackman-Harris (4-terms), Hamming and adjusted Blackman-Harris (4-terms)

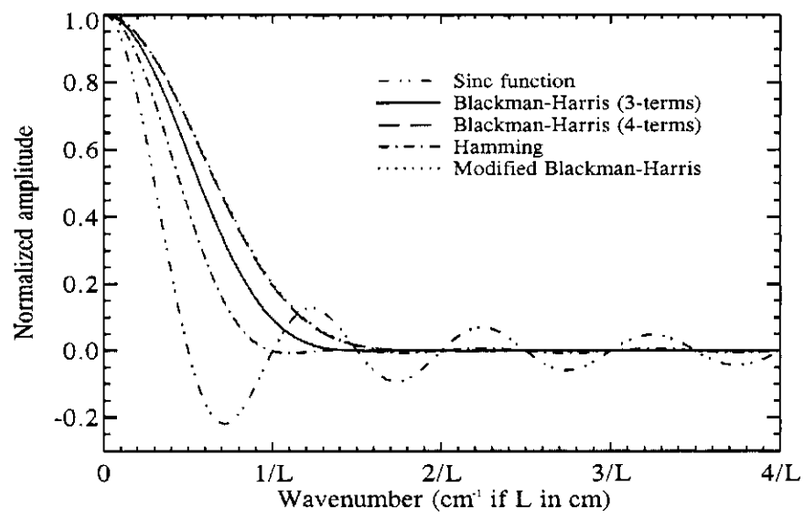

Figure 4.11: Instrumental line shapes of Blackman-Harris, Hamming and Adjusted Blackman-Harris apodizing functions

4.5.1 Finding the coefficients

The coefficients were found using the IDL® [53] Amoeba minimization routine. The IDL® program was written to perform the minimization. Starting from their functional form, the Norton-Beer functions 4.16 were Fourier transformed to determine the ILS and subsequently its FWHM. The magnitude of the largest secondary maximum (or minimum) was also calculated. The next step was to choose target FWHM with reference to the FWHM of the sinc function, for example 1.3, and to minimize the magnitude of the largest secondary lobes so that the function would fall on or below the empirical line on the Filler diagram. The program iterated until the number of iterations reached some limit (in practice this was set at 400). After each iteration, the program would plot the corresponding function locus on the Filler diagram. Once the program had converged, or reached the iteration limit, the corresponding point was plotted on the Filler diagram together with the empirical line described by equation 4.17. Upon convergence, the program returns the set of coefficients, C_i, that correspond to the minimized function. The number of terms required (n in the equation 4.16) to achieve convergence depended on the degree of apodization and ranged from n = 3 to n = 5 terms for FWHMs ranging from 1.1 to 2.0. In all cases the initial starting point on the Filler diagram was taken to be the locus of the sinc function. It was possible to determine all coefficients from the starting point. For completeness, the program was executed with different starting points and Amoeba would always converge to the same set of coefficients even when the starting point was a significant distance away from the starting position.

In order to determine the validity of the empirical line (equation 4.17) it was

decided to repeat this analysis with the target line shifted two decades below its nominal position on the Filler diagram. The result showed that the functions would converge to essentially the same value. This provides confidence that the empirical line (equation 4.17) is a real limit for this class of functions. As a further independent check of these results, a different minimization method, Powell method, was used to confirm the coefficients. The Powell method returned the same coefficients as the Amoeba method. This proved that we indeed have the right coefficients. In the next section we briefly describe the two methods used.

4.5.2 Amoeba or Downhill simplex method

The IDL function Amoeba minimizes functions using the downhill simplex method [54, 55]. The downhill simplex method performs multidimensional minimization ie., finds the minimum of a function with two or more independent variables. The simplex method does not require the knowledge of the derivative of the function and therefore the method finds frequent use. A simplex is a geometrical figure consisting, in N dimensions, of $N+1$ vertices and all their interconnected line segments and polygon face [55]. For example, in two dimensions, a simplex is a triangle and in three dimensions it is a tetrahedron. In multidimensional minimization, it is necessary to give a starting guess ie., $N+1$ points that define an initial simplex. If P_0 is the initial point then the rest of points can be found using the following formula $P_i = P_0 + \lambda e_i$, where, e_i are N unit vectors and λ is a guess of the problem's characteristic length scale [55].

The downhill simplex method takes a series of steps from an initial starting point, through the opposite face of the simplex, to a location where the function has a lower

value; these steps are called reflections. The method also can expand itself in one or more directions to take larger steps. When minimization reaches a "valley floor", the method contracts itself in the transverse direction and tries to go down the valley. Like all minimization algorithms, the convergence criteria can be complicated. Furthermore, since there is more than one variable, it is possible to define different tolerances for each. One method of checking for convergence is to determine when the next step size is lower than some predetermined value; conversely, for a given variable, the minimization can be assumed to be converged when the function value is less than some predetermined value.

4.5.3 Powell method

The Powell method of minimization [55, 56] uses the method of the direction set, which includes a set of directions along which the function moves towards its minimum. The Powell method uses what is called a conjugate direction set, which means that the minimization along one direction is not affected by the minimization along subsequent directions since these are linearly independent [55]. Starting from an initial point P_0, the method constructs $n+1$ lines through this point and searches for a minimum of the function along each line for the direction of largest decrease of the function. Each minimum along each direction line is stored as P_l where $l = 1..n$. The direction of the largest decrease is replaced by the direction given by $(P_n - P_0)$. The assumption of the scheme is that the substituted direction includes the replaced direction so that the resulting set of directions remains linearly independent [55]. The iteration process continues with the new starting position $P_0 = P_n$ until the minimum is reached.

FWHM	C_0	C_1	C_2	C_4	C_6	C_8
1.1	0.701551	-0.639244	0.937693	0	0	0
1.2	0.396430	-0.150902	0.754472	0	0	0
1.3	0.237413	-0.065285	0.827872	0	0	0
1.4	0.153945	-0.141765	0.987820	0	0	0
1.5	0.077112	0	0.703371	0.219517	0	0
1.6	0.039234	0	0.630268	0.234934	0.095563	0
1.7	0.020078	0	0.480667	0.386409	0.112845	0
1.8	0.010172	0	0.344429	0.451817	0.193580	0
1.9	0.004773	0	0.232473	0.464562	0.298191	0
2.0	0.002267	0	0.140412	0.487172	0.256200	0.113948

Table 4.4: Coefficients of the extended Norton-Beer apodizing functions.

4.5.4 Results

Using the method described above we have extended the analysis of Norton and Beer to derive the coefficients of 10 optimum apodizing functions that correspond to FWHM of 1.1 to 2.0 in steps of 0.1. The apodizing functions are shown in figure 4.12, the corresponding ILSs in figure 4.13 and the coefficients C_i are shown in table 4.4.

The locus of these apodizing functions are shown as red circles in figure 4.14; the three original Norton-Beer functions are shown as blue circles. Also shown is the location of the triangle (Bartlett) apodizing function, which, as mentioned earlier, although frequently used, is far from optimum.

4.6 Conclusion

In conclusion, numerous apodizing functions have been compared and contrasted in this chapter. It has been shown that some of them are far from optimum. We agree with Norton and Beer that there is evidence for an empirical line on the Filler diagram

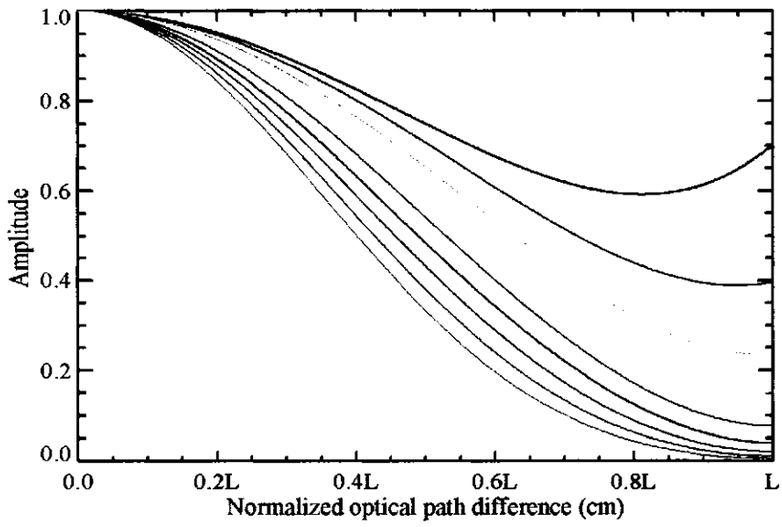

Figure 4.12: Ten extended Norton-Beer apodizing functions. The function corresponding to FWHM of 1.1 is in black, the rest of the functions in decreasing order of the tail amplitude correspond to FWHM of 1.2, 1.3 etc.

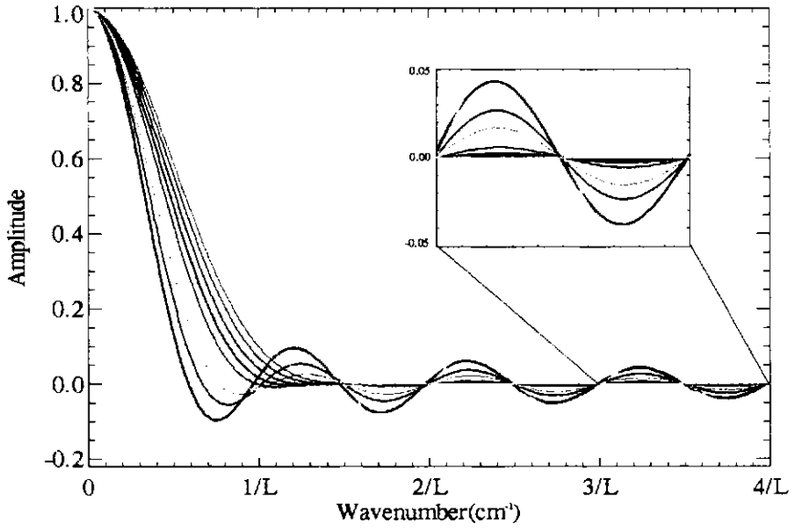

Figure 4.13: Instrumental line shapes corresponding to the 10 apodizing functions compared with the sinc function (pink line). Insert shows the magnified region of the third sidelobe.

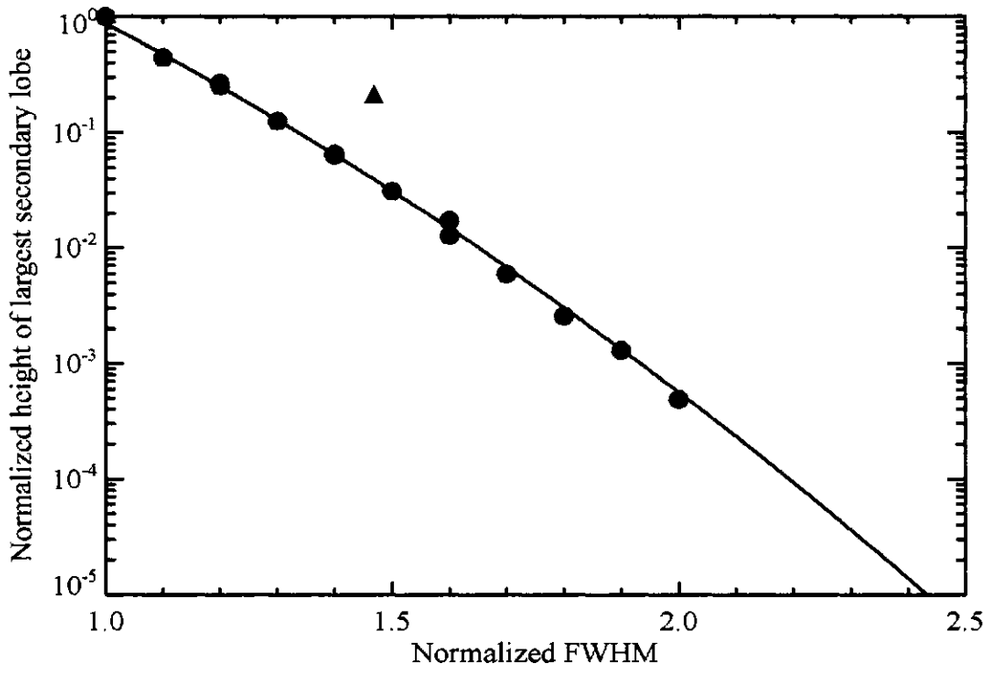

Figure 4.14: Extended Norton-Beer apodizing functions (red circles) compared with three original Norton-Beer apodizing functions (blue cirlcles) and the triangle (Bartlett) apodizing function (red triangle)

below which no optimum apodizing function exist. Our study of the extended Norton-Beer apodizing functions has led to derivation of 10 optimum functions. These functions can easily be used to study the tradeoff between resolution and the ringing of the ILS. These 10 new functions cover the range from 1.1 to 2.0 of FWHM in steps of 0.1. The FWHM, the height and the positions of the secondary minima and maxima of these functions are given in tables 4.5 and 4.6, respectively. Table 4.7 gives the percentage of the largest secondary lobe of these functions with respect to the central maximum.

Relative FWHM	FWHM	h_1	h_2	h_3	h_4	h_5
1.0	0.60364	-0.21723	-0.091325	-0.057973	-0.042479	-0.033525
		0.715525	1.736325	2.742149	3.745112	4.747042
1.1	0.66420	-0.096312	-0.075860	-0.050756	-0.037757	-0.029987
		0.750012	1.713789	2.726237	3.733150	4.737500
1.2	0.72424	-0.055039	-0.045200	-0.031224	-0.023451	-0.018701
		0.815562	1.734427	2.737289	3.740819	4.743405
1.3	0.78458	-0.027229	-0.026187	-0.019615	-0.015065	-0.012127
		0.893129	1.747848	2.741476	3.743089	4.744947
1.4	0.84468	-0.013897	-0.013639	-0.012602	-0.010128	-0.008296
		0.990710	1.744366	2.731459	3.734965	4.738350
1.5	0.90512	-0.006740	-0.005233	-0.006337	-0.005274	-0.004388
		1.093694	1.794395	2.755126	3.750099	4.749515
1.6	0.96542	-0.002756	-0.001781	-0.002705	-0.002569	-0.002242
		1.201594	1.885519	2.770838	3.754891	4.751677
1.7	1.02550	-0.001295	-0.000511	-0.001098	-0.001227	-0.001133
		1.324419	1.974661	2.788058	3.760063	4.754043
1.8	1.08598	-0.000064	-0.000313	-0.000380	-0.000550	-0.000551
		1.482119	2.061705	2.819646	3.767627	4.757247
1.9	1.14610	-0.000263	-0.000282	-0.000085	-0.000199	-0.000232
		1.644506	2.098222	2.903101	3.783034	4.762789
2.0	1.20662	-0.000104	-0.000083	-0.000104	-0.000105	-0.000101
		2.348144	3.776461	4.763836	5.758335	6.755960

Table 4.5: FWHM and height (upper row) and position (lower row) of the first five minima of 10 best apodizing functions in units of 1/L.

Relative FWHM	FWHM	h_1	h_2	h_3	h_4	h_5
1.0	0.60364	0.128375	0.070914	0.049029	0.037473	0.030332
		1.230154	2.239839	3.243821	4.246163	5.247804
1.1	0.66420	0.096291	0.061050	0.043331	0.033434	0.027178
		1.206513	2.220976	3.230148	4.235539	5.239143
1.2	0.72424	0.054493	0.037163	0.026814	0.020821	0.016972
		1.243239	2.235294	3.239185	4.242212	5.244445
1.3	0.78458	0.027323	0.022755	0.017081	0.013447	0.011037
		1.280246	2.242023	3.242146	4.244048	5.245779
1.4	0.84468	0.008161	0.013794	0.011295	0.009135	0.007587
		1.328441	2.231925	3.233072	4.236753	5.239763
1.5	0.90512	0.003573	0.006695	0.005802	0.004800	0.004033
		1.405000	2.264633	3.251529	4.249592	5.249655
1.6	0.96542	0.002738	0.002413	0.002696	0.002407	0.002089
		1.505329	2.301476	3.259629	4.252705	5.251229
1.7	1.02550	0.001252	0.000782	0.001217	0.001189	0.001071
		1.615708	2.343501	3.268347	4.256090	5.252965
1.8	1.08598	0.000555	0.000212	0.000501	0.000561	0.000532
		1.691538	2.419983	3.282272	4.260803	5.255272
1.9	1.14610	-0.00013	0.000102	0.000151	0.000223	0.000232
		1.830878	2.539345	3.315750	4.269465	5.259122
2.0	1.20662	0.000058	0.000097	0.000106	0.000104	0.000098
		3.284766	4.268922	5.260508	6.256902	7.255372

Table 4.6: FWHM and height (upper row) and position (lower row) of the first five maxima of 10 best apodizing functions in units of 1/L.

FWHM of Extended Norton-Beer functions relative to sinc	Height of secondary maxima as a percentage of total height
1.0	-21.723 %
1.1	-9.631%
1.2	-5.504 %
1.3	-2.732 %
1.4	-1.389 %
1.5	-0.674 %
1.6	-0.275%
1.7	-0.129 %
1.8	-0.031 %
1.9	-0.026 %
2.0	-0.010 %

Table 4.7: FWHM and height of the largest secondary maximum of 10 best Norton-Beer apodizing functions.

Chapter 5

Fourier transform spectroscopy of the Orion Molecular Cloud

5.1 Introduction

It is well known that the interstellar medium contains molecular clouds, regions of above average density, where, under the right conditions, star formation can take place. The main constituents of molecular clouds are dust and molecular gas. Dust, composed of solid grains that give rise to broadband emission, is best studied with a low-resolution spectrometer. Emission from the gas, on the other hand, which gives rise to narrow spectral features, is best studied using a high-resolution spectrometer. Photometric measurements, while generally more sensitive than spectroscopic measurements because radiation from all wavelengths within the bandpass of the infrared filter, which defines the photometric band, is measured at any given time, are unable to differentiate between the dust and gas

components of emission within the photometric band [35, 57]. The inability to differentiate between these two components of emission can lead one to misinterpret the underlying physics of the region under study.

The goal of this chapter is to determine the dust emission component of the brightest region in OMC, Orion-KL. The chapter divided into three parts. First, a theoretical model of dust emission Spectral Energy Distribution (SED) is developed and three techniques studied to determine the SEDs: dual-band photometry method, dual-band FTS method and single-band FTS method. Unfortunately, although we had four observing runs, inclement weather prevented us from obtaining spectroscopic FTS data at 450 μm. In the second part of this chapter, I will describe two methods used to extract the continuum from the 850 μm FTS band alone. Finally, the chapter concludes with an analysis of the molecular line emission observed with the FTS, through application of a technique commonly used in heterodyne spectroscopy known as rotation diagram analysis.

5.2 Spectral energy distribution

The spectral energy distribution, S_ν, at a frequency ν, can be expressed in terms of a spectral index, γ, which is related to the dust temperature, T, and the dust emissivity index, β, by [14]

$$S_\nu = (N_g M_g)\,\kappa_0 \left(\frac{\nu}{\nu_0}\right)^\beta B_\nu(T_d)\Omega \propto \nu^\gamma, \tag{5.1}$$

S_ν is measured in Jy, where 1 Jy = $10^{-26}\mathrm{Wm}^{-2}\mathrm{Hz}^{-1}$, κ_0 (m^2/kg) is the dust emissivity at some reference frequency ν_0, β is the dust emissivity index, and $B_\nu(T_d)$ ($\mathrm{Wm}^{-2}\mathrm{str}^{-1}\mathrm{Hz}^{-1}$) is the Planck blackbody function at frequency ν, for dust at temperature T_d, Ω is the solid

angle, N_g is the dust column density (m^{-2}) and M_g is the mass of the dust grains (kg). The Planck function, $B_\nu(T)$ is defined as

$$B_\nu(T) = \frac{2h\nu^3}{c^2}\frac{1}{e^{\frac{h\nu}{kT}} - 1}. \tag{5.2}$$

The units of the Planck function are $Wm^{-2}str^{-1}Hz^{-1}$. Expressed in terms of wavelength, λ, the ratio of the photometric fluxes at wavelengths of 450 and 850 μm can be written as [58, 59]:

$$\frac{S_{450}}{S_{850}} = \frac{e^{\frac{hc}{\lambda_{850}kT}} - 1}{e^{\frac{hc}{\lambda_{450}kT}} - 1}\left(\frac{\lambda_{850}}{\lambda_{450}}\right)^{3+\beta}. \tag{5.3}$$

The primary goal of this analysis is to determine the dust emissivity, β, but equation 5.3 shows this will require a knowledge of the dust temperature.

5.3 Methods of determining β

This section will discuss three different methods of determining the dust emissivity, β: Dual-band photometry, dual-band FTS spectroscopy and single-band FTS spectroscopy. A computer program was written in IDL® to model the SED of a molecular cloud. A cloud of temperature 30 K and dust emissivities, β, of 1.5 and 2 was modeled using equation 5.1. Under typical conditions experienced at Mauna Kea, the noise at 850 μm is an order of magnitude less than at 450 μm [60]. In this simulation, for simplicity, and based upon noise measured with SCUBA [60], it is assumed that the white noise of 1-σ has a value of 10 mJy at 850 μm and 100 mJy at 450 μm.

Figure 5.1 shows the SEDs for a model cloud having temperatures ranging from 10 to 50 K and for β of 1.5 and 2, arbitrarily normalized to an 850 μm band flux of 100

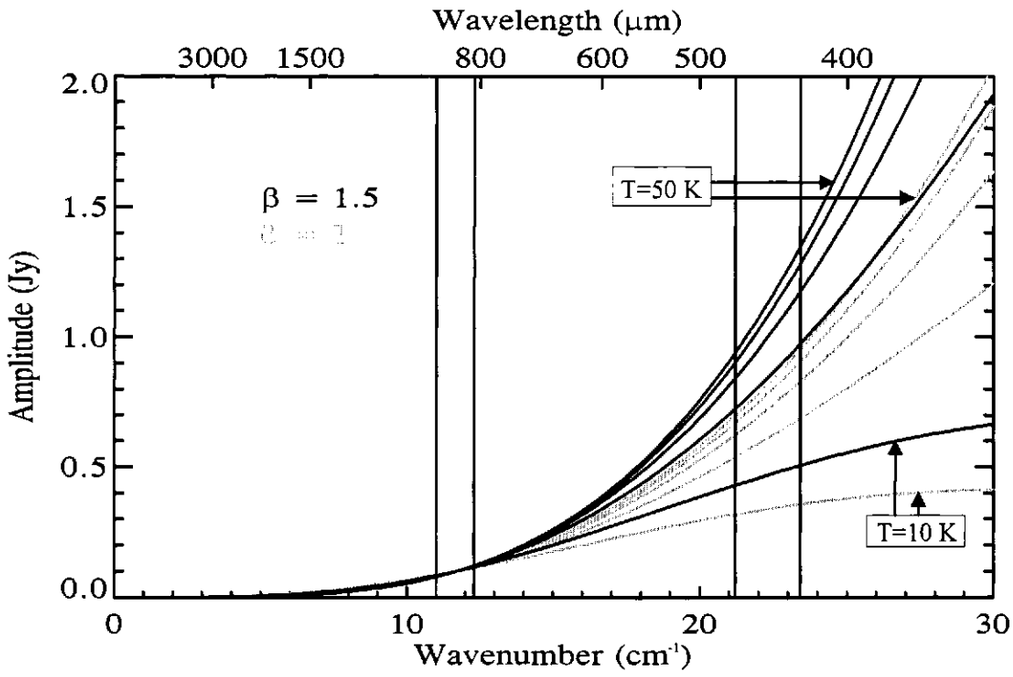

Figure 5.1: Model spectral energy distribution for source flux of 100 mJy at 850 μm, dust emissivity β = 1.5 and 2 and temperatures of 10, 20, 30, 40, 50 K. The passbands of the 850 μm and 450 μm bands are identified by solid black lines.

mJy. Figure 5.2 shows the same SEDs as in figure 5.1, with noise added as described above. The two regions bounded by solid lines correspond to the 450 and 850 μm filters matching the atmospheric transmission windows in which observations are possible from Mauna Kea, shown in figure 5.3 [61]. These models will be used in the next section to compare and contrast different methods of determining the dust emissivity, β. The 450 and 850 μm waveband regions, with added noise, were fitted to a function of the form of the equation 5.1 using the fitting routine MPFITFUN described in the section 5.3.3.

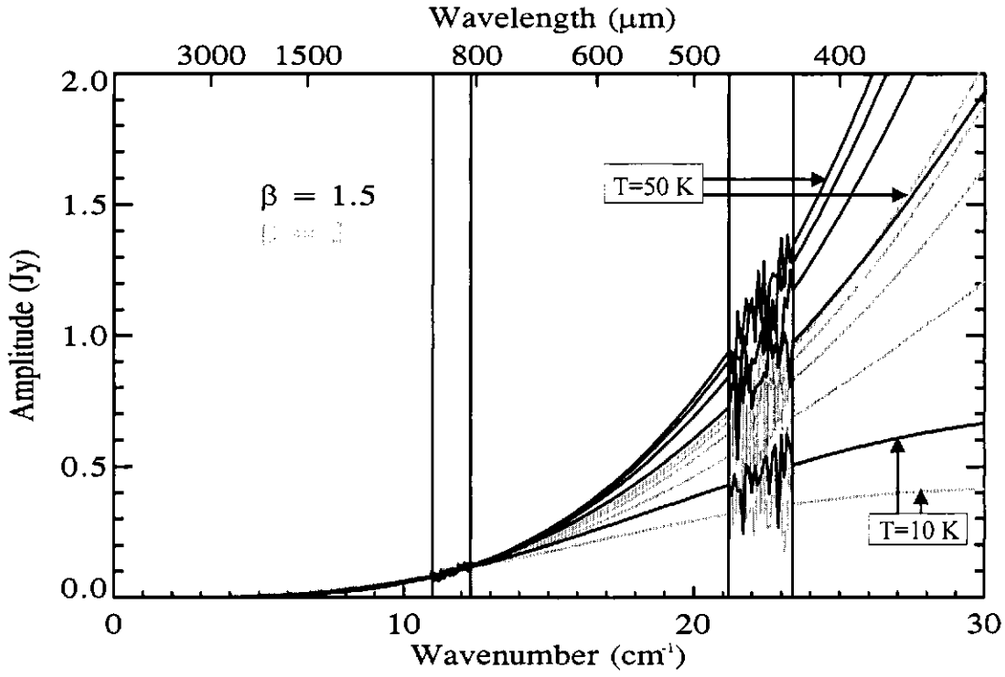

Figure 5.2: Model spectral energy distribution for source flux of 100 mJy, dust emissivity $\beta = 1.5$ and 2 and temperatures of 10, 20, 30, 40, 50 K. White noise was introduced into two bands as discribed in the text.

5.3.1 SCUBA 850 and 450 μm photometry

Estimates of dust emissivity can be obtained from SCUBA photometric measurements, at 850 and 450 μm, by inversion of equation 5.3. Photometric measurements have superior raw sensitivity when compared with the spectroscopic measurements taken with an FTS using a similar detector [35, 57]. This is due to the fact that radiation from all wavelengths within the bandpass of the infrared filter, which defines the photometric band, is measured at any given time. There are other difficulties with the dual band photometric method. The shape of the JCMT beam at 450 μm is far from ideal. In addition to

a narrow diffraction limited response of ~7", the beam has significant side-lobe response due to diffraction from the individual panels (~1m) that constitute the dish surface [62]. Because the beam sizes at 450 and 850 μm are so different, comparing photometric data at the two wavebands requires some assumptions with respect to the size of the emitting region and its coupling to the telescope in the two wavebands. Finally, observations at 450 μm are extremely sensitive to weather, because in this band, the adjacent water vapour lines are much stronger than at 850 μm. Figure 5.3 shows the atmospheric transmission at Mauna Kea at submillimetre wavelengths, from which it is seen that observations at 450 μm require the best observing conditions.

The data corresponding to T = 30 K and β =1.5 in figure 5.2 was used to determine β, using the dual-band photometric method. The fluxes, S_{450} and S_{850}, were determined by calculating the area under the curve in the 450 and 850 μm bands. Using equation 5.3, β was calculated as follows:

$$\begin{aligned}
\frac{e^{\frac{hc}{\lambda_{450}kT}}-1}{e^{\frac{hc}{\lambda_{850}kT}}-1}\left(\frac{\lambda_{850}}{\lambda_{450}}\right)^{3+\beta} &= \frac{S_{450}}{S_{850}} \qquad (5.4)\\
\left(\frac{\lambda_{850}}{\lambda_{450}}\right)^{3+\beta} &= \frac{S_{450}}{S_{850}}\frac{e^{\frac{hc}{\lambda_{850}kT}}-1}{e^{\frac{hc}{\lambda_{450}kT}}-1}\\
(3+\beta)\log\left[\frac{\lambda_{850}}{\lambda_{450}}\right] &= \log\left[\frac{S_{450}}{S_{850}}\frac{e^{\frac{hc}{\lambda_{850}kT}}-1}{e^{\frac{hc}{\lambda_{450}kT}}-1}\right]\\
3+\beta &= \log\left[\frac{S_{450}}{S_{850}}\frac{e^{\frac{hc}{\lambda_{850}kT}}-1}{e^{\frac{hc}{\lambda_{450}kT}}-1}\right]\left[\log\frac{\lambda_{850}}{\lambda_{450}}\right]^{-1}\\
\beta &= \log\left[\frac{S_{450}}{S_{850}}\frac{e^{\frac{hc}{\lambda_{850}kT}}-1}{e^{\frac{hc}{\lambda_{450}kT}}-1}\right]\left[\log\frac{\lambda_{850}}{\lambda_{450}}\right]^{-1}-3
\end{aligned}$$

The next step was to use equation 5.4 to determine β while varying the estimate of the temperature, T, of the cloud. Starting at the guess temperature of 10 K up to the

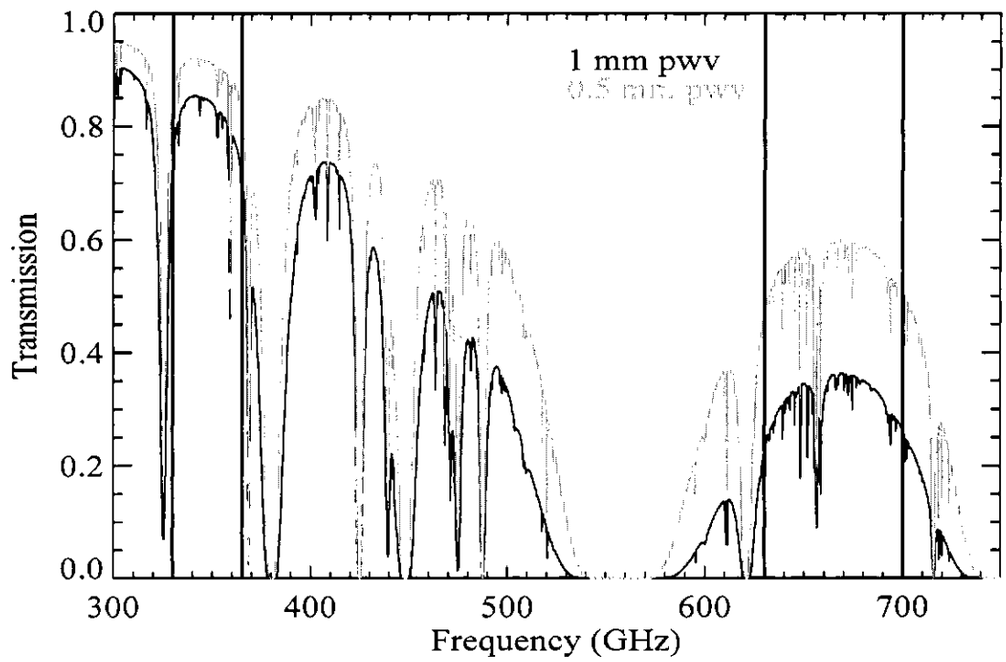

Figure 5.3: The transmission of the atmosphere: at 1 mm precipitable water vapour (black) and at 0.5 mm precipitable water vapour (gray), corresponding to average and excellent observing conditions, respectively. The spectral range of the 850 μm band is from 330 - 365 GHz and for the 450 μm band is from 630 - 700 GHz.

temperature of 50 K, in steps of 1 K, β was calculated. The uncertainty in the derived β was calculated by taking the difference between the derived β and the true β of 1.5 ie., $(\beta - \beta_{true})$. The result is shown in figure 5.4. The brown curve in the upper plot of figure 5.4 shows the difference between the retrieved and modeled β, using the photometric method for a cloud having a temperature of 30 K. It is readily seen that as the assumed temperature deviates from the model value of 30 K, the errors in retrieved β become large. One of the biggest difficulties in determining β using the photometric method lies with estimating the temperature of the source region; small errors in the assumed source temperature translate

to large errors in the retrieved β. This can be readily seen from figure 5.1. Consider the model with T = 20 K and $\beta = 2$ and the model with T = 50 K and $\beta = 1.5$. The integrated fluxes at 450 μm are 845 and 820 mJy, respectively. Since the integrated flux at 850 μm is 100 mJy in both cases, the ratio between 450 and 850 μm fluxes is virtually identical, this illustrates that the determination of β from the dual-band photometric method is heavily dependent on the assumed source temperature.

5.3.2 FTS 850 and 450 μm (dual-band) spectroscopy

FTS observations at 850 and 450 μm have lower sensitivity than equivalent photometric observations since the energy is now being measured in smaller wavebands rather than a full waveband. FTS observations share the same source-telescope coupling and weather-related issues as photometric measurements. However, the FTS data can, in principle, be used to extract the source temperature of the emitting region, and subsequently to determine β, removing the reliance on the assumed source temperature.

For this method, the same model cloud was used as in the previous section, ie., T = 30 K and $\beta = 1.5$ in figure 5.2. The noisy data from the two bands was isolated and fitted with a function of the form in equation 5.1, using the IDL® fitting algorithm MPFITFUN. The algorithm is based upon the Levenberg-Marquardt technique, which finds the best set of model parameters that match the data by minimizing the sum of the weighted squared differences between the model and the data [63]. The lower plot in figure 5.4, (an expanded version of the upper plot), shows the differences between the retrieved and modeled β, ie., $(\beta - \beta_{true})$. The pink trace is the difference in β when the temperature is a free parameter fitted by the fitting function and the blue trace is the difference in β when the temperature

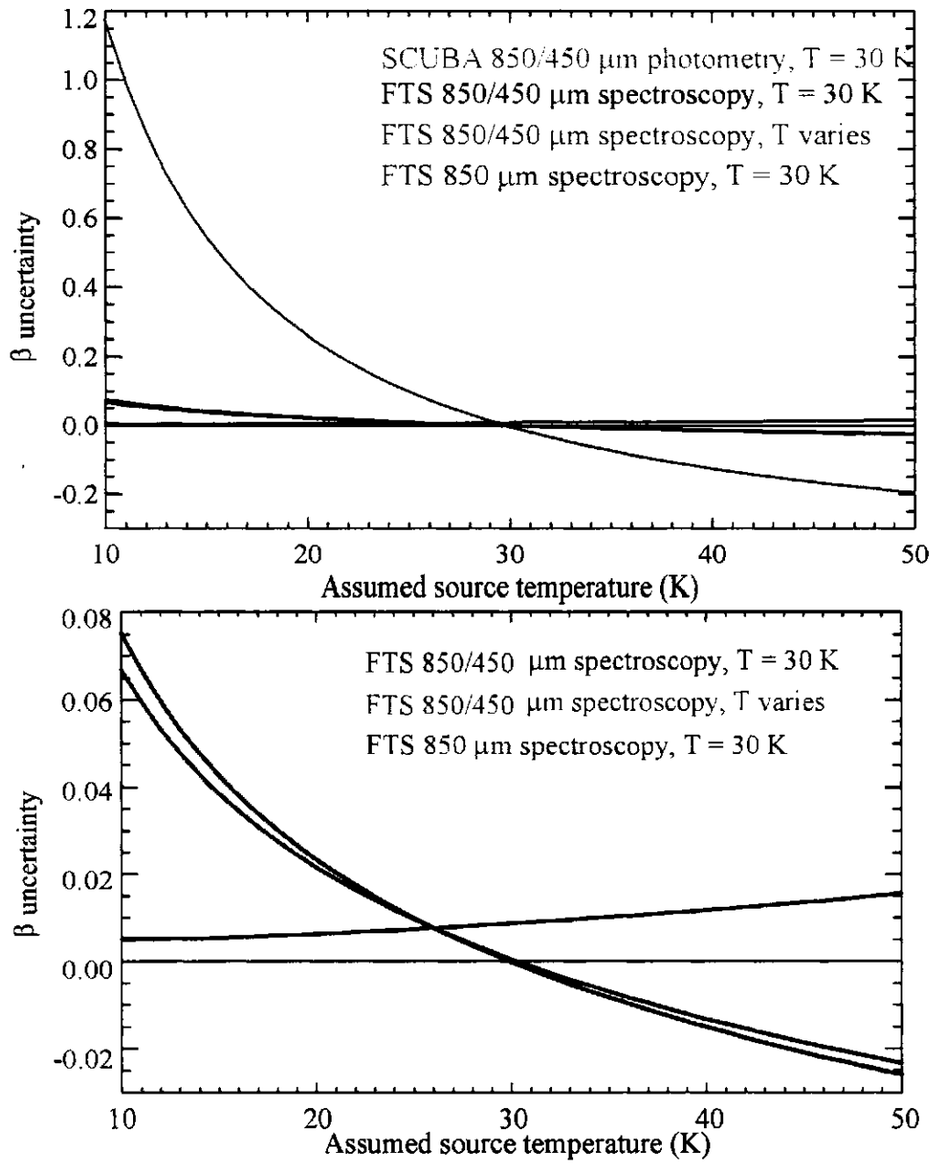

Figure 5.4: Uncertainty in derived β as a function of temperature for different observation methods (upper plot). Uncertainty in derived β as a function of temperature excluding the photometric dual-band method (lower plot)

is assumed to be fixed at 30 K. As the assumed temperature deviates from 30 K the errors in retrieved β increase, as expected, but they are still an order of magnitude less than the errors in equivalent SCUBA photometric measurements (section 5.3.2). The reason for this is that the temperature of the cloud can be, in principle, determined from the FTS spectrum by the fitting method described above, which fits to the different slopes of the continuum emission in the individual bandpasses at 850 and 450 μm.

5.3.3 FTS 850 μm (single-band) spectroscopy

FTS observations in the 850 μm band have several advantages over both previous methods: the JCMT has a well defined beam profile (essentially Gaussian) of 15", and the weather plays less of a role at this wavelength than at 450 μm [61]. The steps in determining β for this method are the same as in the dual-band FTS method, except that there is now only one band to consider.

The most important result is that the retrieved β is less sensitive to errors in the assumed temperature when compared with the dual-band photometry method in section 5.3.2, due to the fact that the longer wavelengths are closer to the Rayleigh Jeans regime. The red trace in figure 5.4 shows the differences between retrieved and modeled β when the temperature of the cloud is assumed to be fixed at 30 K. As the assumed temperature deviates from 30 K, the errors in retrieved β increase but are, again, significantly less, by roughly an order of magnitude, than those obtained with the photometric method (section 5.3.2). Table 5.1 lists the errors in the retrieved β associated with the three methods described above for three different estimates of the temperature. The true β for the simulated data was 1.5.

Measurement method	β assuming T = 30 K	β error assuming T = 20 K	β error assuming T = 40 K
SCUBA 850/450 μm	1.503	+0.122	-0.263
FTS 850/450 μm	1.5002	+0.0149	-0.0242
FTS 850 μm	1.4995	+0.0136	-0.0212

Table 5.1: Comparison of errors in retrieved β

5.4 Using FTS spectra to determine the continuum component of emission from Orion-KL

As mentioned earlier, poor weather during the three observing runs prevented FTS observations at 450 μm. This section will describe two approaches used to determine the SED of the Orion-KL region using the single-band spectroscopic method at 850 μm, described in section 5.3.4. The first approach fits a function of the form $A\nu^{\gamma}$ to the regions of lowest spectral line content of the observed FTS data of the Orion-KL region. The second approach uses a high resolution heterodyne spectra of Orion-KL, a knowledge of the instrumental line shape of the FTS and a function of the form $A\nu^{\gamma}$ to fit to the FTS spectrum of the Orion-KL region. First, it is necessary to describe the heterodyne data used in this analysis.

5.4.1 Heterodyne spectroscopy versus FTS spectroscopy

While heterodyne spectroscopy provides the highest spectral resolution measurements of any commonly used spectrometer [64, 6], it does so over a limited spectral range and often has baseline drifts that make it difficult to determine any continuum components of emission. FTS spectroscopy, on the other hand, is capable of simultaneously measur-

ing the continuum and line components of emission, although at only moderate spectral resolution (0.1-0.005 cm^{-1} (150-3000 MHz) in the case of U of L FTS). To compare the heterodyne and FTS spectroscopic techniques, one set of data for each was obtained during the December 2000 observing run at the JCMT. Both observations were done at a wavelength of 850 μm.

The FTS observations were made with the U of L FTS [5]. One input port of the FTS viewed the source and the other port viewed an open dewar filled with liquid N_2. The data were taken at spectral resolution of 150 MHz, or equivalently 0.005 cm^{-1}. The size of the JCMT beam at 850 μm is $\sim$15". There were 146 interferograms taken in the frequency range of 322 - 371 GHz (10.73 - 12.37 cm^{-1}), with each source interferogram followed by an interferogram of the background sky offset by 900" in right ascension (RA) from the source. RA was chosen as the direction to nod to minimize contamination from other regions of OMC, which, as discussed earlier, has filamentary structure running more or less north to south [3]. The offset in RA is calculated so that the observations of source and background sky are done through approximately the same airmass; however, atmospheric variability is still the dominant noise source. Atmospheric variability is the major problem because it introduces noise into the interferogram, which subsequently translate to noise in the spectra. Modelling, done with the University of Lethbridge Transmission and Radiance Model (ULTRAM), shows that atmospheric emission at 850 μm is several thousands Janskys (Jy) [65]. By comparison, the emission from brightest region of Orion is $\sim$ 167 Jy, while the emission from the majority of the compact sources in the OMC is less than a few Jy, in the 850 μm band. For this reason, it is necessary to take careful account of the contribution of

atmospheric emission from the spectrum of Orion. For these observations, the amount of precipitable water vapour (pwv) was on average 1.5 mm. By use of an atmospheric model [65], the pwv can be converted to an optical opacity, τ, by the equation 5.5. This gives the opacity of 0.09 at 225 GHz [66].

$$PWV = 20\tau - 0.32. \tag{5.5}$$

The heterodyne spectra of the Orion-KL region in the 850 μm band were obtained at the JCMT using Rx B3 heterodyne receiver [67]. Thirty scans of two brightest regions in OMC known as Orion-KL and Orion-S were obtained in the frequency range of 322 - 371 GHz (10.73 - 12.37 cm^{-1}). Each scan was of the frequency range 2 GHz with the resolution 1.25 MHz; successive scans had 100 MHz overlap. As with the FTS measurements, the effects of the atmospheric emission were minimized by position switching to the background position offset by 900" in RA. The individual heterodyne scans were merged using a program called SPECX [68, 69], which outputs spectra in FITS format. The final merged spectrum is shown in the upper plot of figure 5.5. It is obvious from this plot that each scan has a different baseline offset, due to the atmospheric variability or the calibration errors from tuning the receiver. Following a standard procedure, a linear baseline was removed from each individual scan. The final heterodyne spectrum with baseline removed is shown in the lower plot of figure 5.5. The amplitude of the spectral lines is expressed in antenna temperature, a common unit in radio astronomy, which is the signal power received at the telescope expressed in Kelvin [70].

The upper plot of figure 5.6 shows the FTS spectrum of the Orion KL region [5]; the classical instrumental line shape of the FTS (sinc function) is evident, and a clear

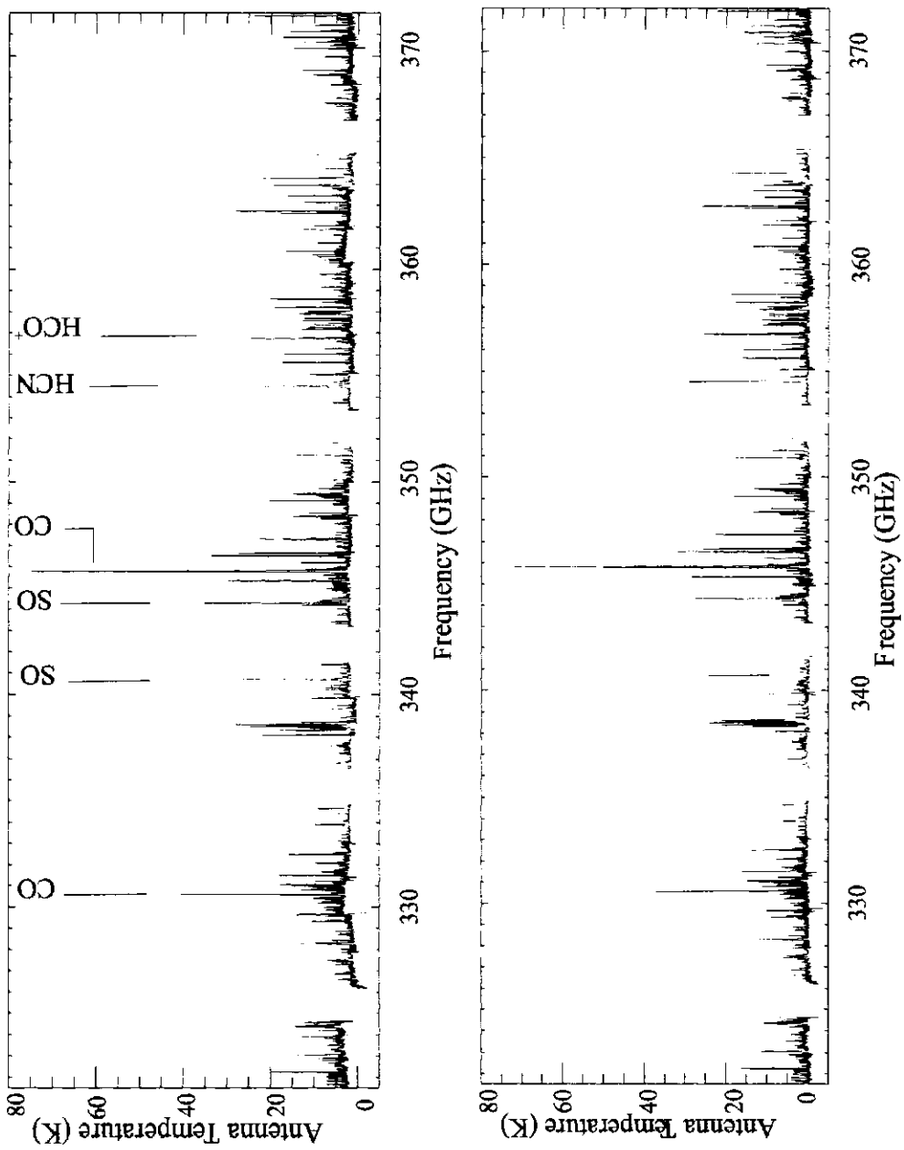

Figure 5.5: (Upper plot) The raw heterodyne spectrum of Orion-KL showing the variation in baseline between individual scans. Some of the more clearly identified lines are shown. (Lower plot) The raw heterodyne spectrum of Orion-KL with the baseline corrected.

continuum component can be seen. It is the continuum component that carries information on the properties of the dust in molecular clouds, such as the dust temperature and the emissivity. These properties are determined through analysis of the SEDs, which was discussed in the previous section. By comparison, the lower spectrum in the figure 5.6 is the earlier result of Serabyn [64]. Equally important, it is the only other FTS measurement of Orion to date. The spectrum is seen to be of lower resolution with no evidence of sinc line shape as would be expected from an FTS. Moreover, it is evident that the baseline, which would represent any continuum emission, has been removed.

5.4.2 Orion-KL 850 μm analysis

The upper spectrum of figure 5.6 exhibits the classical sinc instrumental line shape function of an FTS given by equation 4.4. When the heterodyne spectrum from the lower plot of figure 5.5 is convolved with the sinc function of the appropriate resolution (150 MHz or 0.005 cm^{-1}), the FTS and convolved heterodyne spectra are seen to be in close agreement as seen in figure 5.7. A measure of this agreement is the integrated line flux within the 850 μm band; the integrated line flux for the FTS spectrum is determined to be 34.1 $\pm$ 2 K*GHz, and for the heterodyne spectrum it is 35.7 $\pm$ 1 K*GHz. This level of agreement between two independent instruments shows that the FTS is capable of precision spectral photometry.

The existence of an underlying continuum flux can also be seen by figure 5.7; a clear baseline offset of approximately 2 K and a noticeable slope to the data are evident. In order to extract the underlying continuum flux, two methods have been developed. In the first method, the heterodyne spectrum of Orion-KL was carefully examined to determine eight

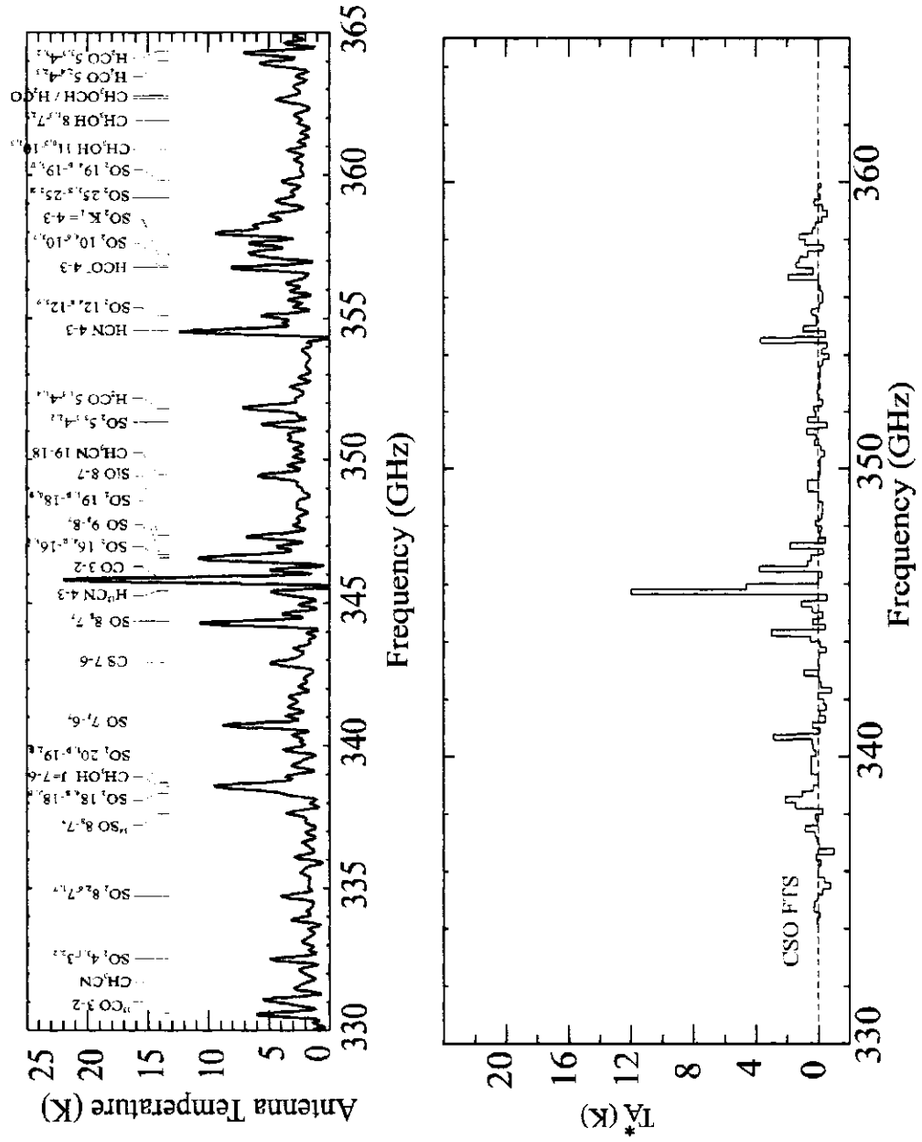

Figure 5.6: (Upper plot) Spectrum of Orion-KL taken with Fourier Transform Spectrometer, most of the prominent spectral lines are identified. (Lower plot) Spectrum of Orion-KL taken with Caltech Submillimeter Observatory Fourier Transform Spectrometer. In comparison to the upper plot, the spectral lines resemble a histogram [5]. The identification of spectral lines was done by comparing the spectrum to Schilke et al. [6] heterodyne spectrum of the same region.

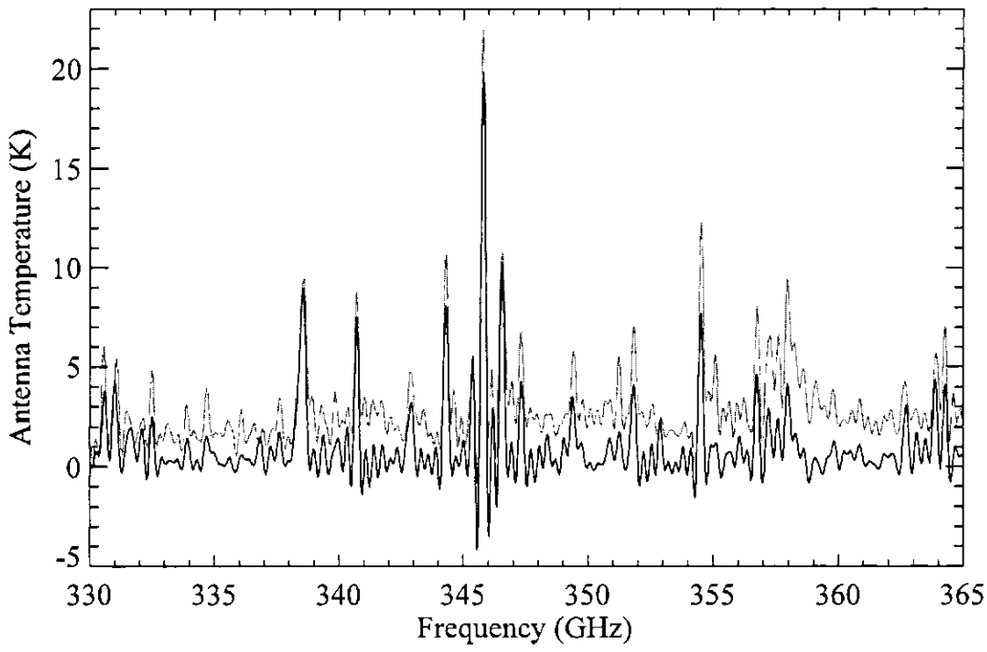

Figure 5.7: Comparison of FTS spectra of Orion molecular (gray trace) with the convolved heterodyne spectra (black trace).

spectral regions that had the lowest integrated line intensity. However, the continuum component cannot be determined from the heterodyne spectrum because, as mentioned earlier, the baseline has been removed in processing. The corresponding regions of the lowest integrated line intensity in the FTS spectrum were determined and averaged. The eight resulting photometric values were then fitted to a function of the form $A\nu^{\gamma}$, using the algorithm MPFITFUN, to extract the spectral index. In the Rayleigh-Jeans region (where $h\nu << kT$), the Planck function can be rewritten as $B_{\nu}(T) \approx \frac{2\nu^2 kT}{c^2}$, so $\gamma = \beta + 2$. Figure 5.8 shows the best fit to the averaged data from regions of few spectral lines and yields a spectral index, γ, of 3.54 $\pm$ 0.80 or, equivalently, β of 1.54 $\pm$ 0.8, in the Rayleigh-Jeans

limit.

The second method uses the same algorithm to fit the entire FTS spectrum to the heterodyne spectrum, which is first convolved with the instrumental line shape of the FTS (a sinc function of FWHM 150 MHz or 0.005 cm^{-1}) plus the continuum term ($A\nu^{\gamma}$). Again, the spectral index and its associated 1-σ standard error is returned by the fitting function. Figure 5.9 shows an expanded region of FTS data along with the fit returned by the program. This method yields a spectral index, γ, of 3.59 with the 1-σ standard error of + 1.22 and - 1.13. In the Rayleigh-Jeans limit, β becomes 1.59 with the 1-σ standard error of + 1.22 and - 1.13.

It is well known that line emission from Orion-KL is a significant fraction of the total 850 μm band flux [6]. Johnstone et al. [3] have determined the spectral index of Orion-KL to be 2.2, while the mean spectral index of Orion molecular cloud was measured to be 3.6 $\pm$ 0.4. This is shown in figure 5.10, where it is seen that the SED of Orion-KL is much lower than other sources. There are two reasons why the spectral index of Orion-KL is expected to be low as compared to the mean spectral index of the OMC. The first is that the spectrum of Orion-KL could contain numerous spectral lines, which contribute to the emission and thus lower the spectral index. The second reason is that the dust grains in the cloud may be covered in icy mantles, which makes the emissivity, β, of the dust, and hence its spectral index, lower. From this technique, we determined the line contribution for Orion-KL to be 32 % $\pm$ 2 %. This is to be compared with previous estimates of the line contribution of the total emission which are in the region of 25-50 % [64]. Our results show that, when the spectral line component of emission is accounted for, the derived SED from

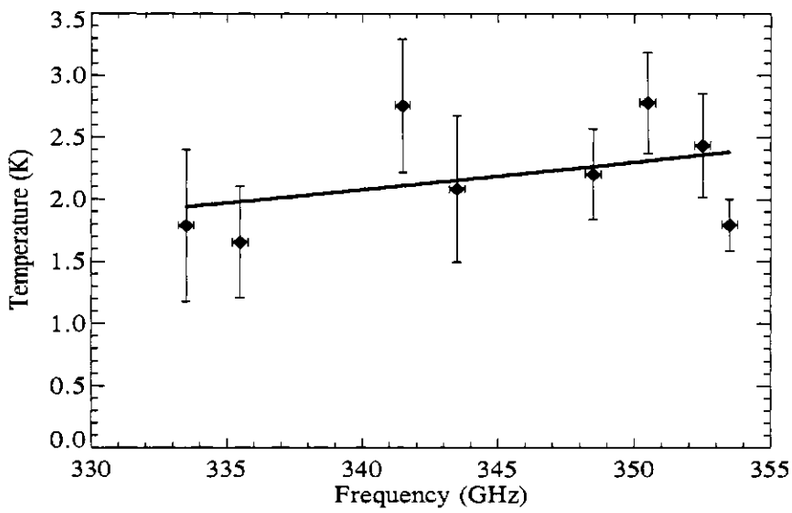

Figure 5.8: Fitting $A\nu^{\gamma}$ to the regions of lowest spectral line content in the Orion-KL spectrum.

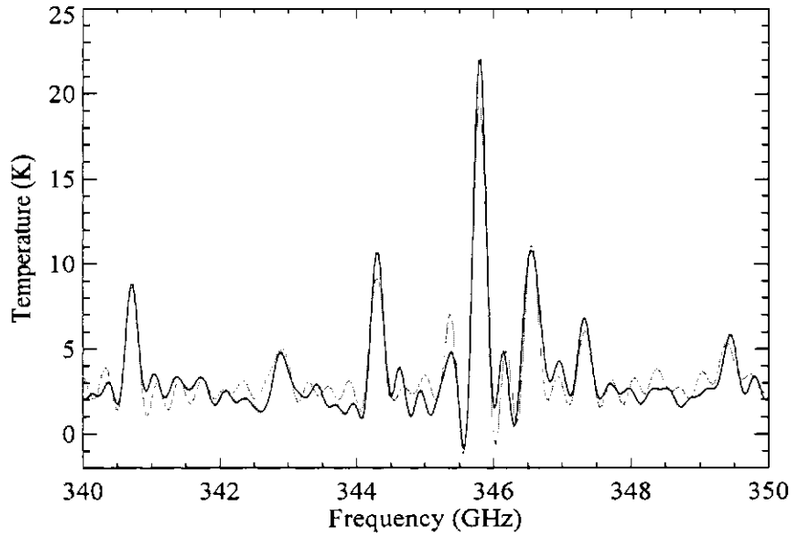

Figure 5.9: Comparison of FTS spectra of Orion-KL (black trace) with fitted continuum plus sinc convolved heterodyne spectra of the same region (gray trace).

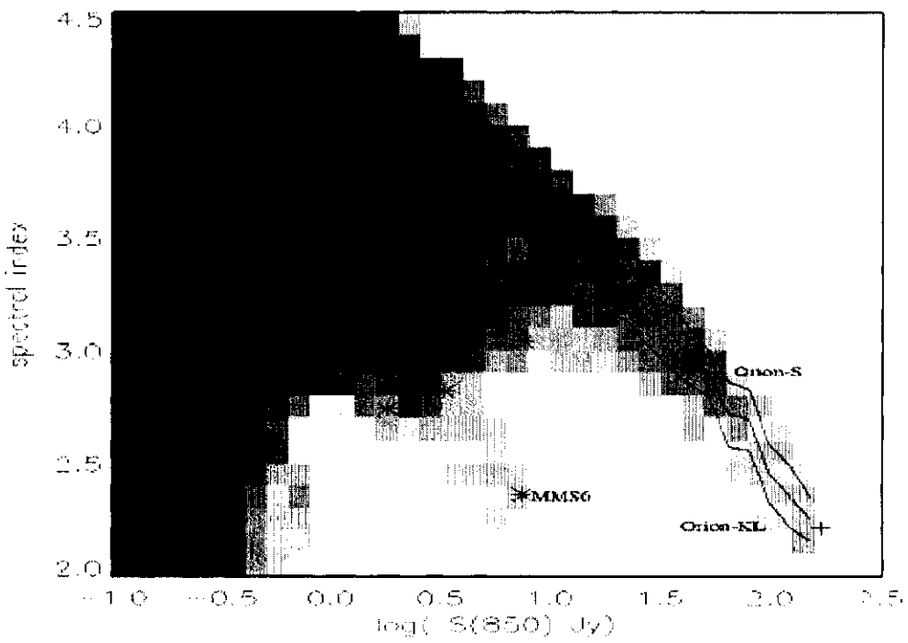

Figure 5.10: A map of the mean spectral index, γ, as a function of 850 μm flux (Jy), along with $\pm 1\sigma$ error estimate of the Orion Molecular Cloud taken with SCUBA photometer [3]

the 850 μm band is close to the average value determined from the SCUBA maps of the Integral Shaped Filament (ISF) [3]. These are the first results of their kind, and, although the error bars are large, the results agree well with previous work done with photometric measurements.

5.4.3 Orion-KL 450 μm analysis

As discussed in section 5.3.2., 450 μm band observations are very difficult because the atmospheric transmission and variability are often poor. For this reason, we only have two surveys of this region, due to Serabyn [64], and Schilke [71] to compare with our

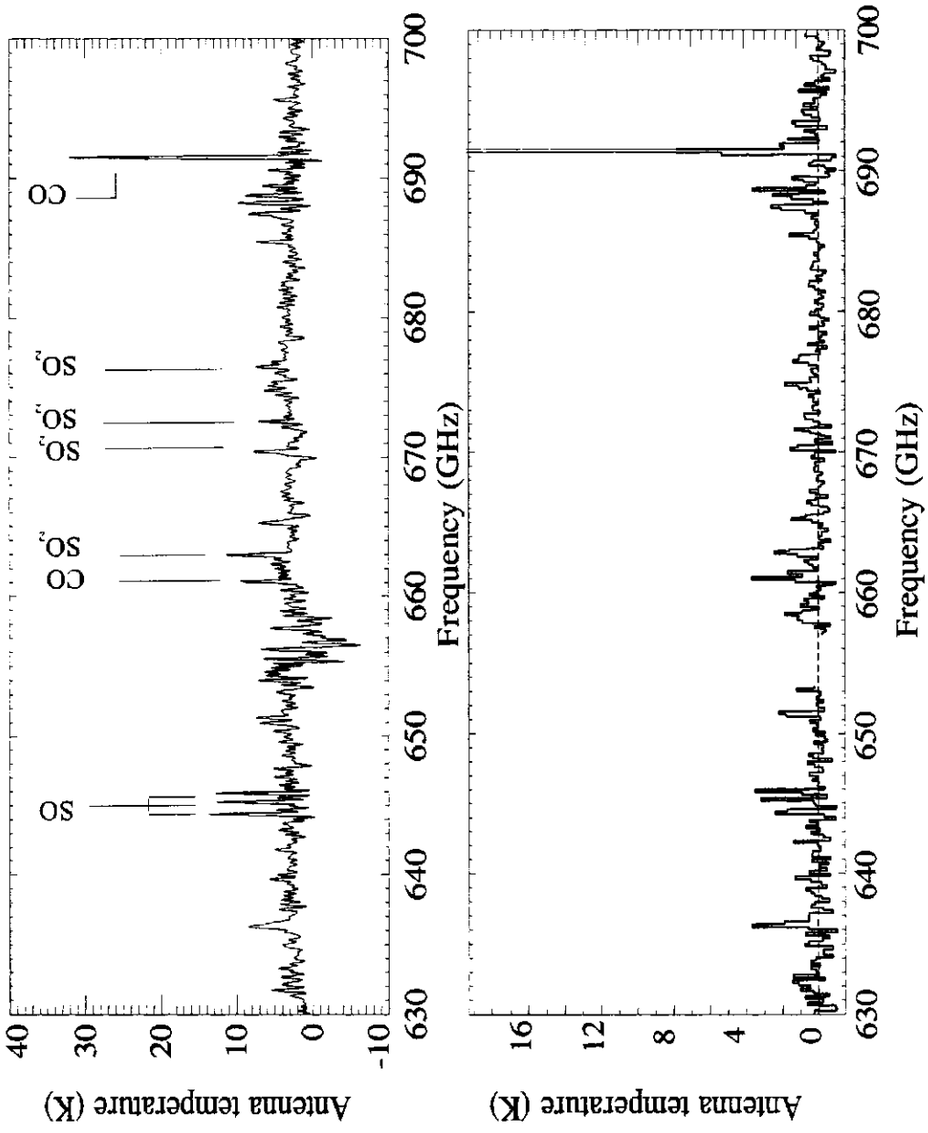

Figure 5.11: Spectrum of Orion-KL at 450 μm taken with the U of L FTS at a resolution of 150 MHz or 0.005 cm^{-1} (upper plot). Spectrum of Orion-KL at 450 μm taken with the CSO FTS with the 200 MHz resolution (lower plot) [5].

results. Serabyn's spectrum was obtained using an FTS at the CSO, while Schilke's work was obtained with a heterodyne receiver at the CSO. Unfortunately, we do not have access to the data of Schilke analysis so we will restrict our analysis to the spectrum of Serabyn. Figure 5.11 shows a plot of the 450 μm band Orion-KL spectrum for two different FTS spectrometers: the upper trace shows the U of L FTS spectra, shown in red, and the lower trace shows the CSO FTS spectrum shown in blue. The atmospheric pwv during the U of L FTS observation of December 2001 was approximately 0.9 mm which corresponds to an optical opacity, τ, of 0.061 (equation 5.5). Only 16 interferograms were acquired at a wavelength of 450 μm; half on source and half off source. It is evident from the figure 5.11 that while the Lethbridge FTS spectrum is noisy, several spectral lines are identifiable. As was the case in the 850 μm analysis, (section 5.4.2), the U of L spectrum is seen to be of higher resolution (150 vs. 200 MHz) and exhibits the classical sinc function expected of an FTS. Unfortunately, the quality of the 450 μm data was insufficient to attempt fitting the underlying continuum.

5.5 Orion-S analysis

During the December 2001 observing run, the heterodyne and the FTS spectra of the Orion-S region were obtained. Orion-S is located 90" south of Orion-KL, and is known to have fewer molecular line transitions than Orion-KL [3]. The heterodyne spectra of the Orion-S region in the 850 μm band were obtained using Rx B3 heterodyne receiver at the JCMT [67]. Thirty scans were obtained, covering the frequency range of 322 - 371 GHz in intervals of 2 GHz with the resolution 1.25 MHz. Successive scans had 100

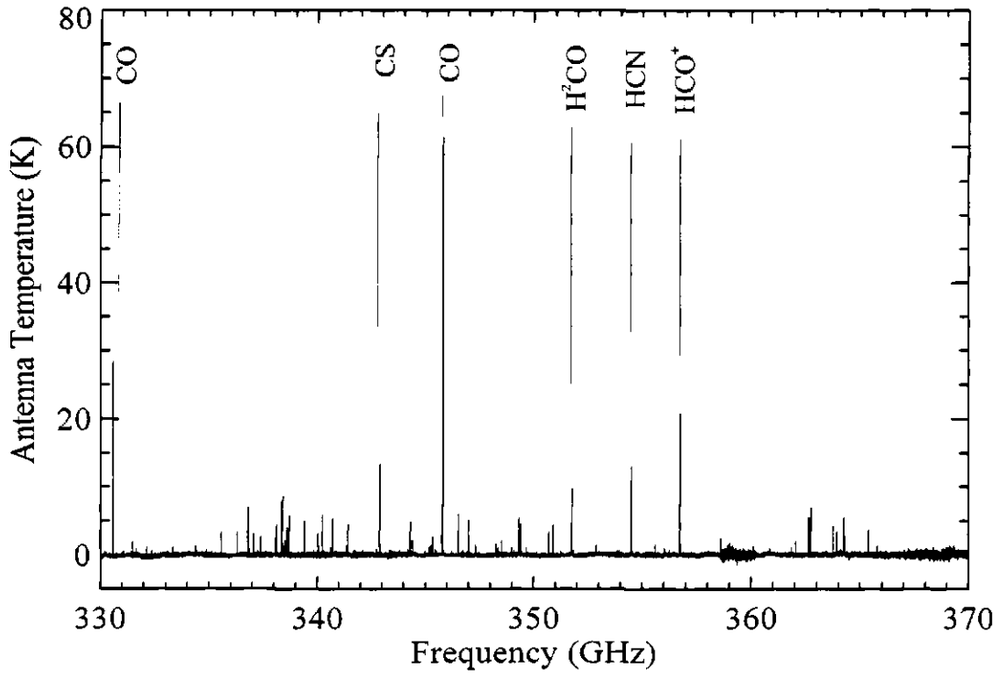

Figure 5.12: Heterodyne spectrum of Orion-S. Some of the most prominent spectral lines are identified on the plot.

MHz overlap. As discussed in section 5.4.1, the effects of the atmospheric emission were minimized by position switching against a background position offset by 900" in RA. The resulting spectrum is shown in figure 5.12. It can be seen in this figure 5.12 that there are fewer spectral lines in the Orion-S spectrum compared to the Orion-KL spectrum, and the lines are also weaker.

Two sets of FTS data for Orion-S were obtained during this run, one set of 28 interferograms (14 on source and 14 off source) from the December 2001 run and the other set of 44 interferograms (22 on source and 22 off source) from the October 2002 run. The atmospheric optical opacity at 225 GHz for these dates were 0.056 and 0.081, respectively.

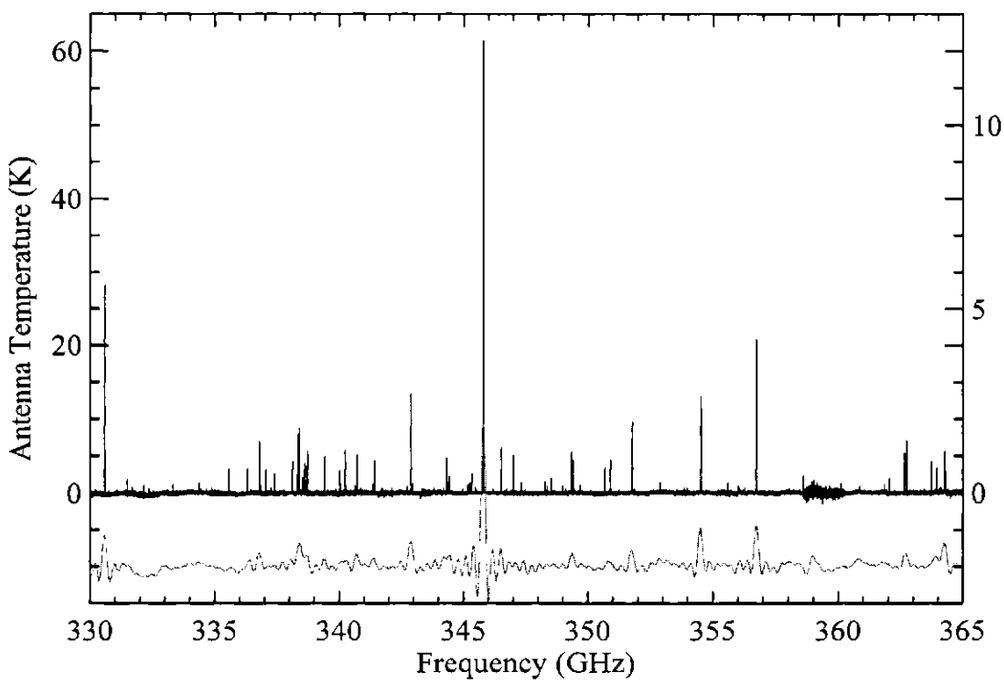

Figure 5.13: Heterodyne spectrum of Orion-S (black trace) convolved with the FTS instrumental line shape (gray trace) displaced -10 K for clarity.

As discussed above, the first step in the analysis was to take the heterodyne data and convolve it with the sinc function of FWHM of 150 MHz to simulate the instrumental line shape of an FTS. The result is shown in figure 5.13. The red curve shows the heterodyne data convolved with a sinc function.The next step was to analyze the FTS data and compare it to the convolved heterodyne data. It can be seen from the results, shown in figure 5.14, that the FTS data (upper trace) are noisy. Some of the lines can be identified but the SED could not be determined since the atmosphere was not stable enough to allow the determination of the continuum. However, with the more sensitive detectors and better weather, the determination of the SEDs for Orion-S would be possible. Although weather

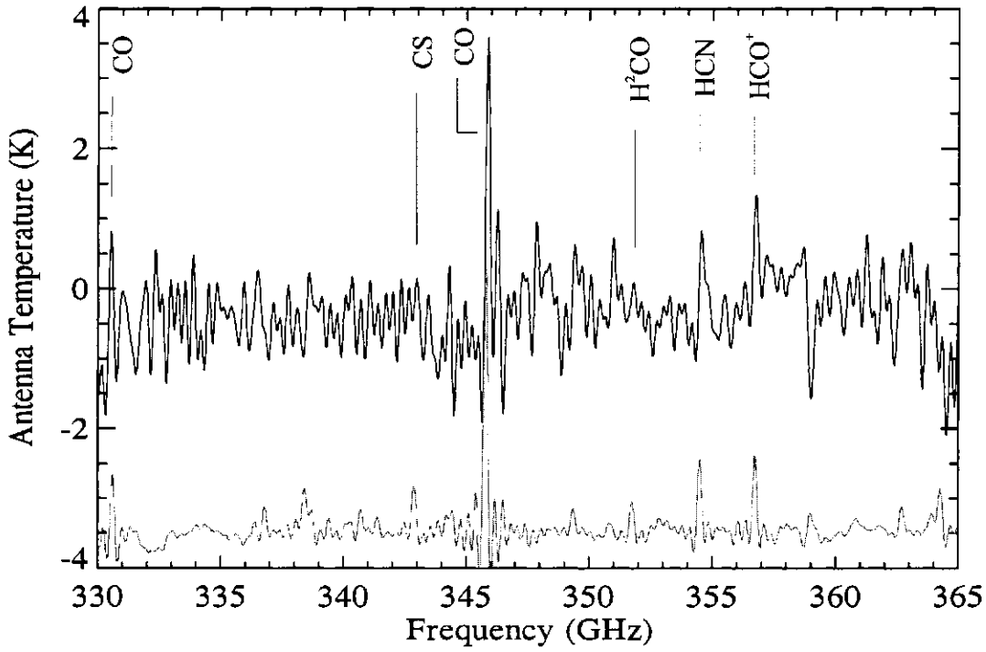

Figure 5.14: Measured FTS spectrum of Orion-S (black curve) compared to convolved heterodyne spectrum (gray curve) displaced -3.5 K for clarity.

prevented obtaining the dual band FTS data, and the 850 μm data of Orion-S was of low quality, the results presented in this section are first of their kind and serve to illustrate the potential use of FTS spectroscopy in continuum measurements of the ISM.

5.6 Using FTS spectra to determine spectral line component of emission for Orion-KL

Although the spectral resolution of an FTS cannot compare with heterodyne spectrometers, since the spectral resolution of heterodyne spectrometers is over two orders of

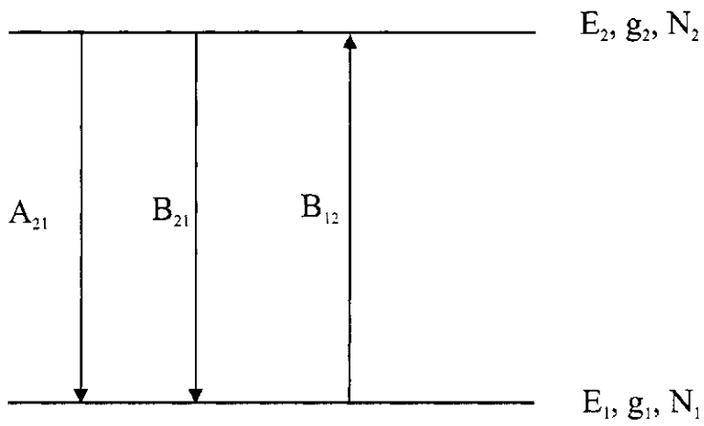

Figure 5.15: The emission and absorption processes for a two level atom. N_2 and N_1 are the populations of the levels 2 and 1, respectively, g_2 and g_1 are the degeneracies of the two levels, and E_2 and E_1 are the energies of the levels.

magnitude better than the FTS spectrometer, many spectral features can be identified in FTS spectra. We have borrowed a technique from heterodyne spectroscopy, known as the rotation diagram technique, to analyze data shown in figure 5.6.

5.6.1 Background: Emission and absorption processes for a two-level atom

The radiative emission and absorption processes for a two-level atom are shown in figure 5.15. In this figure, E_2 and E_1 are the energies of the two levels, g_2 and g_1 are the degeneracies of the two levels and N_2 and N_1 are the populations of the two levels.

In a steady state, the rate of loss from level two is equal to the rate of gain to level one and vice versa, allowing one to write

$$-\frac{dN_2}{dt} = \frac{dN_1}{dt} = A_{21}N_2 + B_{21}\rho(\nu)N_2 - B_{12}\rho(\nu)N_2, \tag{5.6}$$

where A_{21} is the Einstein coefficient (s^{-1}) for spontaneous emission, B_{21} and B_{12} are the

Einstein coefficients for stimulated emission ($m^3/(Js^2)$) and $\rho(\nu)$ is the density of the radiation field (Js/m^3). In absence of the external radiation field, the solution for this differential equation becomes:

$$N_2(t) = N_2(0)\exp(-A_{21}t).$$

If the system is maintained in thermal equilibrium, then the Maxwell-Boltzmann distribution defines the probability that a level is thermally populated. Generalized to all states, the ratio of the population in upper state, j, to the population in the lower state, i, is given by [72]

$$\frac{N_j}{N_i} = \frac{g_j}{g_i}\exp\left[-\frac{(E_j - E_i)}{kT}\right]. \tag{5.7}$$

In the absence of the external radiation field, as frequently occurs in the ISM, the intensity of the emission can be written as

$$I = N_j A_{21} = N_i \frac{g_j}{g_i}\exp\left[-\frac{(E_j - E_i)}{kT}\right], \tag{5.8}$$

where N_j is given by equation 5.7. Relating the number of atoms in a given state to the total number of atoms, N, and by letting the initial state be the ground state ($g_i = g_0$, $E_i = E_0 = 0$), the following relationship can be established, using equation 5.8:

$$\begin{aligned} N &= N_0 + N_1 + N_2 + ... \qquad (5.9)\\ &= N_0 + \frac{N_0 g_1}{g_0}\exp\left[-\frac{E_1}{kT}\right] + \frac{N_0 g_2}{g_0}\exp\left[-\frac{E_2}{kT}\right] + ... \\ &= \frac{N_0}{g_0}\left(g_0 + g_1\exp\left[-\frac{E_1}{kT}\right] + g_2\exp\left[-\frac{E_2}{kT}\right] + ...\right) \\ &= \frac{N_0}{g_0}\sum_{j=0}^{\infty} g_j\exp\left[-\frac{E_j}{kT}\right] \\ N &= \frac{N_0}{g_0}Q(T), \end{aligned}$$

where $Q(T)$ is called the partition function. From equation 5.7 (taking the initial state to be the ground state) and equation 5.9, N_j can be written

$$N_j = \frac{N}{Q(T)} g_j \exp\left[-\frac{E_j}{kT}\right]. \tag{5.10}$$

Equation 5.8 can then be expressed as

$$I = N_j A_{21} = \frac{N}{Q(T)} g_j \exp\left[-\frac{E_j}{kT}\right] A_{21},$$

The Einstein A coefficient can be expressed in a more fundamental way [73]

$$A_{21} = \frac{64\pi^4 \nu^3}{3hc^3} \frac{S\mu_{ji}^2}{g_j}. \tag{5.11}$$

Here, S is the line strength and μ_{ji} is the dipole moment. From this analysis, it is clear that under local thermal equilibrium, the measured intensity of emission is proportional to the total number of the atoms, N, and the temperature, T. The rotation diagram technique is the method for determining N and T, based upon this concept.

5.6.2 LTE rotation diagram technique

Rotation diagrams [74, 75, 76, 77] are a tool to study physical conditions in molecular clouds. The LTE Rotation Diagram technique is based on the following assumptions: the molecular transitions are optically thin (ie., no radiation emitted locally is absorbed locally), a single excitation LTE temperature defines all transitions, the rotation temperature is much larger that the temperature of the background, and that the Rayleigh-Jeans approximation holds for all transitions [73].

Using the analysis from the previous section, the rotation diagram can be calcu-

lated by the following equation:

$$\log L \equiv \underbrace{\log \frac{3k \int T_A^* dv}{8\eta_B \nu S \mu^2 g_I g_K}}_{y} = \underbrace{\log \frac{N}{Q_{rot}}}_{c} - \underbrace{\frac{E_u}{k}}_{x} \cdot \underbrace{\frac{\log e}{T_{rot}}}_{m.} \tag{5.12}$$

The quantities in this equation are in CGS units as follows:

$k = 1.380658 * 10^{-16}$ erg/K

$\int T_A^* dv$ is the integrated intensity in units of K*cm/s

η_B is the beam efficiency of the telescope

ν is the rest frequency of the spectrum in units of Hz

S is the line strength (Nm^4/esu^2)

μ is the relevant dipole moment in units of esu (1 Debye = 10^{-18}esu)

g_I is the reduced nuclear spin weight

g_K is the K-level degeneracy

N is the column density in units of cm^{-2}

Q_{rot} is the rotational partition function

E_u is the upper state energy of the transition in units of erg

T_{rot} is the rotation temperature in Kelvin

$L = \frac{3k \int T_A^* dv}{8\eta_B \nu S \mu^2 g_I g_K}$ and from this it is possible to derive the molecular abundance, N, and the rotational temperature, T_{rot}.

Most of the variables in this equation are known. Integrated areas of the lines can be calculated from the spectrum that is corrected for atmospheric transmission, coupling to the telescope and opacity of the lines. The quantity, $S\mu^2$, however, can be derived from the parameters in the molecular data base such as the Jet Propulsion Laboratory (JPL)

[78]. Their website [79] gives the following relationship between $S\mu^2$ and the integrated line intensity at 300 K, I_{ba}:

$$S\mu^2 = \frac{I_{ba}(T)Q_{rs}}{4.16231 \times 10^{-5}\nu_{ba}\left[e^{-\frac{E_L}{kT}} - e^{-\frac{E_U}{kT}}\right]}. \tag{5.13}$$

In this equation, Q_{rs} is the rotational partition function for 300 K. All variables in this equation for specific molecules can be found on the JPL website. The next step is to extract the column density and rotational temperature of the molecules from these equations. It can be seen that in equation 5.12, $\log(L)$ is linear in E_u/k. Therefore, a plot of the locus of the spectral line data on the graph of $\log L$ vs. E_u/k should fall on the straight line whose slope leads to the temperature of the emitting region given by 5.14 and whose intercept is the column abundance given by 5.15 , where c and m are taken from 5.12 :

$$T_{rot} = -\frac{\log e}{m} \tag{5.14}$$

$$N = 10^c \cdot Q_{rot}. \tag{5.15}$$

5.6.3 Orion-KL at 850 and 450 μm: LTE Rotation Diagrams

The rotation diagram technique has been applied to the 450 and 850 μm FTS spectra of Orion-KL. The principal emission arises from the molecules: carbon monoxide (CO), sulfur monoxide (SO), sulfur dioxide (SO_2) and methanol (CH_3OH). The technique can only be applied to the molecules SO and SO_2, which provide the sufficient number of lines for the analysis. The FTS data will be compared with the data from Serabyn [64] and Shilke et al. [71].

The U of L FTS and CSO spectra of Orion-KL at 450 μm and 850 μm were used for this analysis. The U of L and CSO FTS spectra were cross-calibrated using the integrated

CO line intensity. Following Serabyn, a correction for the effects of opacity was taken into account by multiplying the spectrum by $\tau/(1-e^{-\tau})$, where τ ranges from roughly 3 for lowest frequency transitions ($\sim$ 200 GHz), to 6 in midrange ($\sim$ 500 GHz), to 1.2 for the highest frequency lines ($\sim$ 900 GHz) [64].

To validate the rotational diagram technique, Serabyn's data was used to generate rotation diagrams and determine the temperature and column abundance of SO and SO_2 from his data. Line areas were determined directly from Serabyn's paper. The results are shown in figure 5.16. In these diagrams the opacity was assumed to be zero and the telescope coupling was 30 %.

A linear least squares fit to the data shown in figure 5.16 yields the following results: The rotation temperature for the SO molecule is calculated to be (100.56 ± 5.5) K and column density is $(4.54 \pm 0.6) \times 10^{16}\text{cm}^{-2}$. This is in very good agreement with the temperature quoted by Serabyn of 101 K: the author does not give the column density for this case. For the SO_2 molecule, the rotation temperature is calculated to be (80.4 ± 12) K and column density is $(7.03 \pm 1.7) \times 10^{16}\text{cm}^{-2}$. Serabyn's result was 93 K for rotation temperature and $8.0 \times 10^{16}\text{cm}^{-2}$, which falls inside our error bars. The purpose of this exercise was to validate the rotational diagram technique.

The U of L FTS data has subsequently been analyzed taking into account the opacity of the SO molecule with $\tau = 6$ for the 450 μm data and $\tau = 4.5$ for the 850 μm data. The results are shown in figure 5.17.

A linear least squares fit to the data shown in figure 5.17 yields the following results: The rotation temperature for the SO molecule is calculated to be (85 ± 23) K and

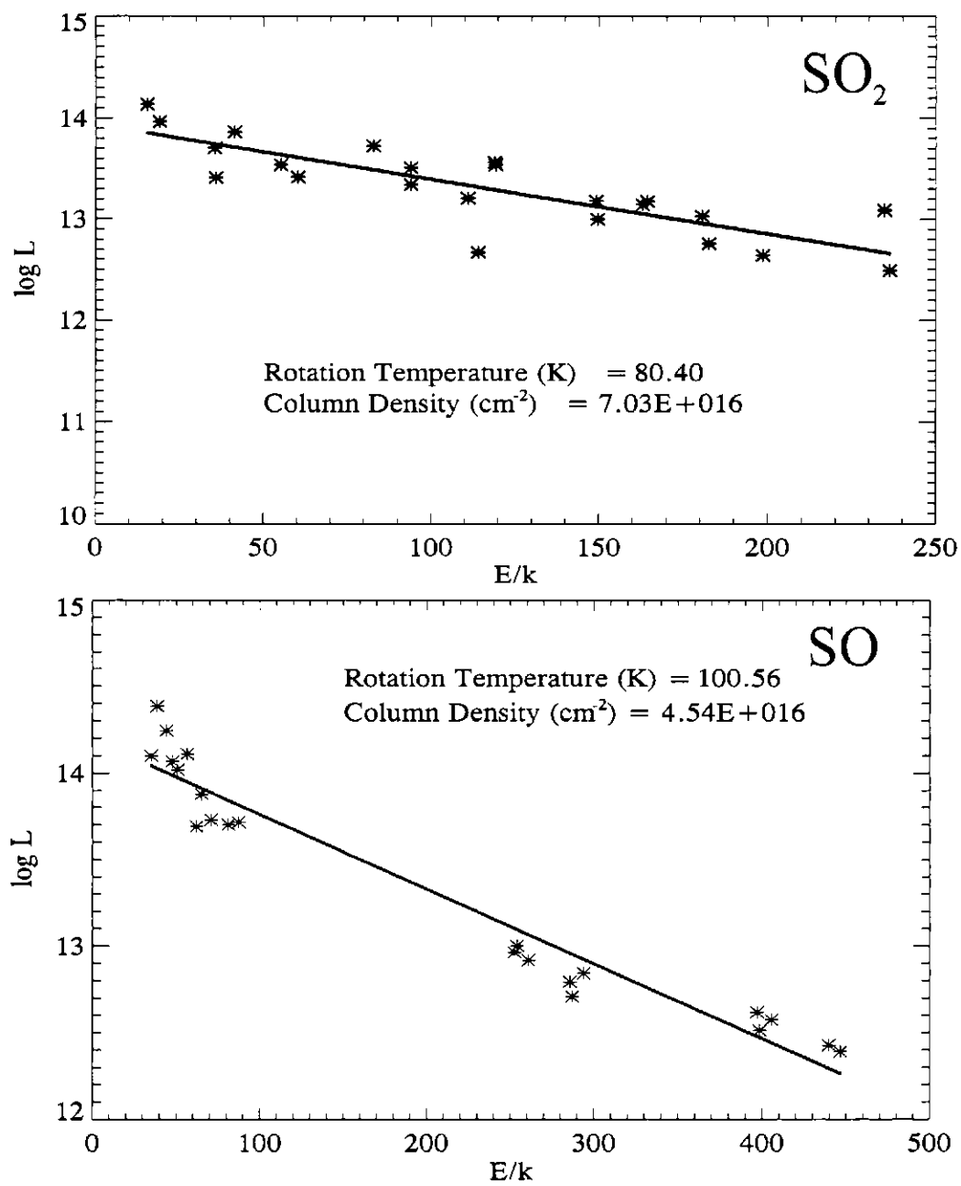

Figure 5.16: Rotation diagrams for SO_2 (upper plot) and SO (lower plot) reproduced from Serabyn's data.

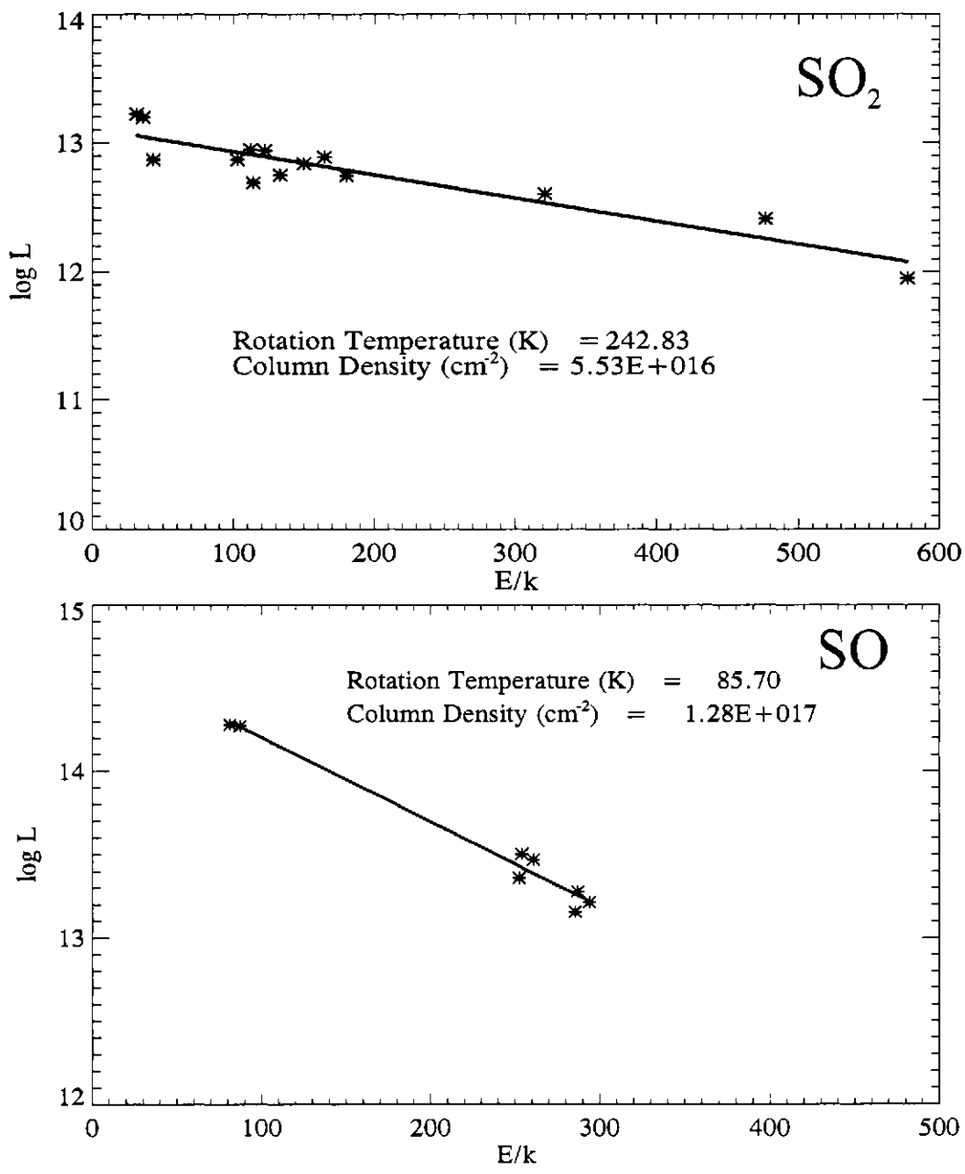

Figure 5.17: Rotation diagrams for SO_2 (upper plot) and SO (lower plot) for U of L FTS data.

	SO T_{rot} (K)	SO col. den. (cm^{-2})	SO_2 T_{rot} (K)	SO_2 col. den. (cm^{-2})
Serabyn	83 ± 2	2.2×10^{17}	93 ± 5	8×10^{16}
Schilke	64 ± 5	$(2.3 \pm 0.7) \times 10^{17}$	187 ± 4	$(6 \pm 0.3) \times 10^{16}$
UofL FTS	85 ± 23	$(1.3 \pm 3.76) \times 10^{17}$	242 ± 29	$(5.5 \pm 0.7) \times 10^{16}$

Table 5.2: Comparison of Rotation Temperatures and Column Densities for two different molecules: SO and SO_2

column density is $(1.3 \pm 3.76) \times 10^{17}cm^{-2}$. The rotation temperature for SO_2 molecule is calculated to be (242.83 ± 29) K and column density is $(5.53 \pm 0.7) \times 10^{16}cm^{-2}$. The column density is in good agreement with the Schilke et al. value of $6 \times 10^{16}cm^{-2}$, but the temperature differs by about 55 K. All temperatures and column densities values are shown in table 5.2. Our results for SO are in closer agreement with Serabyn's analysis, while the SO_2 results are in closer agreement with Schilke's analysis. In the comparison of the two different FTS measurements, the difference is most likely due to the much wider (200 - 900 GHz) spectral range that Serabyn was able to observe. As discussed above, extremely poor weather on several observing runs prevented us from obtaining 850 μm measurements. Overall, our results are closer to the measurements of Schilke, but the error bars are quite large. This illustrates the difficulty in determining the physical condition in the interstellar medium.

5.7 Conclusion

This chapter has shown that, with an FTS, it is possible to extract the continuum and line components from the interstellar medium. Three methods of determining the model SED have been discussed and it was shown that single band FTS spectroscopy method is, in principle, superior to dual band photometry or dual band FTS spectroscopy

(when 450 μm atmosphere is unstable at 450 μm). This chapter also presented the results of SEDs in the Orion-KL region using two methods: Fitting the continuum to the regions of lowest spectral line emission in the Orion-KL, and fitting the heterodyne spectrum plus the continuum term to the FTS spectrum. Although the error bars are large, the derived SEDs are in agreement with the general SED found for the OMC. Finally, for completeness, the rotation diagram technique was introduced and the results for the rotation temperature and the molecular abundance of SO and SO_2 from Orion-KL were found to be in close agreement with previous results. While the resolution of an FTS is at least two orders of magnitude lower than of heterodyne receiver, it is encouraging that the FTS spectra yield results for molecular abundances and temperature that are not significantly different from those determined with a much higher resolution heterodyne technique. The results presented in this thesis illustrate the potential power of Fourier Transform Spectroscopy as a diagnostic tool in understanding physical conditions in the interstellar medium.

Chapter 6

Conclusion and future work

This thesis has addressed the applicability of Fourier transform spectroscopy at submillimetre wavelengths to the study of the ISM. FTS measurements of the two brightest regions of the Orion Molecular Cloud, Orion-KL and Orion-S, shown in figure 1.2, obtained with an FTS, have been presented. This is only the second FTS in operation, which has been designed specifically for observations at submillimetre wavelengths. As discussed in the thesis, the classical instrumental line shape of the U of L FTS (ie., the sinc function) is clearly evident in the spectra. The continuum component has been extracted, which carries information on the properties of the dust in the ISM. From this analysis it is possible to determine the dust temperature and the emissivity. The spectra have been shown to be superior to the earlier results of Serabyn [64], which had ill-defined line shape and continuum.

The U of L FTS spectra have also been compared with heterodyne spectra obtained contemporaneously. When the heterodyne spectra are convolved with a sinc function of

the appropriate resolution, there is an excellent agreement between heterodyne and FTS spectra. However, the heterodyne spectra often have ill-defined baselines and therefore cannot be used to study continuum component of emission.

In this thesis, a model SED of a molecular cloud was used to investigate various methods of extracting the dust emissivity from submillimetre wavelength observations. From this work it was concluded that single band FTS spectroscopy has the best sensitivity to errors in β, compared to the dual-band SCUBA photometric measurements and the dual-band FTS spectroscopic measurements, because the atmospheric variations in the 450 μm band are noticeable.

Along the way, two specific aspects of FTS spectroscopy were studied in detail; cosmic ray removal and apodization. Ten apodization functions have been derived (seven of them new) that provide a small set from which to choose the optimum tradeoff between spectral resolution and ringing in the ILS. These 10 functions cover the range from 1.1 to 2.0 of FWHM in steps of 0.1 and it is expected that this set of functions will find use in a wide range of fields involving Fourier analysis.

6.1 Future work

The Submillimeter Common User Bolometer Array (SCUBA-2) [35, 80] is currently being developed for use at the JCMT in Hawaii, and it will become operational in 2006. SCUBA-2 will replace the existing bolometer array detector, SCUBA, which is limited by the small array size. The new SCUBA-2 camera will feature $\sim 10,000$ pixels in two arrays and a field of view 8' [35]. Combined with the increased sensitivity of the

superconducting bolometers, SCUBA-2 will result in a factor of 1000 increase in mapping speeds of a compared to its highly successful predecessor [35].

Two auxiliary instruments will be developed for this detector: an imaging FTS (FTS-2) and a polarimeter. These instruments will open up another dimension in sub-millimetre astronomy by enabling spectroscopic and polametric studies of a wide range of astronomical objects, such as infrared galaxies, interstellar mediums, star forming regions, and planetary atmospheres.

Under the current design, FTS-2 will use ~2000 pixels, each pixel having over 10 times the sensitivity of the detector that produced the data for this thesis. Since the mapping time required is given by the following equation [80]:

$$t = \frac{3.8 \times 10^{31}}{\eta} \left(\frac{A}{FOV} \right) \left(\frac{NEP}{\Delta f \times \Delta T} \right)^2, \tag{6.1}$$

where η is the observing efficiency, A is the area of the map, FOV is the FTS field of view, NEP is the detector noise-equivalent-power measure at the bolometer, Δf is the spectral resolution in MHz and ΔT is the temperature sensitivity. From this equation, it can be seen that if each pixel has 10 times more sensitivity, then with 2000 pixels it will be possible to map the sky 200,000 times faster than with the spectrometer described in this thesis.

FTS-2 will be able to obtain simultaneous, variable, resolution 450 μm and 850 μm wavelength spectra from each point on the sky corresponding to individual pixels in the array. FTS-2 will use the Mach-Zehnder spectrometer design, which has also been adopted for the Spectral and Photometric Imaging Receiver (SPIRE) instrument for the European Space Agency (ESA) Herschel space mission. FTS-2 will exploit two input ports; one port will view the source while the other port will view the adjacent region of the sky. The

second port will allow for the automatic subtraction of the atmospheric emission from the source, on a pixel-by-pixel basis. This will provide exceptional atmospheric correction which will enable FTS-2 to determine the properties of sources that are only few tens of mJy's in brightness. FTS-2 will allow astronomers to determine the properties of dust in the ISM to a much greater accuracy than is currently possible. In particular, its unique ability to separate the continuum and line components emission will remove one of the principal uncertainties in this field of research.

The work on the apodizing and the SED techniques in this thesis will find direct application with this new, cutting edge detector system.

Appendix A

Unit Conversion

Unit conversion from wavelength to frequency (Hz or wavenumber) can be confusing; this appendix describes the various conversion factors. Wavelength is defined as $c = \nu\lambda$, where ν is the frequency in Hertz (Hz), λ is the wavelength (m), and c is the speed of light. It is customary to express the wavelength in the units of nanometers (nm) or micrometers (μm) since. In Fourier transform spectroscopy, the natural unit of spectral scale is inverse pathlength, or wavenumber, $\sigma = \frac{1}{\lambda}$ (cm^{-1}). The wavenumber scale can simply be converted to frequency by multiplying by speed of light, (ie., is to say that $\nu = c\sigma$. The values of wavelength, wavenumber, and frequency corresponding to the 450 and 850 μm spectra reported in this thesis, are given below.

	Band centre	Left edge	Right edge
λ (μm)	450	476	429
σ (cm^{-1})	22.2	21	23.3
ν (GHz)	666	630	700

Table A.1: Unit conversion between wavelength, λ, wavenumber, σ and frequency, ν for 450 μm waveband.

	Band Centre	Left edge	Right edge
λ (μm)	850	909	833
σ (cm^{-1})	11.6	11	12
ν (GHz)	353	330	360

Table A.2: Unit conversion between wavelength, λ, wavenumber, σ and frequency, ν for 850 μm waveband.

Appendix B

A list of acronyms

AIG - Astronomical Instrumentation Group

CSO - Caltech Submillimeter Observatory

CWT - Continuous Wavelet Transform

ESA - European Space Agency

FTS - Fourier Transform Spectroscopy

FWHM - Full Width Half Max

IDL - Interactive Data Language

ILS - Instrumental Line Shape

ISF - Integral Shaped Filament

ISM - Interstellar Medium

JCMT - James Clerk Maxwell Telescope

JPL - Jet Propulsion Laboratory

KPNO - Kitt Peak National Observatory

LTE - Local Thermal Equilibrium

MRA - Multi-resolution Analysis

NOAO - National Optical Astronomy Observatory

OMC - Orion Molecular Cloud

PCF - Phase Correction Function

RA - Right Ascension

SCUBA - Submillimeter Common User Bolometer Array

SED - Spectral Energy Distribution

SPIRE - Spectral and Photometric Imaging Receiver

U of L - University of Lethbridge

ZPD - Zero Path Difference

Bibliography

[1] P. Jacquinot, "New Developments in Interference Spectroscopy," Rep. Prog. Phys. **23,** 267–312 (1960).

[2] P. Fellgett, "A Propos de la Theorie Du Spectrometre Interferentiel Multiplex," J. Phys. Radium **19,** 187 (1958).

[3] D. Johnstone and J. Bally, "JCMT/SCUBA Submillimeter Wavelength Imaging of the Integral-Shaped Filament in Orion," The Astronomical Journal **510,** L49–L53 (1999).

[4] S. P. Davis, M. C. Abrams, and J. W. Brault, *Fourier Transform Spectrometry* (Academic Press, London, 2001).

[5] D. A. Naylor, B. G. Gom, I. S. Schofield, G. J. Tompkins, and G. R. Davis, "Mach-Zehnder Fourier Transform Spectrometer for Astronomical Spectroscopy at Submillimeter Wavelengths," Proc. SPIE, Millimeter and Submillimeter Detectors for Astronomy **4855,** 540–551 (2003).

[6] P. Schilke, T. D. Groesbeck, G. A. Blake, and T. G. Phillips, "A Line Survey of Orion KL from 325 to 360 GHz," The Astronomical Journal Supplement Series **108,** 301–337 (1997).

[7] J. E. Dyson and D. A. Williams, *The Physics of the Interstellar Medium* (IOP Publishing Ltd, 1997).

[8] M. Harwit, *Atrophysical Concepts* (Springer-Verlag New York Inc., 1988).

[9] V. Bromm and R. B. Larson, "The First Stars," Annual Review of Astronomy and Astrophysics **42,** 79–118 (2004).

[10] W. J. Kaufmann and R. A. Freedman, *Universe*, 5 ed. (W. H. Freedman and Co., 1999).

[11] J. L. Spitzer, "On a Possible Interstellar Galactic Corona," Astrophysical Journal **124,** 20–34 (1956).

[12] G. B. Field, D. W. Goldsmith, and H. J. Habing, "Cosmic-Ray Heating of the Interstellar Gas," Astrophysical Journal (Letters) **155,** L149 (1969).

[13] C. F. McKee and J. P. Ostriker, "A Theory of the Interstellar Medium: Three Components Regulated by Supernova Explosions in an Inhomogeneous Substrate," The Astrophysical Journal **218,** 148–169 (1977).

[14] R. H. Hildebrand, "The Determination of Cloud Masses and Dust Characteristics from Submillimetre Thermal Emission," Q. Jl R. astr. Soc. **24,** 267–282 (1983).

[15] R. Bowers and T. Deeming, *Astrophysics II: Interstellar Matter and Galaxies* (Jones and Bartlett Publishers, INC. Boston, 1984).

[16] R. Stognienko, T. Henning, and V. Ossenkopf, "Optical Properties of Coagulated Particles," Astronomy and Astrophysics **296,** 797–809 (1995).

[17] V. Ossenkopf and T. Henning, "Dust Opacities for Protostellar Cores," Astronomy and Astrophysics **291,** 943–959 (1994).

[18] R. Genzel and J. Stutzki, "The Orion Molecular Cloud and Star-Forming Region," Annual Review of Astronomy and Astrophysics **27,** 41–85 (1989).

[19] N. R. A. Observatory, http://www.cv.nrao.edu/ awootten/allmols.html .

[20] A. L. Lavoisier, J. B. J. Fourier, and M. Faraday, *Elements of Heat, Analytical Theory of Heat and Experimental Researches in Electricity* (Encyclopedia Britannica, Inc., 1952).

[21] I. Grattan-Guinness, *Joseph Fourier 1768-1830* (The Massachusetts Institue of Technology, 1972).

[22] E. Hecht, *Optics* (Addison Wesley Longman Inc., New York, 2002).

[23] E. O. Brigham, *The Fast Fourier Transform* (Prentice-Hall Inc., 1974).

[24] J. S. Walker, *Fourier Analysis* (Oxford University Press, 1988).

[25] P. R. Griffiths and J. A. de Haseth, *Fourier Transform Infrared Spectrometry* (John Wiley and Sons Inc., New York, 1986).

[26] M. Born and E. Wolf, *Principles of Optics: Electromagnetic Theory of Propagation, Interference and DIffraction of Light*, 6 ed. (Cambridge University Press, 190).

[27] R. J. Bell, *Introductory Fourier Transform Spectroscopy* (Academic Press, New York and London, 1972).

[28] L. R. J. W. Strutt, Phil. Mag. **24,** 864 (1912).

[29] J. Kauppinen, T. Karkkainen, and E. Kyro, "Correcting Errors in the Optical Path Difference in Fourier Spectroscopy: A New Accurate Method," Applied Optics **17,** 1587–1594 (1978).

[30] B. Carli, F. Forni, and F. Mencaraglia, "Phase Error Correction in FT Spectroscopy of Spectra with Positive and Negative Intensities," International Journal of Infrared and Millimeter Wave **3,** 529–540 (1982).

[31] R. C. M. Learner, A. P. Thorne, I. Wynne-Jones, J. W. Brault, and M. C. Abrams, "Phase Correction of Emission Line Fourier Transform Spectra," J. Opt. Soc. Am. A. **12,** 2165–2171 (1995).

[32] M. S. Hutson and M. S. Braiman, "Application of Doubled-Angle Phase Correction Method to Time-Resolved Step-Scan FT-IR Spectra," Vibrational Spectroscopy **19,** 379–383 (1998).

[33] M. L. Forman, W. H. Steel, and G. A. Vanasse, "Correction of Asymmetric Interferograms Obtained in Fourier Spectroscopy," J. Opt. Soc. Am **56,** 59 (1966).

[34] D. A. Naylor, G. R. Davis, T. A. Clark, P. A. R. Ade, and M. J. Griffin, "Fourier Transform Spectroscopy at the James Clerk Maxwell Telescope," Optical Society of America FTS and ORS topical meeting poster FMD9, Coeur d'Alene, Idaho (2001).

[35] D. A. Naylor and B. G. Gom, "SCUBA-2 Imaging Fourier Transform Spectrometer," Proc. SPIE, Imaging Spectrometry IX **5159,** 91–101 (2004).

[36] B. Swinyard *et al.*, "The Imaging FTS for Herschel SPIRE," IR Space Telescopes and Instruments, Proc. SPIE **4850,** 698–709 (2003).

[37] J. F. James and R. S. Sternberg, *The Design of Optical Spectrometers* (Butler and Tanner Ltd., London, 1969).

[38] J. Kauppinen and J. Partanen, *Fourier Transforms in Spectroscopy* (Wiley-VCH Verlag Berlin GmbH, Berlin, 2001).

[39] B. B. Rossi, *Cosmic Rays* (McGraw-Hill Inc., New York, 1964).

[40] M. Lanfranchi, B. Carli, A. Gignoli, C. Lee, and M. Ridilfi, "Cosmic-Ray Flux Detected by an IR Bolometer Operated on Board of a Stratospheric Aircraft," Infrared Physics and Technology **40,** 379–386 (1999).

[41] V. L. Ginzburg, *The Astrophysics of Cosmic Rays* (Israel program for scientific translations Ltd., 1969).

[42] D. Jarman, intersil Application note AN 9504 (unpublished).

[43] B. G. Gom, "A Cryogenic Detector for Submillimetre Astronomy," Master's thesis, University of Lethbridge (1999).

[44] "The Wavelet Tutorial," http://users.rowan.edu/ polikar/WAVELETS/WTtutorial.html .

[45] S. Mallet, "A Theory for Multiresolution Signal Decomposition: The Wavelet Representation," IEEE Trans. on Pattern Analysis and Machine Intelligence **14,** 710–732 (1992).

[46] I. Daubechies, "The Wavelet Transform, Time-Frequency Localization and Signal Analysis," IEEE Transactions on Information Theory **36,** 961–1004 (1990).

[47] *IDL Wavelet Toolkit User's Guide*, Research Systems, Inc., 2002.

[48] C. Zhu and P. R. Griffiths, "Extending the Range of Beer's Law in FT-IR Spectrometry. Part 2: Theoretical Study of Continuous Apodization Functions," Applied Spectroscopy **52,** 1409–1413 (1998).

[49] F. J. Harris, "On the Use of Windows for Harmonic Analysis with the Discrete Fourier Transform," Proceedings of the IEEE **66,** 51–83 (1978).

[50] R. H. Norton and R. Beer, "Errata," J. Opt. Soc. Am. **67,** 419 (1977).

[51] R. H. Norton and R. Beer, "New Apodizing Functions for Fourier Spectrometry," J. Opt. Soc. Am. **66,** 259–264 (1976).

[52] A. S. Filler, "Apodization and Interpolation in Fourier-Transform Spectroscopy," J. Opt. Soc. Am. **54,** 762–767 (1964).

[53] "The Interactive Data Language,", Research Systems Inc., 4990 Pearl East Circle, Boulder, CO 80301, USA.

[54] J. A. Nelder and R. Mead, "A Simplex Method for Function Minimization," Computer Journal **7,** 308–313 (1965).

[55] W. H. Press, S. A. Teukolsky, W. T. Vetterling, and B. P. Flannery, *Numerical Recipes in C: The Art of Scientific Computing* (Cambridge University Press, 1992).

[56] M. J. D. Powell, "A Method for Minimizing a Sum of Squares of Non-Linear Functions Without Calculating Derivatives," The Computer Journal **7,** 303–307 (1965).

[57] B. G. Gom and D. A. Naylor, "An Update on the Imaging Fourier Transform Spectrometer for SCUBA-2," Proc. SPIE, Astronomical Telescopes and Instrumentation 5498 , in press.

[58] D. Ward-Thompson, P. F. Scott, R. E. Hills, and P. Andre, "A Submillimetre Continuum Survey of Pre-Protostellar Cores," Mon. Not. R. Astron. Soc. **268,** 276–290 (1994).

[59] C. D. Wilson, L. W. Avery, M. Fich, D. Johnstone, G. Joncas, L. B. G. Knee, H. E. Matthews, G. F. Mitchell, G. H. Moriarty-Schieven, and R. E. Pudritz, "Submillimeter Continuum Emission in the Rho Ophiuchi Molecular Cloud: Filaments, Arcs and an Unidentified Far-Infrared Object," The Astrophysical Journal **513,** L139–L142 (1999).

[60] W. S. H. et Al., "SCUBA: A Common-User Submillimetre Camera Operating on the James Clerk Maxwell Telescope," Mon. Not. R. Astron. Soc. **303,** 659–672 (1999).

[61] I. M. Chapman, D. A. Naylor, and R. R. Phillips, "Correlation of Atmospheric Opacity Measurements by SCUBA and an Infrared Radiometer," Mon. Not. R. Astron. Soc **354,** 621–628 (2004).

[62] T. A. Clark, D. A. Naylor, and G. R. Davis, "Detection and Limb Brightening of the HI N=20 - 19 Rydberg Line in the Submillimetre Spectrum of the Sun," Astronomy and Astrophysics **357,** 757–762 (2000).

[63] E. W. Weisstein, "Levenberg-Marquardt Method," From MathWorld–A Wolfram Web Resource. http://mathworld.wolfram.com/Levenberg-MarquardtMethod.html .

[64] E. Serabyn and E. W. Weisstein, "Fourier Transform Spectroscopy of Orion Molecular Cloud Core," The Astrophysical Journal **451,** 238–251 (1995).

[65] I. M. Chapman, "The Atmosphere Above Mauna Kea at Mid-Infrared Wavelengths," Master's thesis, University of Lethbridge (2002) .

[66] G. R. Davis, D. A. Naylor, M. J. Griffin, T. A. Clark, and W. S. Holland, "Broadband Submillimetre Spectroscopy of HCN, NH3 and PH3 in the Troposphere of Jupiter," Icarus **130,** 387–403 (1997).

[67] A. Russel, H. V. D. Stadt, B. Hayward, and B. Duncan, "JCMT Plans for a Heterodyne Array," Multi-feed Systems for Radio Telescopes, ASP Conference Series **75,** 179–185 (1995).

[68] R.M.Prestage, H.Meyerdierks, J.F.Lightfoot, T.Jenness, R.P.J.Tilanus, R.Padman, and A.J.Chipperfield, "SPECX - A Millimetre Wave Spectral Reduction Package,", 2000, cCLRC / Rutherford Appleton Laboratory Particle Physics Astronomy Research Council.

[69] H. Matthews and T. Jenness, "SPECX Cookbook Reduction of Millimetre Wave Data,", 1997, cCLRC / Rutherford Appleton Laboratory Particle Physics Astronomy Research Council.

[70] P. Lena, *Observational Astrophysics* (Springer-Verlag Berlin Heidelberg New York, 1986).

[71] P. Schilke, D. J. Benford, T. R. Hunter, D. C. Lis, and T. G. Phillips, "A Line Survey of Orion-KL from 607 to 725 GHz," The Astrophysical Journal Supplement Series **132,** 281–364 (2001).

[72] G. K. Woodgate, *Elementary Atomic Structure* (McGraw-Hill Publishing Company Ltd., 1970).

[73] B. E. Turner, "A Molecular Line Survey of Sagittarius B2 and Orion-KL from 70-115 GHz II. Analysis of the Data," The Astrophysics Journal Supplement Series **76,** 617–686 (1991).

[74] M. A. Thompson, G. H. Macdonald, and T. J. Millar, "A 330-360 GHz Spectral Survey of G34.3+0.15 III. The Outer Halo," Astron. Astrophys. **342,** 809–822 (1999).

[75] G. A. Blake, E. C. Sutton, C. R. Masson, and T. G. Phillips, "Molecular Abundances in OMC-1: The Chemical Composition of Interstellar Molecular Clouds and the Influence of Massive Star Formation," The Astrophysical Journal **315,** 621–645 (1987).

[76] G. H. Macdonald, A. G. Gibb, R. J. Habing, and T. J. Millar, "A 330 - 360 GHz Spectral Survey of G 34.3+0.15 I. Data and Physical Analysis," Astron. Astrophys. Suppl. Ser. **119,** 333–367 (1996).

[77] G. A. Blake, E. C. Sutton, C. R. Masson, and T. G. Phillips, "The Rotational Emisision - Line Spectrum of Orion A Between 247 and 263 GHz," Astron. Astrophys. Suppl. Ser. **60,** 357–374 (1986).

[78] "Jet Propulsion Laboratory," http://www.jpl.nasa.gov/ .

[79] H. M. Pickett, E. A. Cohen, H. J. Drouin, and J. C. Pearson, "Submillimeter, Millimeter and Microwave Spectral Line Catalog," http://spec.jpl.nasa.gov/ftp/pub/catalog/doc/catintro.pdf (2003).

[80] B. G. Gom and D. A. Naylor, "An Update on the Imaging Fourier Transform Spectrometer for SCUBA-2," Proc. SPIE, Astronomical Telescopes and Instrumentation, in press 5496 .